

THESIS FOR THE DEGREE OF DOCTOR OF PHILOSOPHY

**Non-invasive EEG Functional Neuroimaging
for Localizing Epileptic Brain Activity**

by

YAZDAN SHIRVANY



CHALMERS

Department of Signals and Systems
CHALMERS UNIVERSITY OF TECHNOLOGY
Göteborg, Sweden 2013

Göteborg 2013

Non-invasive EEG Functional Neuroimaging for Localizing Epileptic Brain Activity

YAZDAN SHIRVANY

ISBN 978-91-7385-810-6

This thesis has been prepared using L^AT_EX.

Copyright © YAZDAN SHIRVANY, 2013.

All rights reserved.

Doktorsavhandlingar vid Chalmers Tekniska Högskola

Ny serie nr 3491

ISSN 0346-718X

Department of Signals and Systems
Signal Processing and Biomedical Engineering
Chalmers University of Technology
SE-412 96 Göteborg, Sweden

Phone: +46 (0)31 772 1716

Fax: +46 (0)31 772 1725

E-mail: yazdan.shirvany@chalmers.se

Front cover: Credit @psdesign1 - Fotolia.com.

Printed by Chalmers Reproservice
Göteborg, Sweden, February 2013

*If we knew what it was we were doing,
it would not be called research, would it?*
A. Einstein (1879-1955)

Abstract

Epilepsy is one of the most common neurologic diseases in the world, and is present in up to 1% of the world's population. Many patients with epilepsy never receive the treatment which make them seizure free. Surgical therapy has become an important therapeutic alternative for patients with drug resistant epilepsy. Correct and anatomically precise localization of the epileptic focus, preferably with non-invasive methods, is the main goal of the pre-surgical epilepsy diagnosis to decide if resection of brain tissue could be a successful treatment option. The most important diagnosis tool used at epilepsy surgery centers is electroencephalography (EEG), which is used to find the source of activities inside the brain by measuring the potential on the scalp with EEG electrodes at different locations. One major advantage of EEG source localization over other brain imaging modalities is its high temporal resolution. The procedure of EEG source localization deals with solving the forward problem to find the scalp potentials for a given current dipole(s) inside the brain and the inverse problem to estimate the source(s) that fits with the given potential distribution at the scalp electrodes. Realistic models of the human head are geometrically complex and the tissue conductivity is inhomogeneous as well as anisotropic. A critical issue for the forward problem is how to handle the computational complexity in the numerical approaches with regard to the inverse problem. There is still a lack of sufficiently powerful methods and algorithms that would satisfy the time-restrictions for the solution of the inverse problem. The overall goal in this thesis is to develop a non-invasive, clinically-viable, time-efficient method for localization of epileptic brain activity based on EEG source localization. For the forward problem two methods are proposed for modeling the dipole source which can handle the head model complexity; a modified subtraction method and a method based on the reciprocity theorem. For the inverse problem we propose a new global optimization method based on particle swarm optimization (PSO) to solve the multi-dipole EEG source localization. The techniques of multimodal magnetic resonance imaging (MRI) are used in order to generate a high-resolution realistically shaped volume conductor model. The anisotropic white matter conductivity tensor is determined by diffusion tensor MRI (DT-MRI) measurements and isotropic conductivities are assigned to the other tissues in the model. The new proposed methods are tested for synthetic and real EEG data. The results are compared with state-of-the-art and other existing methods. In the synthetic data both spherical head models and realistic

head models with anisotropic tissues are used for validation. In the real EEG test, measured somatosensory evoked potentials (SEPs) for a healthy subject are used for EEG source localization. A realistic 1 *mm* patient-specific, anisotropic finite element model of the subject's head, with special consideration of precise modeling the two compartments, skull and cerebrospinal fluid (CSF), generated from T1-weighted MRI data is used. Source localization results are validated against a clinical expert source localization as well as functional MRI palm-brushing measurements and the proposed method typically finds the source location within 10 millisecond. The EEG source localization results agree well with both the clinical expert and fMRI results. The finite element method (FEM) in combination with the reciprocity theorem and the modified PSO is a highly efficient and robust solution methodology for EEG source localization.

Preface

This thesis is in partial fulfillment of the requirements for the degree of Doctor of Philosophy at Chalmers University of Technology, Göteborg, Sweden.

The work has been performed in the Biomedical Electromagnetics Group, Department of Signals and Systems at Chalmers between Jan. 2009 and Jan. 2013 under the supervision of Professor Mikael Persson, Associate Professor Fredrik Edelvik (Fraunhofer-Chalmers Research Center, FCC) and Medical Doctor Anders Hedström (Sahlgrenska University Hospital). Prof. Persson also acts as examiner of the thesis. In addition to the supervisors, Dr. Stefan Jakobsson has been involved in this work.

This work has been supported in part by Chalmers University of Technology and Islamic Development Bank. The project has been performed in collaboration with industry, namely FCC. The data for this thesis was recorded by the Neurophysiology Department, Sahlgrenska University Hospital, Göteborg, Sweden.

Acknowledgments

I would like to express my sincere gratitude to my supervisors for their time and patience. First of all, I express my sincere thanks to Prof. Mikael Persson for his support and patience. I would also like to express my thankfulness to my co-supervisor Assoc. Prof. Fredrik Edelvik from FCC for all his kindness and time he dedicated to the progress of my research articles. I am very grateful to Dr. Anders Hedström, Prof. Mikael Elam and Assoc. Prof. Magnus Thordstein from Sahlgrenska University Hospital for their valuable feedback and enthusiasm with pushing this work towards clinics. I also want to thank all the other nice members involved in this project, Dr. Stefan Jakobsson, Dr. Artur Chodorowski, Dr. Andrew Mehnert, Dr. Tonny Rubaek, Lic.Eng. Oskar Talcoth, M.S. Simon Aleryd, M.S. Qaiser Mahmood and M.S. Irene Perini.

I would like to thank my friends for all their support and kindness. Here I say thanks to my lovely brother Reza who always be with me. Lot of thanks to Mahdiah for all her support. My special thanks to Sajed, Amir, Mohammad, Nima, Ramin, Babak and all other my lovely friends that create an unforgettable time in my life. Last but not least, I would like to mention the unfailing support of my parents, bigger brother, Ramin, and lovely sister, Roshan. Thanks to all of you.

List of Publications

This thesis is based on the following papers:

Paper I

Yazdan Shirvany, Fredrik Edelvik, Stefan Jakobsson, Anders Hedström, Mikael Persson, “Application of Particle Swarm Optimization in Epileptic Spike EEG Source Localization”, *Applied Soft Computing*, in press, Available online, 2012.

Paper II

Yazdan Shirvany, Fredrik Edelvik, Stefan Jakobsson, Anders Hedström, Qaiser Mahmood, Artur Chodorowski, Mikael Persson. “Non-invasive EEG Source Localization using Particle Swarm Optimization: A Clinical Experiment”, Annual International Conference of the IEEE, *Engineering in Medicine and Biology Conference (EMBC)*, pp: 6232–6235, 2012.

Paper III

Yazdan Shirvany, Antonio R. Porras, Koushyar Kowkabzadeh, Qaiser Mahmood, Hoi-Shun Lui, Mikael Persson. “Investigation of Brain Tissue Segmentation Error and its Effect on EEG Source Localization”, Annual International Conference of the IEEE, *Engineering in Medicine and Biology Conference (EMBC)*, pp: 1522–1525, 2012.

Paper IV

Yazdan Shirvany, Xinyuan Chen, Prathamesh Sharad Dhanpalwar, Mahdieh Mir Hashemi, Fredrik Edelvik and Mikael Persson. “Influence of Different Sources of Noise on Epileptic Spike EEG Source Localization”, *SPIE Medical Imaging, Biomedical Applications in Molecular, Structural, and Functional Imaging*, Volume 8672, 2013.

Paper V

Yazdan Shirvany, Fredrik Edelvik, Stefan Jakobsson, Anders Hedström, Qaiser Mahmood, Artur Chodorowski, Mikael Persson. “Particle Swarm Optimization Applied to EEG Source Localization of Somatosensory Evoked Potentials”, Submitted to *IEEE Transaction on Neural System and Rehabilitation Engineering*, 2013.

Paper VI

Yazdan Shirvany, Tonny Rubaek, Fredrik Edelvik, Stefan Jakobsson, Oskar Talcoth and Mikael Persson. “Evaluation of a Finite-Element Reciprocity Method for Epileptic EEG Source Localization: Accuracy, Computational Complexity and Noise Robustness”, Submitted to *Letters of Biomedical Engineering*, 2012.

Paper VII

Fredrik Edelvik, Björn Andersson, Stefan Jakobsson, Stig Larsson, Mikael Persson and **Yazdan Shirvany**. “An Improved Method for Dipole Modeling in EEG-Based Source Localization”, World Congress on Medical Physics and Biomedical Engineering, *IFMBE Proceedings*, Vol. 25, pp:146–149, 2009.

Paper VIII

Qaiser Mahmood, **Yazdan Shirvany**, Andrew Mehnert, Artur Chodorowski, Johanna Gellermann, Fredrik Edelvik, Anders Hedström and Mikael Persson. “On the Fully Automatic Construction of a Realistic Head Model for EEG Source Localization”, Submitted to Annual International Conference of the IEEE, *Engineering in Medicine and Biology Conference (EMBC)*, 2013.

Paper IX

Yazdan Shirvany, Fredrik Edelvik, Magnus Thordstein, Irene Perini, Anders Hedström, Mikael Elam, Mikael Persson. “Real-Time EEG Source Localization using Reciprocity Theorem and Particle Swarm Optimization”, Submitted to *IEEE Transaction on Biomedical Engineering*, 2013.

Other related publication by the author not included in this thesis:

1. Mikael Persson, Tomas McKelvey, Andreas Fhager, Hoi Shun Lui, **Yazdan Shirvany**, Artur Chodorowski, Qaiser Mahmood, Fredrik Edelvik, Magnus Thordstein, Anders Hedström and Mikael Elam, “Advances in Neuro Diagnostic based on Microwave Technology, Transcranial Magnetic Stimulation and EEG source localization”, *Asia Pacific Microwave Conference*, pp:469–472, 2011.
2. **Yazdan Shirvany**, Mikael Persson, Fredrik Edelvik, Stefan Jakobsson, Anders Hedström, Koushyar Kowkabzadeh, Antonio Reyes and Hoi Shun Lui. “Dipole Source localization based on Epileptic Spike Signals and Particle Swarm Optimization method in the Finite Element Head Model”, *Proceedings of Medicinteknikdagarna 2010*, pp. 128.

3. Antonio Reyes, Koushyar Kowkabzadeh, **Yazdan Shirvany**, Hoi Shun Lui, Simon Bergstrand, Anders Hedström and Mikael Persson, “Evaluations of Brain Tissue Segmentation from the Widely-Used Software Packages”, *Proceedings of Medicinteknikdagarna 2010*, pp. 187.

Contents

Abstract	i
Preface	iii
Acknowledgments	v
List of Publications	vii
Contents	x
Notations	xiii
Abbreviations and Acronyms	xv
Part I: Introductory Chapters	1
1 Introduction	3
1.1 EEG Source Localization	5
1.2 Overview of the Thesis	9
2 The Physics of EEG	11
2.1 Neurophysiology	11
2.2 The Generators of the EEG	13
3 Forward Problem	15
3.1 Poisson's Equation	15
3.2 The Source Currents	16
3.3 EEG Forward Problem	17
3.4 Solving the Forward Problem: Green's Function	18
3.5 Finite Element Method	19
3.6 Source Modeling	22
3.6.1 Direct Method	22
3.6.2 Modified Subtraction Method	22
3.6.3 Reciprocity Method	24

4	Inverse Problem	27
4.1	Lead Field Matrix	28
4.2	Node Basis Lead Field Matrix	29
4.3	Element Basis Lead Field Matrix	29
4.4	Parametric Method	30
4.5	Computational Complexity	31
4.6	Choosing the Number of Sources	33
5	Particle Swarm Optimization	35
5.1	Original PSO	36
5.2	Improved PSO	37
5.3	PSO Drawbacks	38
5.4	The Modified PSO	38
5.4.1	Evolutionary Programming	39
5.4.2	The Concept of Authority	40
5.4.3	Adaptive Swarm Size	40
5.4.4	Problem-Specific Modification	41
5.5	Comparison of Different Algorithms	41
5.5.1	Results and Discussions	42
5.6	Multiple Source Localization	46
6	Head Model	49
6.1	MR Acquisition	50
6.2	MRI Segmentation Methods	50
6.2.1	FSL	50
6.2.2	Mean Shift Method	51
6.2.3	Manual Segmentation	52
6.3	Modeling Tissue Conductivity Anisotropy	52
6.3.1	Direct Mapping	54
6.3.2	Volume Normalized Mapping	55
6.4	Numerical Results	55
7	Real EEG Test Case	59
7.1	Somatosensory Evoked Potential	59
7.1.1	EEG Signal Preprocessing	61
7.2	Validation	61
7.2.1	Anatomical Validation	62
7.2.2	Functional Validation	63
7.2.3	Exhaustive Search	66
7.3	Result and Discussion	66

8	Summary of the Papers	69
8.1	Forward Problem: Papers I, VI and VII	69
8.2	Inverse Problem: Papers I, II and IX	70
8.3	Real EEG Data: Papers II, V and IX	70
8.4	Sensitivity Analysis: Papers III, IV and VIII	71
9	Conclusions and Outlook	73
	References	75

Part II: Included Papers **99**

Paper I: Application of Particle Swarm Optimization in Epileptic Spike EEG Source Localization

Paper II: Non-invasive EEG Source Localization using Particle Swarm Optimization: A Clinical Experiment

Paper III: Investigation of Brain Tissue Segmentation Error and its Effect on EEG Source Localization

Paper IV: Influence of Different Sources of Noise on Epileptic Spike EEG Source Localization

Paper V: Particle Swarm Optimization Applied to EEG Source Localization of Somatosensory Evoked Potentials

Paper VI: Evaluation of a Finite-Element Reciprocity Method for Epileptic EEG Source Localization: Accuracy, Computational Complexity and Noise Robustness

Paper VII: An Improved Method for Dipole Modeling in EEG-Based Source Localization

Paper VIII: On the Fully Automatic Construction of a Realistic Head Model for EEG Source Localization

Paper IX: Real-Time EEG Source Localization using Reciprocity Theorem and Particle Swarm Optimization

Notations

\mathbb{R}, \mathbb{R}^n	-Set of real positive numbers and set of n-dimension vectors
\mathbf{x}	-3-dimensional vector $\mathbf{x} = (x_1, x_2, x_3)^T$
\mathbf{E}	-Electric field intensity (V/m)
\mathbf{D}	-Electric displacement (C/m ²)
\mathbf{H}	-Magnetic field intensity (A/m)
\mathbf{B}	-Magnetic flux density (T = Vs/m ²)
\mathbf{j}	-Electric current density (A/m ²)
\mathbf{M}	-Dipole moment (Cm = Ams)
ρ	-Electric charge density (C/m ³)
μ	-Magnetic permeability (Vs/Am)
σ	-Electric conductivity (S/m = A/Vm)
ε	-Electric permittivity (As/Vm)
\mathbf{A}	-a matrix
\mathbf{A}^T	-Transpose of \mathbf{A}
\mathbf{A}^{-1}	-Inverse of \mathbf{A}
δ	-delta function
e_i	- i^{th} unit vector
$\ \cdot\ $	-Euclidean norm
∇	-Gradient
Δ	-Laplace operator
$\nabla \cdot$	-Divergence operator
$\nabla \times$	-Curl operator (also: rot)
Φ	-Scalar electric potential
χ	-A smooth cut-off function
T	-The number of time points
N	-The number of FE nodes
N_{elec}	-The number of EEG electrodes
N_{cell}	-The number of cells
p	-Dipole source model: The number of sources
$\Omega, \partial\Omega$	-Closed bounded domain and its boundary

$\hat{\mathbf{n}}$	-3D unit vector normal to a boundary
G	-Green's function
\bar{d}	-mean of the vector \mathbf{d}
$n!$	-Factorial of $n = 1 \times 2 \times \cdots \times (n-1) \times n$
φ	-Finite element basis function
\mathbf{K}	-Finite element stiffness matrix
\mathbf{u}	-Finite element unknown function
\mathbf{b}	-Finite element right-hand side
\mathbf{L}	-Lead field matrix
\mathbf{R}	-Restriction matrix
\mathbf{T}	-Transfer matrix
\mathbf{u}_{elec}	-The electrode potentials
W_p^q	-Sobolev space

Abbreviations and Acronyms

CSF	Cerebrospinal Fluid
CT	Computed Tomography
DT	Diffusion Tensor
EEG	ElectroEncephaloGraphy
FE	Finite Element
FOV	Field Of View
fMRI	functional Magnetic Resonance Imaging
GM	Gray Matter
GMG	Geometric Multi-Grid
MAG	MAGnification factor
MR	Magnetic Resonance
MRI	Magnetic Resonance Imaging
PSO	Particle Swarm Optimization
PET	Positron Emission Tomography
ROI	Region of Interest
RDM	Relative Difference Measure
SEP	Somatosensory Evoked Potential
SNR	Signal-to-Noise Ratio
SPECT	Single Photon Emission Tomography
T1-MRI	T1-weighted MRI
TE	Echo Time
TR	Repetition Time
WM	White Matter

Part I
Introductory Chapters

Introduction

Epilepsy is one of the most common neurological diseases, and is present in up to 1% of the world's population. Many patients with epilepsy never receive the treatment which make them seizure free; consequently, treatment of epilepsy by medications is a major challenge, according to the World Health Organization [1]. Surgical therapy has become an important therapeutic alternative for patients with drug resistant epilepsy. In a consensus definition proposed by the International League Against Epilepsy (ILAE), the drug resistant epilepsy is defined as *failure of adequate trials of two tolerated and appropriately chosen and used antiepileptic drugs (AED) schedules (whether as monotherapies or in combination) to achieve sustained seizure freedom* [2].

Although intracranial surgery involves inherent risks, these risks are smaller than the risks of uncontrolled seizures. The morbidity and mortality of seizures include the following [1]:

- Accidental injury, commonly including fractures, burns, dental injuries, lacerations, and head injuries.
- Cognitive decline and memory loss, which over time has been demonstrated to occur in patients.
- Sudden unexplained death in epilepsy (SUDEP) that can reach a rate of one death per 500 patients per year.
- Psychological, social, and vocational impairment.

Considering the above factors, a continued pharmacological therapy after failure to control seizures with several trials of antiepileptic drugs, is not always an effective treatment. Moreover, Engel [3] shows that the benefits of anteromedial temporal lobe resection (AMTR) for disabling complex partial seizure, are greater than continued treatment with AEDs, and the risks are at least comparable. In addition, surgery yields a better quality of life and reduces depression and anxiety

as early as three months after temporal resection, compared with continued pharmacological therapy [4].

The heterogeneity of focal epilepsy across patients demands an extensive multimodal approach to focus localization [5]. Generally, results of at least three standard investigative modalities, conducted in series, are required to concur before surgery can be planned. Standard modalities are: reported clinical seizure semiology; electroencephalography (EEG) or electrocorticography (ECoG) seizure onset location combined with videoderived seizure semiology; structural MRI (sMRI); and nuclear imaging techniques. Nuclear imaging detects abnormality in ictal, during an actual seizure, versus interictal, period between seizures, blood flow by single photon emission computed tomography (SPECT), and/or abnormality in interictal glucose metabolism by positron emission tomography (PET). The localization performance of these methods is validated by comparison with post-surgical outcomes.

Only when a well-defined structural lesion agrees with seizure semiology and scalp EEG onset with or without radiotracer techniques, can surgery be planned without invasive study. Structural MRI locates brain lesions in about 70-80% of focal epilepsy [6]. In other cases, intracranial electrode placement is often considered. When the lesion is located, but is close to eloquent cortex such as basal temporal area, primary motor area, primary sensory area and primary visual area, fMRI and invasive studies help to minimize resection of such tissue. However, a visualized lesion may not represent the entire seizure-generating region. Underestimating the extent of the region can result in the re-occurrence of seizures following resective surgery. Overestimating the extent of the region holds an increased risk of functional deficits. Correct and anatomically precise localization of the epileptic focus, preferably with non-invasive methods, is the main goal of the pre-surgical epilepsy diagnostic procedure. The current techniques have limited accuracy and are therefore associated with significant risks. Hence, there is a need for improved, complementary, time-efficient, non-invasive methods to define the seizure-generating focus.

The neurophysiological analysis of the EEG data is a time consuming and rather cumbersome process involving several steps where the data is converted between different systems. There is therefore great need for modern computer-based tools that could determine the location of the epileptic focus more accurately than possible by simple visual inspection and also facilitate an automation of the whole procedure to reduce the manual neurophysiological analysis. The pre-surgical workup would be shortened and ultimately more patients could be identified that would benefit from surgery.

1.1 EEG Source Localization

The EEG is the most important diagnostic tool used at epilepsy surgery centers. The first human EEG was recorded in 1924 by Hans Berger [7]. The activity that is measured in an EEG is the result of movements of ions, the so-called *primary currents*, within activated regions in the cortex of the human brain. This brain activity is often modeled as a current dipole. It is shown in [8] that this current dipole is an acceptable approximation for modeling the neural activities in the brain. The current dipole represents a restricted area with synchronously active pyramidal cells located in the gray matter of the cortex, see Chapter 2. The EEG source localization method localizes epileptic electrical activity, called interictal epileptiform discharges (IEDs), such as in spike waveforms. IEDs occur between seizures and most often are closely linked to the site of the seizure focus. In contrast to the electrographic activity during seizures, IEDs do not cause patient movement artifacts in an MRI scanner, which is advantageous to data acquisition and analysis. However, in visual analysis of the EEG (precise) localization of IEDs are coarse.

The procedure of the EEG source localization deals with two problems. First, the forward problem to find the scalp potentials for a given current dipole(s) inside the brain, and second the inverse problem to estimate the source(s) that fits with the given potential distribution at the scalp electrodes. One of the major advantages of EEG source localization compared to other brain imaging modalities is its high temporal resolution.

The simple, and still the most commonly used, head models in the forward problem describe the head by three or four spherical layers, representing scalp, skull, cerebrospinal fluid (CSF) and brain. In each of these layers, the conductivity is assumed to be isotropic and homogeneous. The advantage of spherical models is that the scalp potential generated by dipolar sources can be computed analytically by using series expansion formulas [9]. It is known that five tissue compartments, i.e., gray matter, white matter, CSF, skull and scalp are the most important tissues for EEG source localization [10, 11]. For a finer discrimination the scalp layer may also be divided into fat and muscle compartments. These tissues have different conductivities [12]. The human skull consists of a soft bone layer (spongiosa) enclosed by two hard bone layers (compacta). Since the spongiosa has a much higher conductivity than the compacta [13], the skull shows a direction-dependent (anisotropic) conductivity. A ratio of 1 to 10 has been measured for the radial and tangential direction to the skull surface [14]. The brain white matter has an anisotropic conductivity with a ratio of about 1:9 (normal:parallel to fibers) [15]. However, although no direct technique exists for robust and non-invasive measurement of the conductivity properties, recently the

relation between the effective electrical conductivity tensor of brain tissue and the effective water diffusion tensor, as measured by Diffusion Tensor MRI (DT-MRI), was formulated [16–19]. The underlying assumption is that the same structural features that result in anisotropic mobility of water molecules, which can be detected by DT-MRI, also result in anisotropic conductivity. Basser et al., [16] showed that the eigenvectors of the conductivity tensor are the same as those from the water diffusion tensor.

The influences of volume conductor inhomogeneities and head model simplifications on EEG analysis, have been studied by various authors (see, for example, [20–24]). Using the spherical model instead of a patient-specific model in EEG source localization, may cause errors in the range of 10 – 30 mm [20, 21]. Moreover, in [22, 25], it is shown that holes in the skull, for instance in patients with trepanned skull (boring, cutting, and scraping open holes in a human skull), have a non-negligible effect on EEG source localization. In [22], it is also shown that it can be important to model inhomogeneities of the brain compartment, since simulated fields are especially sensitive to local conductivity changes around the source [26]. With regard to skull anisotropy, van den Broek et al., in [22], showed a smearing effect on the forward problem, and Marin et al., in [23], showed a non-negligible impact on the inverse problem for certain inverse methods of the distributed source model approach. Moreover, white matter conductivity anisotropy has been shown to have an influence on the forward problem [24].

Finite Element (FE) head models, developed by various research groups (see [22, 23, 27, 28]), are able to handle both realistic geometries and inhomogeneous and anisotropic material parameters. However, the critical issue for the forward problem is how to deal with the computational complexity of the FE model with regard to the inverse problem. Iterative solvers, like the preconditioned conjugate gradient (PCG) method with conventional preconditioners, have been used for solving the large linear FE equation system. The repeated solution of such a system with a constant geometry and varying right hand sides (the sources), sometimes more than a thousand times, is the major time consuming part of the source localization process. These computational times limit the resolution of the models in the practical use of EEG source localization. It has been shown in recent studies [29, 30] that algebraic multigrid preconditioners (AMP) and parallel computing can be used to obtain reasonable simulation times.

Inverse EEG source localization is the process of finding one or several sources, given the EEG potentials measured by the electrodes at the scalp. The number of EEG electrodes is usually between 30 – 100 and in some cases as many as 200. In [31], it is shown that the most important step for selecting the number of EEG electrodes is the increase from 31 to 63 electrodes, whereas increasing from 63 to 123 electrodes only improves the source localization results marginally. In comparison to the number of electrodes, the number of possible source locations is

much larger. Thus, the solution of the inverse problem is generally not unique in the sense that many dipole source configurations can result in the same EEG. To attain uniqueness, it is necessary to impose *a priori* knowledge on the source distribution. The different methods to solve the EEG source localization problem are traditionally categorized into parametric (dipole or continuous) and non-parametric (distributed or discretized) methods. The main difference between these two methods is whether a fixed number of dipoles is assumed *a priori* or not. The non-parametric methods act on a distributed source model, where the restriction to a limited number of focal sources is removed. On the other hand parametric methods are often well suited for estimating the current dipole used to represent the well-localized activated neural sources for events like epileptic spikes and evoked potentials (EPs) [8, 32].

The clinical use of the dipole [33] and distributed [34] EEG source localization have been examined in benign focal epilepsy of childhood with centrotemporal spikes (BFEC) and mesial temporal lobe epilepsy (MTLE). For both groups, Plummer in [35] showed that the moving-regularized and the rotating-non regularized dipole models with a single dipole, and the standardized low-resolution electromagnetic tomography (sLORETA) distributed method [36] constrained to cortex using rotating sources, had robust and clinically meaningful results. In [33] and [34] EEG source localization approaches were tested for a single time point at the spike peak. Plummer concluded that the dipole and distributed EEG source localization are complementary and furthermore single dipole models are often sufficient for epileptic spike source localization. If multiple dipoles (see [37–39]) or a whole current distribution (see [40–42]) are assumed to underlie the measured potentials, the inverse problem remains ill-posed. It is therefore interesting to investigate how sensitive single dipole fit methods are to model inaccuracies.

Despite the fact that intraspikes propagation may occur, the peak of the spike is often used as an indicator of the site of ictal onset. EEG source localization should ideally include the spike onset-to-peak epoch; Lantz in [43] showed that the EEG source localization result at the midpoint of the spike upswing, is more reliable to identify the putative epileptogenic lesion when less propagation has occurred (vs. the spike peak). In [35] this result was confirmed and additionally demonstrated that this applies to both dipolar and distributed EEG source localization, in both BFEC and MTLE. Recently, in EEG source localization the question of localization for single versus averaged IEDs, has been raised. Automated spike averaging is standard practice in EEG source localization studies; the assumption is that electrically averaging identical spikes will increase signal-to-noise ratio (SNR) and optimize the localization solution. Plummer in [35] showed that the single-to-averaged IED localization disagreement can be high. On the other hand, [44] showed that the spike locations computed from different trials of the same electrodes are closely located.

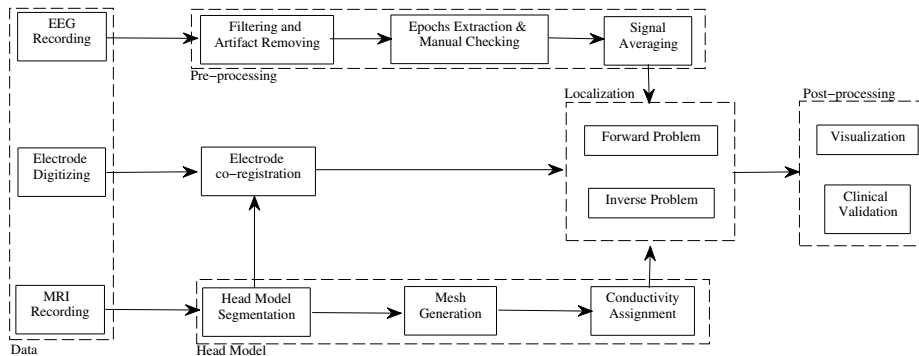


Figure 1.1: The different steps in the EEG source localization procedure.

Source localization is heavily dependent on how the current dipole is modeled and how the computations are performed and several different alternatives have been suggested in the literature [45,46]. Also the localization accuracy is affected by different factors including, segmentation error [47], EEG signal noise [11], electrode misplacements [11,48,49], conductivity noise [11] and tissue anisotropy [50], as well as the numerical computational error. As mentioned earlier, one of the major limitations in EEG-based source reconstruction has been the poor spatial accuracy, which is due to low resolution of previous EEG systems and the use of simplified spherical head models. Thus, source localization requires an accurate and robust solution of the inverse problem with realistic computational effort for the forward problem. EEG-based source localization is an active field of research [51,52], but partly due to the aforementioned shortcomings, the new computational techniques are often not part of the standard pre-surgical diagnostic workup. In Waberski et al. [53], it is concluded that to achieve the final goal of general clinical use, fast and automatic techniques with improved head modelling by finer discretization, and more accurate representation of the conductivities for the narrow anatomical relationship between the cerebral cortex and the complex shaped skull in the region of the temporal lobe, are necessary.

As described in the following, this thesis addresses three important questions in EEG source localization; how to decrease the computational complexity, how to handle anisotropy in the forward problem and the physiological and anatomical constraints in the inverse problem, and how different sources of noise influence the results.

1.2 Overview of the Thesis

The EEG source localization has several different sub-problems that each should be treated carefully. Fig. 1.1 illustrates all necessary steps performed in the EEG source localization procedure. The thesis is organized as follows. A short description of the physics of the EEG is presented in Chapter 2. Chapter 3 contains the description of the forward problem. In this chapter, two methods are proposed for modeling the dipole source that can handle the head model complexity and reduce the computational time for the forward problem. Chapter 4 contains the description of the inverse problem and an overview of different techniques for solving it. Chapter 5 introduces a new algorithm for parametric source localization, based on particle swarm optimization (PSO), for solving the epileptic spike EEG source localization. Chapter 6 deals with the head model generation and white matter anisotropy. In Chapter 7, a real EEG test case is presented. Chapter 8 contains a summary of the appended papers. Finally, the conclusions and an outlook are presented in Chapter 9. Part **II** of this thesis includes Papers which are published/submitted, based on material presented in the thesis.

The Physics of EEG

To understand which activity in the brain we actually capture by the EEG electrodes, one needs to look closer at the microscopic level. In this section the physiology of the EEG will be briefly described. This is important to be familiar with the underlying mechanisms of the EEG for modeling the forward problem.

2.1 Neurophysiology

The brain consists of approximately 20 billion [55] nerve cells or neurons. Neurons are capable of generating and transmitting electrochemical impulses. There are many different kinds of neurons, but they all have the same basic structure. The **soma** or **cell body** contains the nucleus of the cell and is essential for the continuing life of the neuron. The **dendrites**, arising from the soma, are specialized in receiving inputs from other nerve cells; a neuron may have several dendrites. Via the **axon**, impulses are sent to other neurons; a neuron has only one axon. The axon's end is divided into branches which form **synapses** with other neurons, see Fig. 2.1. The synapse is a specialized interface between two nerve cells. The synapse consists of a cleft between a pre-synaptic and post-synaptic neuron. At a synapse, between the axon of one neuron and the dendrite or cell body of the next neuron, impulse transmission depends upon chemicals called neurotransmitters. Further readings on the anatomy of the brain can be found in [56,57].

At rest the intracellular environment of a neuron is negatively polarized at ap-

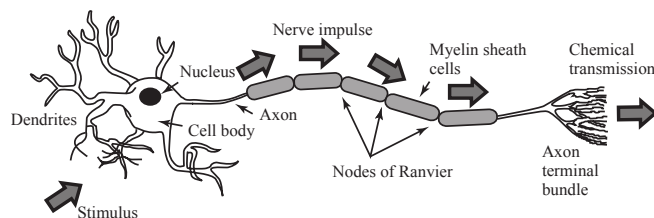


Figure 2.1: Structure of a neuron (adopted from Attwood and MacKay [54])

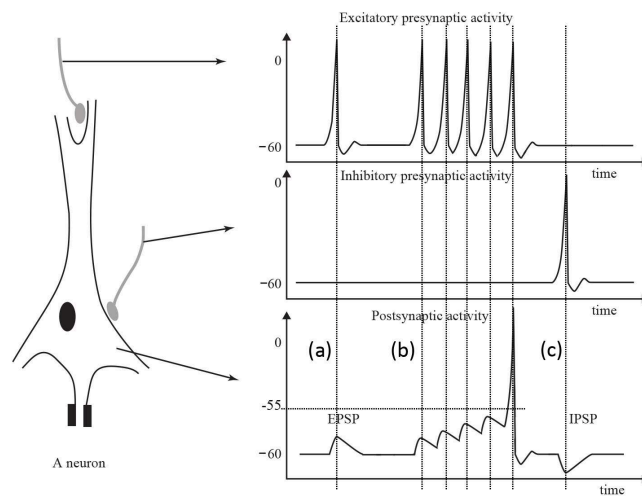


Figure 2.2: The neuron membrane potential changes and current flow during synaptic activation, recorded by means of intracellular microelectrodes. Action potentials in the excitatory and inhibitory presynaptic fibre respectively lead to EPSP and IPSP in the postsynaptic neuron (adopted from Saeid Sanei and J.A. Chambers [58])

proximately -70 mV compared with the extracellular environment. The potential difference is due to an unequal distribution of Na^+ , K^+ and Cl^- ions across the cell membrane. This unequal distribution is maintained by the Na^+ and K^+ ion pumps located in the cell membrane [56]. The neuron's task is to process and transmit signals. This is done by an alternating chain of electrical and chemical signals. Active neurons secrete a neurotransmitter, which is a chemical substance, at the synaptical site. The synapses are mainly localized at the dendrites and the cell body of the post-synaptic cell. The neurotransmitter in contact with the receptors changes the permeability of the membrane for charged ions. Many synapses are termed excitatory, because the neurotransmitter causes the post-synaptic neuron to depolarize (become less negative inside as Na^+ ions enter the cell) and transmit an electrical impulse to another neuron, muscle cell, or gland. In other words, depolarization means that the potential difference between the intra- and extracellular environment decreases. This depolarization is also called an excitatory post-synaptic potential (EPSP), marked by (a) in Fig. 2.2. On the other hand, some synapses are inhibitory, meaning that the neurotransmitter causes the post-synaptic neuron to hyperpolarize (become even more positive outside as K^+ ions leave the cell or Cl^- ions enter the cell) and therefore not transmit an electrical impulse. This potential change is also called an inhibitory post-synaptic potential (IPSP), marked by (c) in Fig. 2.2. There are a large number of synapses from

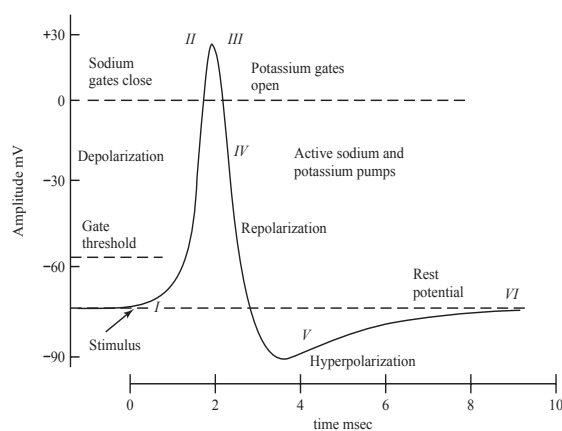


Figure 2.3: Changing the membrane potential for a giant squid axon by closing the Na channels and opening K channels (adopted from Ka Xiong Charand [62])

different pre-synaptic neurons in contact with one post-synaptic neuron. Fig. 2.2 shows the membrane changes recorded by means of intracellular microelectrodes. At the cell body all the EPSP and IPSP signals are integrated. When a net depolarization of the intracellular compartment at the cell body reaches a certain threshold, between -55 and -50 mV, an action potential is generated [59], marked by (b) in Fig. 2.2. Fig. 2.3 shows an example of the above activities schematically for a giant squid axon. An action potential then propagates along the axon to other neurons [60, 61].

2.2 The Generators of the EEG

One neuron generates a small amount of electrical activity. This small amount cannot be picked up by surface electrodes, as it is overwhelmed by other electrical activity from neighboring neuron groups. When a large group of neurons is simultaneously active, the electrical activity is large enough to be picked up by the electrodes at the surface, thus generating the EEG signals. The electrodes used in scalp EEG are large and remote. They only detect the summed activities of a large number of neurons which are synchronously electrically active. The action potentials can be large in amplitude (70 – 110 mV) but they have a short duration (2 ms). A synchronous firing of action potentials of neighboring neurons is unlikely. The post-synaptic potentials are the generators of the extracellular potential field which can be recorded with an EEG. Their time course is larger (10 – 20 ms) which enables summed activity of neighboring neurons. However their amplitude is smaller (0.1 – 10 mV) [61, 63]. The EEG reflects the electrical

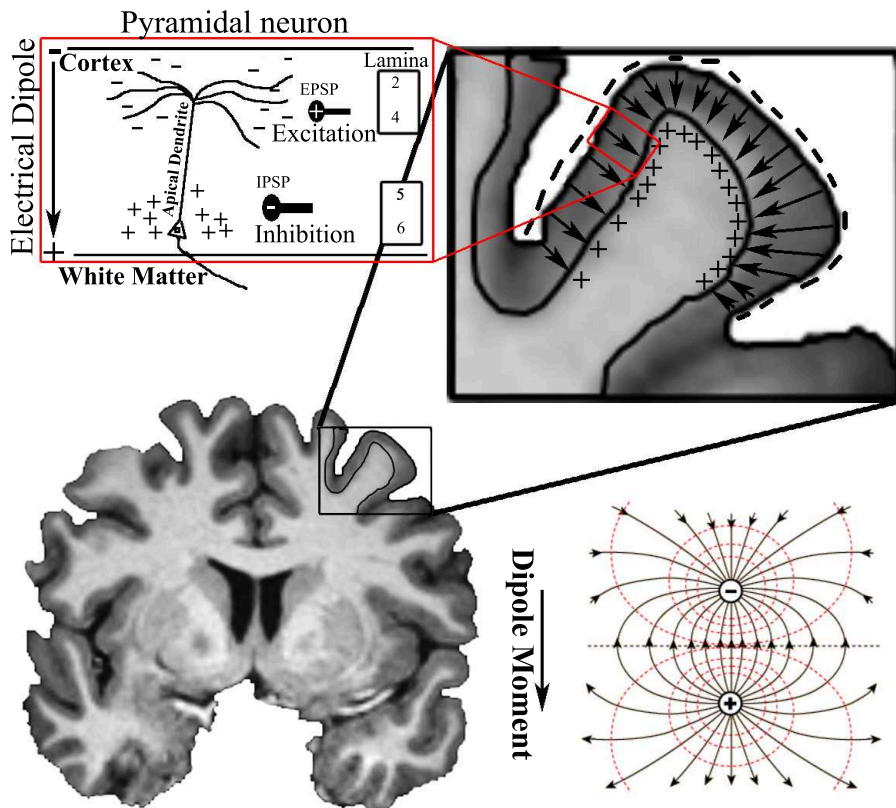


Figure 2.4: Schematic of a brain cross section, illustrating representative cortical EEG sources where dipoles are added to a cortical layer, a pyramidal neuron cell and dipole electric field and its equipotential lines. (designed by Anders Hedström)

activity of a subgroup of neurons, especially pyramidal neuron cells, where the apical dendrite is systematically oriented orthogonal to the brain surface. Fig. 2.4 illustrates a coronal view of a brain where dipoles are added to the cortical layer, a pyramidal neuron cell and the dipole electric field and its equipotential lines.

Forward Problem

3.1 Poisson's Equation

As mentioned in Chapter 2, the EEG reflects the electrical activity of a subgroup of neurons, especially pyramidal neuron cells, where the apical dendrite is systematically oriented orthogonal to the brain surface. The characteristic frequencies of the signals in the kHz range and below, make the capacitive and inductive effects of the tissue negligible [64]. Therefore, the electric and magnetic fields can be described by the well known quasi-static Maxwell equations [65],

$$\nabla \cdot \mathbf{D} = \rho, \quad (3.1)$$

$$\nabla \times \mathbf{E} = 0, \quad (3.2)$$

$$\nabla \times \mathbf{B} = \mu \mathbf{j}, \quad (3.3)$$

$$\nabla \cdot \mathbf{B} = 0, \quad (3.4)$$

where \mathbf{D} is the electric displacement, μ is the magnetic permeability, ρ is the electric free charge density, \mathbf{H} and \mathbf{B} are the magnetic field and magnetic induction, respectively, \mathbf{E} is the electric field and \mathbf{j} is the electric current density. Moreover, the material equations are as follows,

$$\mathbf{D} = \varepsilon \mathbf{E}, \quad (3.5)$$

$$\mathbf{B} = \mu \mathbf{H}, \quad (3.6)$$

where ε is the electric permittivity. It can be assumed that μ is constant over the whole volume and is equal to the permeability of vacuum [37,64]. The irrotational nature of \mathbf{E} indicated by (3.2) enables us to define a scalar electric potential Φ , as follows:

$$\mathbf{E} = -\nabla \Phi. \quad (3.7)$$

The current density is generally divided into two parts [37], the so-called primary or source current, \mathbf{j}^s , and the secondary or return currents, $\sigma\mathbf{E}$,

$$\mathbf{j} = \mathbf{j}^s + \sigma\mathbf{E}, \quad (3.8)$$

where $\sigma \in \mathbb{R}^{3 \times 3}$ denotes the conductivity tensor which is dependent on position and given by,

$$\sigma = \begin{bmatrix} \sigma_{11} & \sigma_{12} & \sigma_{13} \\ \sigma_{21} & \sigma_{22} & \sigma_{23} \\ \sigma_{31} & \sigma_{32} & \sigma_{33} \end{bmatrix}, \quad (3.9)$$

with units $A/(Vm) = S/m$. There are tissues in the human head that have an anisotropic conductivity, e.g., white matter and skull. This means that the conductivity is direction dependent. For isotropic tissues the tensor matrix is a diagonal matrix and for anisotropic tissues it is a symmetric full rank matrix. If we denote the domain of interest as Ω (with boundary $\partial\Omega$), taking the divergence of (3.3) (divergence of a curl of a vector is zero) and using equations (3.7) and (3.8) we get the Poisson's equation

$$\nabla \cdot (\sigma \nabla \Phi) = \nabla \cdot \mathbf{j}^s \text{ in } \Omega, \quad (3.10)$$

with boundary condition

$$\hat{\mathbf{n}} \cdot (\sigma \nabla \Phi) = 0 \text{ on } \partial\Omega. \quad (3.11)$$

3.2 The Source Currents

As mentioned earlier, the primary currents \mathbf{j}^s are movements of ions within the dendrites of the large pyramidal cells of activated regions in the cortex sheet of the human brain. Various modeling possibilities for the primary currents, \mathbf{j}^s , are discussed in the literature [27, 66–68]. A simplified electrical model for this active cell consists of two current monopoles: a current sink at the apical dendrite side which removes positively charged ions from the extracellular environment, and a current source at the cell body side which injects positively charged ions in the extracellular environment. This model can be written mathematically as follows,

$$\mathbf{j}^s(\mathbf{x}) := I_0 \left[\delta(\mathbf{x} - \mathbf{x}_0 + \frac{d\bar{\mathbf{e}}}{2}) - \delta(\mathbf{x} - \mathbf{x}_0 - \frac{d\bar{\mathbf{e}}}{2}) \right] \quad (3.12)$$

where \mathbf{x}_0 and I_0 are the midpoint and the current between two monopolar sources, respectively, d is a distance between two monopolar sources and $\bar{\mathbf{e}}$ is the unit vector from the negative charge to the positive charge. δ is the Dirac delta function

with $\int_{\Omega} \delta dV = 1$. Nunez in [68] showed that 2 mm distance between source and sink can be seen as realistic.

Another model for the source current is the so-called *mathematical dipole* which is formulated as

$$\mathbf{j}_{\text{Math}}^s(\mathbf{x}) = \mathbf{M}\delta(\mathbf{x} - \mathbf{x}_0), \quad (3.13)$$

where \mathbf{x}_0 is the source position and $\mathbf{M} \in \mathbb{R}^3$ is the dipole moment. It is shown in [8] that this current dipole is an acceptable approximation for modeling the neural activities in the brain. This source model has a singularity at \mathbf{x}_0 which is treated differently in the numerical approaches.

3.3 EEG Forward Problem

The EEG forward problem defined in (3.10) and (3.11), is to find the potential in the EEG electrode positions for the given current source(s) inside the brain. Assume Φ satisfies (3.10) for a given primary source \mathbf{j}^s . As the gradient of a constant function is zero then any function $\Phi + C$ satisfies (3.10), where C is a scalar constant. To make the solution of (3.10) unique we introduce a reference electrode and enforce its potential to zero, i.e.,

$$\Phi(\mathbf{x}_{ref}) = 0. \quad (3.14)$$

Then we calculate the solution relative to this reference electrode. Since only the relative difference of the potentials are of interest, it is common in EEG to use the average signals as a common reference,

$$\sum_{k=1}^{N_{\text{elec}}} \Phi(\mathbf{x}_k) = 0. \quad (3.15)$$

Thus, the Poisson's equation can be re-written as,

$$\nabla \cdot (\sigma \nabla \Phi) = \nabla \cdot \mathbf{j}^s \text{ in } \Omega, \quad (3.16)$$

subject to the conditions

$$\left\{ \begin{array}{l} \hat{\mathbf{n}} \cdot (\sigma \nabla \Phi) = 0 \text{ on } \partial\Omega, \\ \text{Either (3.14) or (3.15)}. \end{array} \right. \quad (3.17)$$

Additionally, for existence and uniqueness of the solution of (3.16–3.17), the *compatibility condition*

$$\int_{\Omega} \nabla \cdot (\sigma \nabla \Phi) dV - \int_{\partial\Omega} \hat{\mathbf{n}} \cdot (\sigma \nabla \Phi) dS = 0, \quad (3.18)$$

that follows from Gauss's theorem has to be fulfilled.

3.4 Solving the Forward Problem: Green's Function

Using Green's function provides a way to write the solution of a partial differential equation in closed form, as an integral over distributed sources, e.g., Poisson's equation with a charge density source [65]. The physical reasoning underlying the mathematical technique is that any distributed source can be considered as a sum or integral over elemental sources. Let G be the Green's function that satisfies

$$-\nabla \cdot (\nabla G(\mathbf{x})) = \delta(\mathbf{x}) \quad (3.19)$$

along with the boundary condition that G approaches 0 at infinity where

$$G(\mathbf{x}) = \frac{1}{4\pi|\mathbf{x}|}. \quad (3.20)$$

Physically the Green's function shows the effect in \mathbf{x} due to a source in \mathbf{x}_0 . We may write the general solution to Poisson's equation in an unbounded space in terms of the Green's function, as

$$\Phi(\mathbf{x}) = \int G(\mathbf{x} - \mathbf{x}_0) f(\mathbf{x}_0) dV(\mathbf{x}_0), \quad (3.21)$$

where $f = \nabla \cdot \mathbf{j}^s$. We are especially interested in the potential solution at the EEG electrodes, N_{elec} , on the scalp. If we want to compute only $\Phi(\mathbf{x}_k)$; $k = 1, \dots, N_{\text{elec}}$ the explicit formula (3.21) is suitable, since we can easily choose to compute Φ in only a few points;

$$\Phi(\mathbf{x}_k) = \int_{\Omega} G(\mathbf{x}_k - \mathbf{x}_0) f(\mathbf{x}_0) dV(\mathbf{x}_0). \quad (3.22)$$

The discrete Green's function is an analogy of the lead field matrix, which will be discussed in the next Chapter.

The potential field in an infinite conductor generated by a current dipole with dipole moment $\mathbf{M} = q\mathbf{d}$ (q is the monopole charge and \mathbf{d} is the vector from the

negative charge to the positive charge) at position \mathbf{x}_0 can be derived using Green's solution

$$\Phi^\infty(\mathbf{x}) = \frac{1}{4\pi\sigma^\infty} \frac{(\mathbf{x} - \mathbf{x}_0) \cdot \mathbf{M}}{|\mathbf{x} - \mathbf{x}_0|^3}, \quad (3.23)$$

where σ^∞ is the conductivity.

The first volume conductor models of the human head consisted of a homogeneous sphere [69]. When it was found that the skull tissue has significantly lower conductivity than the scalp and brain tissue a three shell concentric spherical head model was introduced. In this model, illustrated in Fig. 3.1, the inner sphere represents the brain, the intermediate layer represents the skull and the outer layer represents the scalp. For this geometry a semi-analytical solution of Poisson's equation exists [70, 71]. There are also semi-analytical solutions available for layered spheroidal anisotropic volume conductors [72, 73]. Here the conductivity in the tangential direction can be chosen differently from the radial direction.

As we mentioned in Chapter 1, using the spherical head model instead of a patient-specific model in EEG source localization may cause significant errors with respect to the source position. Thus there is a need for accurate head modeling with realistic shape and conductivity properties. Finite element methods are well-suited for handling the head model complexity. An important consideration in finite element methods is how to represent the dipole source in the model, which is treated in the following sections. Here, we restrict the element types to cubical voxels since they are obtained from CT or MRI images.

3.5 Finite Element Method

The finite element method (FEM) is a standard tool for solving differential equations in many disciplines, e.g., electromagnetics, solid and structural mechanics, fluid dynamics, acoustics, and thermal conduction. Jin [74, 75] and Peterson [76] give good accounts of the FEM for electromagnetics. For the discretization of the EEG forward problem we begin by deriving the weak formulation. Multiplying Poisson's equation (3.16) by a test function $v \in W_2^1(\Omega)$ and integrating over Ω :

$$\int_{\Omega} v \nabla \cdot (\sigma \nabla \Phi) dV = \int_{\Omega} v f dV, \quad (3.24)$$

where $f = \nabla \cdot \mathbf{j}^s$ and W_2^1 is the Sobolev space. Next, integrate by parts using the identity

$$\nabla \cdot [v(\sigma \nabla \Phi)] = \nabla v \cdot (\sigma \nabla \Phi) + v \nabla \cdot (\sigma \nabla \Phi) \quad (3.25)$$

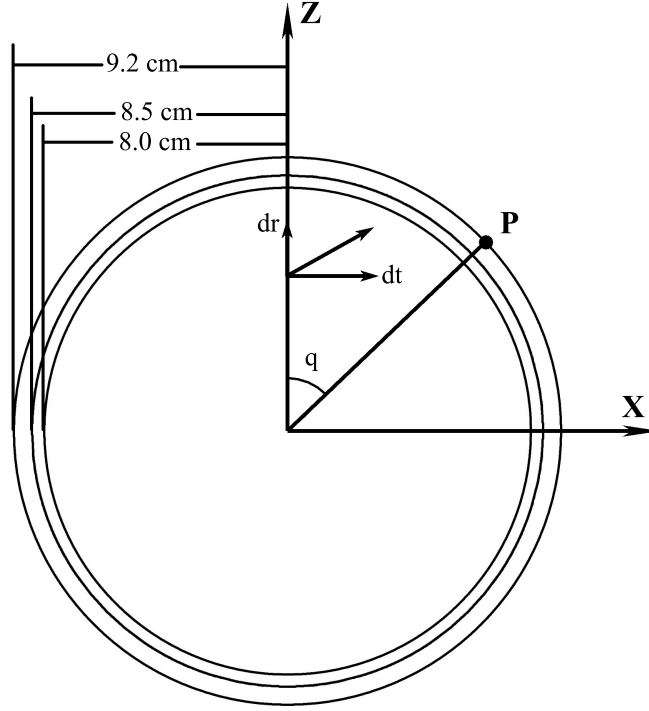


Figure 3.1: The three-shell concentric spherical head model. The dipole is located on the z-axis and the potential is measured at scalp point P.

and Gauss's theorem in 3D:

$$\int_{\Omega} \nabla \cdot \mathbf{F} dV = \int_{\partial\Omega} \hat{\mathbf{n}} \cdot \mathbf{F} dS, \quad (3.26)$$

with $\mathbf{F} = v(\sigma \nabla \Phi)$. This gives the weak form of (3.16):

$$-\int_{\Omega} \nabla v \cdot (\sigma \nabla \Phi) dV + \int_{\partial\Omega} \hat{\mathbf{n}} \cdot (\sigma \nabla \Phi) dS = -\int_{\Omega} \nabla v \cdot (\sigma \nabla \Phi) dV \quad (3.27)$$

$$= \int_{\Omega} v f dV, \quad (3.28)$$

where we have used the boundary condition (3.17).

For the discretization we restrict the element types to cubical voxels with node basis function, φ_j , centered at the mesh points ξ_j , φ_j equals one at node j and zero at all other nodes. An approximation to the potential is then represented in the FE

space $S = \text{span}\{\boldsymbol{\varphi}_j\}_{j=1}^N$ as

$$\Phi(\mathbf{x}) \approx \sum_{j=1}^N u_j \boldsymbol{\varphi}_j(\mathbf{x}), \quad (3.29)$$

where N is the number of FE nodes and u_j are the degrees of freedom (DOFs). After applying variational and FE techniques [77] to (3.16), we arrive at the system of linear equations

$$\mathbf{K}\mathbf{u} = \mathbf{b}, \quad (3.30)$$

where $\mathbf{K} \in \mathbb{R}^{N \times N}$ is a sparse symmetric positive definite stiffness matrix given by

$$K_{i,j} = \int_{\Omega} (\boldsymbol{\sigma} \nabla \boldsymbol{\varphi}_i) \cdot \nabla \boldsymbol{\varphi}_j \, dV, \quad (3.31)$$

$\mathbf{u} \in \mathbb{R}^N$ is the coefficient vector of the electric potential, and $\mathbf{b} \in \mathbb{R}^N$ is the right hand side vector,

$$b_i = - \int_{\Omega} \boldsymbol{\varphi}_i \nabla \cdot \mathbf{j}^s \, dV. \quad (3.32)$$

To get a unique solution we can use a reference electrode, i.e. letting

$$(\mathbf{u}_{\text{elec}})_{\text{ref}} = 0, \quad (3.33)$$

or constrain the mean value over all electrodes, i.e.

$$\sum_{k=1}^{N_{\text{elec}}} (\mathbf{u}_{\text{elec}})_k = 0. \quad (3.34)$$

Both these constraints can be incorporated by modifying the stiffness matrix \mathbf{K} . For (3.33) the row and column corresponding to the chosen electrode node are replaced such that they have a one for the electrode node position and zeros elsewhere. If (3.34) is to be used, \mathbf{K} is expanded by an extra row of ones at the bottom, a column of ones to the right, and a zero element in the lower right corner. In addition the right hand side vector \mathbf{b} is expanded by an additional element. Observe that both these modifications make \mathbf{K} invertible, read more about extending rank deficient linear systems in [78]. In the following section we describe three different methods to model the dipole source.

3.6 Source Modeling

3.6.1 Direct Method

In the direct method, a dipole source is embedded in the element basis functions [79,80]. The approximation can usually be improved by introducing more elements between the poles. An ideal dipole may be described as two point sources of opposite polarity with an infinitely large current and an infinitely small separation d ,

$$\nabla \cdot \mathbf{j}^s(\mathbf{x}) = \lim_{d \rightarrow 0} \frac{I_0}{d} \left[\delta(\mathbf{x} - \mathbf{x}_0 + \frac{d\bar{\mathbf{e}}}{2}) - \delta(\mathbf{x} - \mathbf{x}_0 - \frac{d\bar{\mathbf{e}}}{2}) \right]. \quad (3.35)$$

Substituting (3.35) into (3.32) gives

$$b_i^{\text{dir}} = \mathbf{M} \cdot \nabla \varphi_i(\mathbf{x}_0), \quad (3.36)$$

where $\mathbf{M} = I_0 d \bar{\mathbf{e}}$ is the dipole moment.

As can be seen from (3.36), \mathbf{b}^{dir} depends linearly on the dipole moment \mathbf{M} so we can write

$$\mathbf{b}^{\text{dir}} = \mathbf{b}^{\text{dir}}(\mathbf{x}_0, \mathbf{M}) = \mathbf{B}^{\text{dir}}(\mathbf{x}_0) \mathbf{M}, \quad (3.37)$$

where \mathbf{B}^{dir} is an $N \times 3$ matrix that depends on the dipole position \mathbf{x}_0 .

3.6.2 Modified Subtraction Method

As described in Section 3.2, the dipole source introduces a singularity that requires specific treatment to increase the modeling accuracy compared to the direct method. A subtraction method was first introduced by van den Broeh et al. [45] to circumvent this problem and then investigated in great detail in [22,28,30,80,81]. The total potential is split into two parts, a singularity potential (Φ^∞) and a correction potential (Φ^{corr}), as follows

$$\Phi = \Phi^\infty + \Phi^{\text{corr}}, \quad (3.38)$$

where Φ^∞ is the solution to (3.16) in an unbounded domain with constant conductivity σ^∞ as shown in (3.23). In [81] it is shown that the right hand side (RHS) is nonsingular if σ is constant in a small ball around \mathbf{x}_0 (Paper I). The RHS for the subtraction method has support whenever $\sigma \neq \sigma^\infty$. This means that the RHS must be assembled in each cell where this occurs. Here a modified subtraction method is presented that drastically reduces the number of non-zeros in the RHS to speed up the forward problem. Let

$$\Phi = \chi \Phi^\infty + \Phi^{\text{mod}} = F^\infty + \Phi^{\text{mod}}. \quad (3.39)$$

For convenience, we have defined the function

$$F^\infty = \chi \Phi^\infty, \quad (3.40)$$

where χ is a smooth cut-off function which is identically one in a neighborhood of \mathbf{x}_0 . In Paper VII a method for selecting a suitable choice of χ is presented. (Note: the Φ^{corr} notation is changed to Φ^{mod} because the cut-off function modifies this function as well). Using (3.38) and (3.10), the new formulation reads,

$$-\nabla \cdot (\sigma \nabla \Phi^{\text{mod}}) = \nabla \cdot (\sigma \nabla F^\infty) - \nabla \cdot \mathbf{j}^s \text{ in } \Omega, \quad (3.41)$$

subject to the conditions

$$\begin{cases} \hat{\mathbf{n}} \cdot (\sigma \nabla \Phi^{\text{mod}}) = -\hat{\mathbf{n}} \cdot (\sigma \nabla F^\infty) \text{ on } \partial\Omega, \\ \Phi(\mathbf{x}_{\text{ref}}) = 0. \end{cases} \quad (3.42)$$

Because of the homogeneity assumption we can find a subdomain Ω^∞ where the right hand side in (3.41) is identically zero. Thus the singularity of the right hand side of (3.16) is successfully eliminated by the subtraction approach and the RHS function in (3.41) is now square-integrable over the whole domain Ω and thus appropriate for FEM.

After applying variational and FE techniques to (3.41) with boundary conditions (3.42), we obtain the following system of linear equations:

$$\mathbf{K} \mathbf{u}^{\text{mod}} = \mathbf{b}^{\text{sub}} \quad (3.43)$$

where $\mathbf{K} \in \mathbb{R}^{N \times N}$ is given by (3.31), $\mathbf{u}^{\text{mod}} \in \mathbb{R}^N$ is the coefficient vector of the correction potential, and $\mathbf{b}^{\text{sub}} \in \mathbb{R}^N$ is the right hand side vector,

$$b_i^{\text{sub}} = \int_{\Omega} (\sigma \nabla \varphi_i) \cdot \nabla \Phi^\infty dV. \quad (3.44)$$

As can be seen from (3.23), Φ^∞ depends linearly on the dipole moment \mathbf{M} . Thus, the same holds for the right hand side vector \mathbf{b} and we can write

$$\mathbf{b}^{\text{sub}} = \mathbf{b}^{\text{sub}}(\mathbf{x}_0, \mathbf{M}) = \mathbf{B}^{\text{sub}}(\mathbf{x}_0) \mathbf{M}, \quad (3.45)$$

where \mathbf{B}^{sub} is an $N \times 3$ matrix that depends on the dipole position \mathbf{x}_0 .

After solving (3.43) numerically for Φ^{mod} , the unknown scalar potential Φ can be calculated using (3.38).

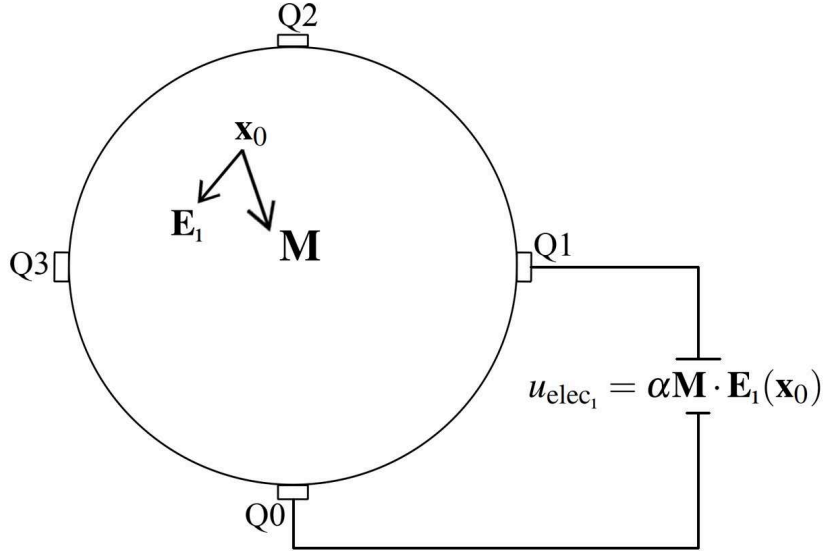


Figure 3.2: A system consisting of a simple domain in which the source with moment \mathbf{M} is located at \mathbf{x}_0 . The EEG measurements are performed with four electrodes, one of which is the reference electrode (Q_0).

3.6.3 Reciprocity Method

The reciprocity principle was introduced by Helmholtz [82] and then adapted to the EEG problem by Rush and Driscoll [83] when they proved the applicability of reciprocity to anisotropic conductors. The concept allows switching the role of the electrodes and dipole sources. Fig. 3.2 shows a simple 2D setup which consists of four electrodes mounted along the boundary of the EEG domain. One of these electrodes is used as a common reference for the measurements (ground). Hence, the output of the EEG measurements is the three voltages measured between one of the electrodes Q_1 , Q_2 , and Q_3 and the reference electrode Q_0 . These three voltages are denoted u_{elec_1} , u_{elec_2} , and u_{elec_3} .

We assume that a single source is present in the system. This source is defined by its position, \mathbf{x}_0 , and dipole moment (orientation and amplitude) \mathbf{M} . As we will be using reciprocity, we also define three distributions of electric fields in the domain, $\mathbf{E}_1(\mathbf{x})$, $\mathbf{E}_2(\mathbf{x})$, and $\mathbf{E}_3(\mathbf{x})$. These are the electric field distributions which are present in the system when we inject a unit current source to electrodes Q_1 , Q_2 , and Q_3 , respectively and withdraw a unit current at the reference electrode.

The theorem of reciprocity states that

$$u_{\text{elec}_i} = \alpha \mathbf{M} \cdot \mathbf{E}_i(\mathbf{x}_0). \quad (3.46)$$

In this expression, the constant α depends on several factors, such as whether we use a voltage or a current source to calculate \mathbf{E}_i as well as how the channels in the measurement system are set up. For simulated data in our system, $\alpha = 1$ (A^{-1}) when a unit current source is used to calculate \mathbf{E}_i . Rush and Driscoll, [83], have presented the proof of the reciprocity theorem for a general inhomogeneous anisotropic medium. The main assumption for their proof is that the conductivity tensor should be a symmetric tensor meaning that $\sigma_{12} = \sigma_{21}$, $\sigma_{13} = \sigma_{31}$, and $\sigma_{23} = \sigma_{32}$, which is the case for human anisotropic tissues. In Section 4.3 we show how the reciprocity theorem can be used for an efficient solution of the inverse problem.

Inverse Problem

Localization of the neural activity inside the brain based on the scalp EEG signals is called the EEG inverse problem. The solution of the inverse problem is generally not unique in the sense that many source configurations can result in the same EEG. To attain uniqueness, it is necessary to impose *a priori* knowledge on the source distribution, for example assumptions about the source model, anatomical and physiological constraints on the source region and sometimes even results from other brain imaging techniques, e.g., fMRI [84–87]. Different inverse approaches for discrete and continuous source parameter space have been proposed [27, 32, 37–39, 41, 88–93]. The inverse problem can be divided into two categories, parametric (dipole or continuous) and non-parametric (distributed or discretized) methods.

In the parametric methods a limited number of dipoles is assumed [37–39, 88]. Different spatio-temporal models exist depending on the number of dipoles assumed in the model and whether one or more of the dipole parameters, i.e., position, magnitude or orientation, are kept fixed or assumed to be known. In the literature [94, 95] one can find three models: a single dipole with time-varying unknown parameters (so-called *moving dipole*); dipoles with fixed positions and orientations but varying amplitudes (*fixed dipole*); fixed dipole positions but varying orientations and amplitudes (*rotating dipole*). In a case when only one single time, e.g., the spike peak, is chosen for the inverse problem, all these three models give the so-called *instantaneous state dipole* model [32]. In [8, 32], it is concluded that the instantaneous dipole model is suited for estimating the well-localized activated neural sources for events like epileptic spike and evoked potentials (EPs).

The non-parametric methods apply a distributed source model [36, 89–93, 96, 97], where the restriction to a limited number of focal sources is removed. To obtain a unique solution for the inverse problem it should be minimized with regard to a specific norm. Different norms have been proposed, such as the L2-norm [40, 89], leading to a smooth current distribution with minimal source energy and the L1-norm [90], which results in a more focal distribution [41]. Most distributed source models are instantaneous models, but recent works show that

spatio-temporal approaches can help to stabilize the inverse reconstruction process [92,93]. In the non-parametric methods, there are no need to model the dipole source in the same way as in the parametric methods, also the restriction about the number of sources is removed which are the main advantages of these methods. Moreover, because of computational simplicity, these methods have been widely adopted in empirical studies [41, 84, 98]. On the other hand, the resulting source distribution is less focal compared to the parametric methods [95]. In [99–102] some limitations of the parametric method have been investigated. In [102] it is shown that the linear inverse solutions are unable to produce adequate estimates of arbitrary current distributions at many brain sites. In [101] and [99] the authors claimed that while smoothness can be an effective constraint for retrieving isolated sources, it can fail for patterns with the same degree of smoothness but composed of multiple active sources.

4.1 Lead Field Matrix

The solution to the discrete EEG inverse problem on matrix form (3.30), is given by

$$\mathbf{u} = \mathbf{K}^{-1}\mathbf{b}. \quad (4.1)$$

In EEG applications, the potentials are typically measured at approximately 40 to 100 electrodes. These values can be obtained by multiplying \mathbf{u} with a *restriction matrix* $\mathbf{R} \in \mathbb{R}^{N_{\text{elec}} \times N}$ as follows,

$$\mathbf{u}_{\text{elec}} = \mathbf{R}\mathbf{u}. \quad (4.2)$$

Each row of \mathbf{R} has value one for the electrode node and zero elsewhere. (Note: assuming that the electrodes are located on FEM nodes.)

As mentioned in Chapter 3, the potential values \mathbf{u}_{elec} depends linearly on each of the dipole moment components $\mathbf{M} = (M_x, M_y, M_z)^T \in \mathbb{R}^3$. Therefore, the relationship between \mathbf{M} and the potential values \mathbf{u}_{elec} , can be described by a matrix operator $\mathbf{L} \in \mathbb{R}^{N_{\text{elec}} \times 3}$, the so-called *lead field matrix* that depends on the dipole position, head geometry and tissue conductivities. A column of \mathbf{L} is formed by calculating the forward problem at the EEG electrodes, N_{elec} , for a dipole at an arbitrary position, \mathbf{x}_0 , inside the brain with unit strength in one of the Cartesian directions. The three columns in \mathbf{L} represent the three orthogonal unit dipoles at the dipole position. If we assume a dipole with time-variant strength with T timepoints, $\mathbf{M} \in \mathbb{R}^{3 \times T}$, the EEG signals at electrode positions, \mathbf{U}_{elec} , can then be calculated very effectively by

$$\mathbf{U}_{\text{elec}} = \mathbf{L}\mathbf{M}, \quad (4.3)$$

where $\mathbf{U}_{\text{elec}} \in \mathbb{R}^{N_{\text{elec}} \times T}$.

The lead field matrix \mathbf{L} can then be used for the whole variety of inverse reconstruction methods; continuous or discretized. For the discretized space one can assemble the lead field matrix for all mesh nodes. Thus, the lead field matrix becomes $\mathbf{L} \in \mathbb{R}^{N_{\text{elec}} \times 3N}$ where each column of \mathbf{L} is formed by calculating the forward solution at the EEG electrodes, N_{elec} , for a dipole on one of the N mesh nodes with unit strength in a Cartesian direction, see Section 4.2. If the dipole moment is assumed to be known *a priori*, i.e., orthogonal to the gray matter surface, then $\mathbf{L} \in \mathbb{R}^{N_{\text{elec}} \times N}$.

4.2 Node Basis Lead Field Matrix

Since only the relative differences of the potential are of interest, it is common in EEG to use the average signal as a common reference, this is the so-called *average reference montage*. Let $\bar{\mathbf{R}}$ be the restriction matrix such that

$$\mathbf{u}_{\text{elec}} - \bar{\mathbf{u}}_{\text{elec}} = \bar{\mathbf{R}}\mathbf{u}, \quad (4.4)$$

where $\bar{\mathbf{u}}_{\text{elec}}$ is the average of the potential at all electrodes. $\bar{\mathbf{R}}$ can be obtained from \mathbf{R} by subtracting the column-wise mean from each entry. Substituting (4.1) in (4.4) gives

$$\mathbf{u}_{\text{elec}} - \bar{\mathbf{u}}_{\text{elec}} = \bar{\mathbf{R}}\mathbf{u} = \bar{\mathbf{R}}\mathbf{K}^{-1}\mathbf{b} = \bar{\mathbf{T}}\mathbf{b}. \quad (4.5)$$

We call $\bar{\mathbf{T}} = \bar{\mathbf{R}}\mathbf{K}^{-1} \in \mathbb{R}^{N_{\text{elec}} \times N}$ the *transfer matrix* for the average reference montage. By substituting (3.37) in (4.5),

$$\mathbf{u}_{\text{elec}} - \bar{\mathbf{u}}_{\text{elec}} = \bar{\mathbf{T}}\mathbf{B}^{\text{dir}}\mathbf{M}, \quad (4.6)$$

we can introduce the lead field matrix as $\mathbf{L}^{\text{dir}} = \bar{\mathbf{T}}\mathbf{B}^{\text{dir}}$ for the direct method. For the subtraction method, the contribution to the total potential comes from two parts, the finite element method computed by (3.43) and the direct contribution from (3.23), respectively. Thus, the lead field matrix is given by $\mathbf{L}^{\text{sub}} = (\bar{\mathbf{T}}\mathbf{B}^{\text{sub}} + \mathbf{F}_{\text{elec}}^{\infty})$. Here $\mathbf{F}_{\text{elec}}^{\infty}$ holds the value of Φ^{∞} for the three polarizations at all electrodes. This lead field formulation is the so-called *node basis* lead field matrix which is based on the divergence of the source current density vector at each node.

4.3 Element Basis Lead Field Matrix

As discussed earlier, the traditional method of constructing the \mathbf{L} matrix is to place three orthogonal sources in each node of the mesh, and compute the voltages at

the electrodes. For the reciprocity method, (3.46) holds for all electrodes and we obtain

$$\begin{bmatrix} E_{1,x}(\mathbf{x}_0) & E_{1,y}(\mathbf{x}_0) & E_{1,z}(\mathbf{x}_0) \\ E_{2,x}(\mathbf{x}_0) & E_{2,y}(\mathbf{x}_0) & E_{2,z}(\mathbf{x}_0) \\ \vdots & \vdots & \vdots \\ E_{N_{\text{elec}},x}(\mathbf{x}_0) & E_{N_{\text{elec}},y}(\mathbf{x}_0) & E_{N_{\text{elec}},z}(\mathbf{x}_0) \end{bmatrix} \begin{bmatrix} M_x(\mathbf{x}_0) \\ M_y(\mathbf{x}_0) \\ M_z(\mathbf{x}_0) \end{bmatrix} = \begin{bmatrix} u_{\text{elec}_1} \\ u_{\text{elec}_2} \\ \vdots \\ u_{\text{elec}_{N_{\text{elec}}}} \end{bmatrix} \quad (4.7)$$

which can be written in short as

$$\mathbf{L}^{\text{rec}}(\mathbf{x}_0)\mathbf{M} = \mathbf{u}_{\text{elec}}, \quad (4.8)$$

where

$$\mathbf{L}^{\text{rec}}(\mathbf{x}_0) = \nabla\mathbf{T}(\mathbf{x}_0) = \nabla(\mathbf{R}\mathbf{K}^{-1})(\mathbf{x}_0). \quad (4.9)$$

Here each row of \mathbf{R} has value 1 for the electrode node, -1 for the ground node, and zero elsewhere. The gradient is evaluated at the midpoint of all cells using the FEM basis functions. If we calculate (4.9) for all cells inside the domain and assemble the lead field matrix, we obtain the *element basis* lead field matrix $\mathbf{L}^{\text{rec}} \in \mathbb{R}^{N_{\text{elec}} \times 3N_{\text{cells}}}$ where N_{cells} is the number of cells. This lead field matrix maps dipole components placed at the elements to potentials at the scalp recording electrodes. So, rather than iteratively placing a source in every node and computing a forward solution at the electrodes, by using the reciprocity theorem the electric field in all of the elements is calculated. The calculated electric field then can be used to reconstruct the potential differences at the electrodes for a source placed in any element.

4.4 Parametric Method

In a parametric method, the number of dipoles is assumed to be fixed and their locations and moments are chosen such that the potentials at the electrodes, \mathbf{u}_{elec} , that are computed in the forward problem, closely approximate the measured potentials, \mathbf{u}_{meas} , according to some criteria. Here we follow the common practice and choose the parameters such that we have the best fit in the least squares sense. For one dipole at a specific instantaneous time we get the following minimization problem

$$J = \min_{\substack{\mathbf{x} \in \Omega_{\text{brain}} \\ \mathbf{M} \in \mathbb{R}^d}} \|\mathbf{u}_{\text{meas}} - \mathbf{L}(\mathbf{x})\mathbf{M}\|^2, \quad (4.10)$$

where Ω_{brain} is the brain domain and d the dimension. Since this is a least squares problem and the electrode potential depends linearly on the dipole moment, see

(4.3), it is convenient to separate the parameters in (4.10) and solve for the dipole moment \mathbf{M} first. Therefore, for a given dipole position $\mathbf{x} \in \Omega_{\text{brain}}$, the optimal components \mathbf{M}_{opt} are found in the least squares sense as the solution of the linear equations $\mathbf{u}_{\text{meas}} = \mathbf{L}(\mathbf{x})\mathbf{M}$, i.e.,

$$\mathbf{M}_{\text{opt}}(\mathbf{x}) = (\mathbf{L}^T(\mathbf{x})\mathbf{L}(\mathbf{x}))^{-1}\mathbf{L}^T(\mathbf{x})\mathbf{u}_{\text{meas}}. \quad (4.11)$$

Substituting (5.12) into (4.10) yields after some manipulation

$$J = \min_{\mathbf{x} \in \Omega_{\text{brain}}} \|\ [\mathbf{I} - \mathbf{L}(\mathbf{x})(\mathbf{L}^T(\mathbf{x})\mathbf{L}(\mathbf{x}))^{-1}\mathbf{L}^T(\mathbf{x})]\mathbf{u}_{\text{meas}} \|^2. \quad (4.12)$$

where \mathbf{I} is a $N_{\text{elec}} \times N_{\text{elec}}$ identity matrix.

Now, (4.12) is only dependent on the dipole position. Finding the minimum of (4.12) can be accomplished, for example, via an exhaustive search, i.e., inversion is carried out for each possible source location in the domain and the site producing the smallest residual energy is selected as the best possible source location. In the next Chapter we propose a new optimization method based on particle swarm optimization, to efficiently find the optimal source position.

4.5 Computational Complexity

In the set-up phase, \mathbf{T} is computed once per head-model by means of solving N_{elec} large sparse FE-systems of equations using, e.g., an iterative AMG-CG solver [29]. The computational complexity of the set-up phase is the same for all three numerical methods, i.e., direct, subtraction and reciprocity, if we ignore the cheap calculation of the gradient of \mathbf{T} , (4.9), in the reciprocity method. On our machine, a PC with Intel(R) Xeon(R) @3.30GHz CPU and 16GB memory, for solving $N_{\text{elec}} = 61$ FE-system for a model with $N = 2\,468\,080$ the set-up phase takes approximately 5 hours. The advantage of this pre-computation, which can be used by both parametric and non-parametric source methods, is that the solution of the inverse problem can then be computed very fast as part of an online process.

In the parametric inverse problem, a fixed number of active sources is assumed and in this approach, a search is made for the best-fit dipole position(s) and orientation(s). If we assume an unknown source direction, the time for finding the optimal source position and orientation is

$$r * \tau_{\text{inv}} = r * (\tau_{\mathbf{b}} + \tau_{\mathbf{M}_{\text{opt}}} + \tau_{\mathbf{u}_{\text{elec}}}) \quad (4.13)$$

in the inverse algorithm, where $\tau_{\mathbf{b}}$ is the time for assembling the right hand side vector. In the direct method, right hand side has eight non-zero entries, and the

Table 4.1: Inverse problem algorithms. Algorithm 1 uses the direct method, Algorithm 2 uses the subtraction method and Algorithm 3 uses the reciprocity method in the forward problem.

Algorithm 1	Algorithm 2	Algorithm 3
Precompute T	Precompute T	Precompute T and ∇T
Repeat	Repeat	Repeat
compute new \mathbf{B}^{dir}	compute new \mathbf{B}^{sub}	
compute $\mathbf{T}\mathbf{B}^{\text{dir}}$	compute $\mathbf{T}\mathbf{B}^{\text{sub}} + \mathbf{F}_{\text{elec}}^{\infty}$	
compute \mathbf{M}_{opt}	compute \mathbf{M}_{opt}	compute \mathbf{M}_{opt}
compute \mathbf{u}_{elec}	compute \mathbf{u}_{elec}	compute \mathbf{u}_{elec}
Until Convergence	Until Convergence	Until Convergence

Table 4.2: Computational time for one iteration in the inverse algorithm for a spherical head model with 2 468 080 nodes.

	Direct	Subtraction	Reciprocity
$\tau_{\mathbf{b}}$	0.30 s	49.5 s	-
$\tau_{\mathbf{M}_{\text{opt}}}$	6.2×10^{-5} s	6.2×10^{-5} s	6.2×10^{-5} s
$\tau_{\mathbf{u}_{\text{elec}}}$	0.15 s	0.16 s	4×10^{-7} s
τ_{inv}	0.45 s	49.66 s	6.24×10^{-5} s

computational time for assembling \mathbf{b}^{dir} is obtained by evaluating (3.36), where \mathbf{M} is a unit vector. In the subtraction method, the mathematical dipole leads to a dense right hand side vector in equation (3.45) with non-zero entries equal to the number of nodes on interfaces. The computational time for assembling \mathbf{b}^{sub} is obtained by evaluating (3.44). In (4.13) $\tau_{\mathbf{M}_{\text{opt}}}$ is the time for evaluating (4.11). The $\tau_{\mathbf{u}_{\text{elec}}}$ is the time for evaluating (4.4) for the direct and subtraction methods and (4.8) for the reciprocity method. The r is the number of iterations needed to find the optimal solution and it is dependent on the convergence speed of the optimization method.

Tables 4.1 shows the necessary steps for EEG source localization by using the different algorithms for solving the forward problems. Table 4.2 shows the wall clock time for the computations on our machine for a model with $N = 2\,468\,080$ nodes. By comparing the computational time for all three methods presented in Table 4.2, we can see that the reciprocity method solves the inverse problem much faster than the other methods.

4.6 Choosing the Number of Sources

The number of focal sources is unknown in advance and is required as an input parameter for the spatio-temporal dipole modeling. One possible way is to start with one dipole and then increase the number until some criterion on the matching between the measured and optimized potentials at the electrodes is met. One natural criterion is that $\frac{\|\mathbf{u}_{\text{meas}} - \mathbf{L}(\mathbf{x})\mathbf{M}\|^2}{\|\mathbf{u}_{\text{meas}}\|^2}$ is lower than some prescribed value, e.g., 0.01. Mosher et al. [38] proposed a method which quickly scans with a one dipole search, rather than the p-dipole search necessary in a complete fit. They proposed to separate the signal and noise subspaces and thus to visually determine the number of source components, through the drop in magnitude of the smallest signal eigenvalue to the greatest noise eigenvalue of the estimated spatial data covariance matrix. This procedure assumes that the signals have sufficient strength and that they are sufficiently uncorrelated during the time interval. In [39] a *trial and error* strategy was proposed to combine the determination of the unknown number parameter with the localization of the sources using the nonlinear dipole fit method. Knösche et al. [91] presented a systematic way to determine the number of dipoles by information criteria. The information criteria are based on a statistical concept of separating the space spanned by the principal components of the estimated data covariance matrix into a signal and a noise part. In the next chapter, we propose a multi-dipole source localization method based on PSO that can deal with scenarios where the single dipole source localization may fail.

Particle Swarm Optimization

As discussed in previous chapters, EEG is one of the most commonly used biomedical techniques since it provides a way to non-invasively study the function of the human brain. The EEG source localization problem is (usually) highly nonlinear and requires efficient algorithms for its solution. The most widely used optimization methods for solving the EEG inverse problem can be classified into two groups: gradient methods, which use function and derivative information (e.g., Levenberg-Marquardt [103]), and search methods (non-gradient techniques) which use only function values (e.g., Nelder-Mead downhill simplex [104]). In the literature these methods are also called local optimization and global optimization methods, respectively. Both of these methods minimize the cost function by iteratively adjusting the parameters of the dipole sources. The local optimization is fast to converge and effective when there is only one dipole in our source model and the data is noiseless. But when we use the multi-dipole model and have noisy data the local optimization approaches are not always effective since they are often trapped in local minima [105–107].

The dimensionality of the EEG source localization problem can be reduced by factoring out the linear parameters but still a fundamental problem remains: the least squares cost function is highly non-convex with respect to the locations of the dipoles. Consequently, inverse methods such as gradient based methods or nonlinear simplex searches often become trapped in local minima, yielding significant localization errors [108, 109]. The gray matter tissue is located in several disjunct regions in the head which leads to a non-continuous solution space and makes the problem more difficult to solve using standard optimization methods [110]. Moreover, by applying the physiological constraints, such as orthogonality (sources are orthogonal to the gray matter surface) and the sparsity, the problem has a non-differentiable cost function [111–113]. In addition, the final solution often depends on the initial approximation and the number of local minima of the cost function [114] since reasonable initial guesses are difficult to make

Metaheuristic algorithms for global optimization have been used in the solution of the EEG inverse problem [115–120], and most of them reported high

accuracy on the estimation of multiple dipoles with simulation and realistic studies. Nevertheless, a strict statistical study on the variability of these results under realistic conditions has not yet been performed, and the establishment of realistic confidence intervals as a function of the parameter space of the metaheuristic algorithms remains an open task.

Particle swarm optimization is a swarm intelligence algorithm for numerical optimization problems [121, 122]. PSO has gained increasing popularity in recent years and has been applied to a large group of problems in science and engineering [123–131], and also in biomedical applications [120, 132–142].

In the next sections, we first introduce the standard PSO method and some improved versions. Also we present the parameter selection approaches and their limitations. Next, we propose a novel particle swarm optimization method with problem-specific modifications for the epileptic spike source localization and compare its effectiveness and efficiency with other improved version of PSO, a genetic algorithm (GA) and the deterministic global optimization algorithm, DIRECT. Finally, we show the ability of modified PSO (MPSO) to solve multiple source localization. The results show that, whereas the DIRECT method failed to efficiently solve the source localization problem, the MPSO could find the optimal solution significantly faster than other improved versions of PSO, as well as GA. To the best of the author's knowledge, the PSO algorithm has not been applied to real EEG source localization previously.

5.1 Original PSO

The Particle Swarm Optimization concept was first introduced by Kennedy and Eberhart [121, 122] in 1995 based on social system behavior such as the movement of flock of birds or a school of fish when searching for food. Each individual in the swarm is called a particle. The i -th particle of the swarm is represented by the vectors \mathbf{X}_i for its position and \mathbf{V}_i for its velocity. The particle has a memory to record the position of its previous best performance, personal best (*pbest*), in the vector \mathbf{P}_i and the position of the best particle in the swarm, global best (*gbest*), which is recorded in the vector \mathbf{P}_g . The particle swarm optimization algorithm consists of, in each iteration, changing the velocity of each particle towards the position of its best performance, \mathbf{P}_i , and the swarm best position, \mathbf{P}_g . Thus in the original version particles move according to the following formula:

$$\begin{cases} \mathbf{V}_i^{t+1} &= \mathbf{V}_i^t + c_1 \text{Rand}() (\mathbf{P}_i - \mathbf{X}_i^t) \\ &\quad + c_2 \text{Rand}() (\mathbf{P}_g - \mathbf{X}_i^t), \\ \mathbf{X}_i^{t+1} &= \mathbf{X}_i^t + \mathbf{V}_i^{t+1}. \end{cases} \quad (5.1)$$

The parameters c_1 and c_2 are the *cognitive* and *social learning rates*. These two rates control the relative influence of the memory of the swarm's best performance, to the memory of the individual, and are often selected to the same value to give each learning rate equal weight. $Rand()$ is a random number, drawn from a uniform distribution between 0.0 and 1.0. In any situation, we do not know whether the cognitive or social learning term should be stronger; if we weight them both with random numbers, then their strength changes randomly. The effect of this is that the particle moves unevenly around the point defined as the weighted average of the two best positions, \mathbf{P}_i and \mathbf{P}_g . Due to randomness, the exact position of this point changes in every iteration. In addition to the c_1 and c_2 parameters, implementation of the original algorithm also requires placing limits on the search area, \mathbf{X}_{\max} and \mathbf{X}_{\min} , and the velocity, \mathbf{V}_{\max} . Changes in velocity are stochastic, and an undesirable result of this is that the particle's trajectory expands towards infinity. The maximum velocity parameter, \mathbf{V}_{\max} , controls the particle's trajectory to avoid approach infinity [143].

5.2 Improved PSO

Shi and Eberhart [144, 145] devised an inertia weight, w , to improve the accuracy of PSO by damping the velocities over time, allowing the swarm to converge with greater precision. By integration of w into the algorithm, the formula for computing the new velocity is

$$\begin{aligned} \mathbf{V}_i^{t+1} = & w\mathbf{V}_i^t + c_1\text{Rand()}(\mathbf{P}_i - \mathbf{X}_i^t) \\ & + c_2\text{Rand()}(\mathbf{P}_g - \mathbf{X}_i^t). \end{aligned} \quad (5.2)$$

As originally developed, w is often decreased linearly from about 0.9 to 0.4 during a run [143]. A suitable selection of the inertia weight provides a balance between exploration, the ability to test various regions in the problem space in order to locate a good optimum, hopefully the global one, and exploitation, the ability to concentrate the search around a promising candidate solution in order to locate the optimum precisely [145].

The maximum velocity, \mathbf{V}_{\max} , is a constraint that controls the maximum global exploration ability PSO can have. By setting a too small maximum velocity, the maximum global exploration ability is limited and PSO will always favor a local search no matter what the inertia weight is. Since the maximum velocity affects global exploration ability indirectly, whereas the inertia weight affects it directly, it will generally be better to control the global exploration ability through inertia weight only. Choosing a large inertia weight to facilitate more global exploration is not a good strategy, instead a smaller inertia weight should be selected to

achieve a balance between exploration and exploitation and thus a faster convergence [143].

In [146] Clerc proposed a *constraint coefficient*, K , as a modification of PSO and in [147] it was found that K , combined with constraints on \mathbf{V}_{max} , significantly improved the PSO performance. The formula for computing the new velocity with constriction factor K is

$$\begin{aligned} \mathbf{V}_i^{t+1} = & K(\mathbf{V}_i^t + c_1 \text{Rand}()(\mathbf{P}_i - \mathbf{X}_i^t) \\ & + c_2 \text{Rand}()(\mathbf{P}_g - \mathbf{X}_i^t)), \end{aligned} \quad (5.3)$$

where $K = \frac{2}{|2 - \phi - \sqrt{\phi^2 - 4\phi}|}$ and $\phi = c_1 + c_2 > 4$.

5.3 PSO Drawbacks

The PSO algorithm introduced by Kennedy and Eberhart has proven to be powerful but needs to select various parameters, such as the maximum velocity coefficient, the swarm size as well as the cognitive and social learning rates. A complete theoretical analysis of the algorithm has been done by Clerc and Kennedy [148]. Based on this analysis, the authors derived a reasonable set of tuning parameters, as confirmed by [147]. However, the parameter selection in a specific problem is not straightforward.

The PSO algorithm risks trapping in local minima and losing its exploration–exploitation ability. Angeline, [149], for well known test functions, showed that although PSO was capable of finding a reasonable quality solution very fast, it could not improve the quality of the solution as the number of iterations was increased. If the *pbest* and *gbest* of a particle remain very close to each other then the particle becomes inactive in the swarm. In other words, when $|\mathbf{P}_i - \mathbf{X}_i^t|$ and $|\mathbf{P}_g - \mathbf{X}_i^t|$ are both small, and at the same time \mathbf{V}_i^t has a small value, then this particle loses its exploration ability. This could happen in the early stages for the *gbest* particle and as a consequence the PSO is trapped in a local minima. In the following section we propose a Modified PSO (MPSO) which can help to reduce the aforementioned drawbacks.

5.4 The Modified PSO

In this section we describe some modifications that have been made to PSO, i.e., evolutionary programming, concept of authority, adaptive swarm size and problem-specific modification.

5.4.1 Evolutionary Programming

One way to avoid PSO being trapped in local minima is mutation [150, 151] and using evolutionary programming (EP) [149, 152, 153]. In EP, a population of N particles is randomly selected initially. Each particle is taken as a pair of real valued vectors, (\mathbf{X}_i, η_i) , where \mathbf{X}_i is the position vector and η_i is the standard deviation for Gaussian mutations of the i -th particle, respectively. Each parent particle (\mathbf{X}_i, η_i) creates a single offspring $(\hat{\mathbf{X}}_i, \hat{\eta}_i)$ according to the following equations [154]:

$$\begin{cases} \hat{\mathbf{X}}_i = \mathbf{X}_i + \eta_i \mathcal{N}(0, 1) \\ \hat{\eta}_i = \eta_i e^{(\hat{\tau} \mathcal{N}(0, 1) + \tau \mathcal{N}(0, 1))} \end{cases} \quad (5.4)$$

where $\mathcal{N}(0, 1)$ denotes a normally distributed random number with mean zero and standard deviation one. The factors τ and $\hat{\tau}$ are commonly set to $(\sqrt{2\sqrt{n_{\text{dim}}}})^{-1}$ and $(\sqrt{2n_{\text{dim}}})^{-1}$ [154]. By utilizing a q -tournament selection, N particles are selected out of $2N$ parents and offspring. Tournament selection is a popular form of selection which is commonly used in genetic algorithms [155]. In the q -tournament selection [156], q number of individuals is chosen randomly from the population and the best individual from this group is selected. This process is repeated as often as individuals must be chosen. The parameter for tournament selection is the tournament size q . The q takes values ranging from 2 to the number of individuals in the population.

After applying EP to the swarm, once more M particles are selected from the swarm population by the q -tournament selection and thus become the so-called *elite particles* [157]. For each particle, the nearest elite particle is determined by the Euclidean distance. By evaluating the fitness value of all the particles, the global best position is determined. The velocity and the position of the particles are updated according to the global best position, the nearest elite position, and the personal best position. These are applied to the PSO with inertia weight as follows:

$$\begin{aligned} \mathbf{V}_i^{t+1} = & w\mathbf{V}_i^t + c_1 \text{Rand}() (\mathbf{P}_i - \mathbf{X}_i^t) + c_2 \text{Rand}() (\mathbf{P}_g - \mathbf{X}_i^t) \\ & + c_3 \text{Rand}() (\mathbf{P}_e - \mathbf{X}_i^t), \end{aligned} \quad (5.5)$$

where c_3 denotes the constant of the nearest elite and \mathbf{P}_e is the nearest elite position.

5.4.2 The Concept of Authority

To maintain the exploration ability in our modified PSO and increase the exploitation ability, we introduce the concept of *authority* and apply it to the particle's behavior. To implement the concept of authority, the R closest particles to *gbest* are extracted as the swarm moves close to a minimum and they are allowed to fly freely based on their memory and knowledge. Thus, the velocity update is divided into two parts as

$$\begin{aligned} \mathbf{V}_i^{t+1} = & w\mathbf{V}_i^t + c_1\text{Rand}()(\mathbf{P}_i - \mathbf{X}_i^t) + c_2\text{Rand}()(\mathbf{P}_g - \mathbf{X}_i^t) \\ & + c_3\text{Rand}()(\mathbf{P}_e - \mathbf{X}_i^t), \end{aligned} \quad (5.6)$$

where $i = 1, 2, \dots, N - R$ and

$$\mathbf{V}_r^{t+1} = w\mathbf{V}_r^t + c_1\text{Rand}()(\mathbf{P}_r - \mathbf{X}_r^t) \quad (5.7)$$

where $r = N - R + 1, \dots, N$. The R nearest particles to *gbest* are re-selected in each iteration to ensure that the particles that moved away from the *gbest* lose their authority and at the next iteration, update their velocity based on (5.6). It means that in some steps the particles that are closer to the global best can influence the performance and decision of the swarm, more than others. The concept of authority allows the swarm to have more information around *gbest* before lots of particles approach it and get stuck to each other, thus it improves the exploitation ability. The concept of authority mixed with EP helps to keep the balance between exploration and exploitation as well as avoiding getting trapped in local minima.

5.4.3 Adaptive Swarm Size

Usually, the swarm size is constant. Some authors use 20, while some others use 30 [122, 145], but nobody has proved that one given size is really better than another. Thus it seems better to let the algorithm modify the swarm size [158], adaptively based on the current situation. In each iteration, the swarm has information about each particle's position, \mathbf{X}_i , personal best, \mathbf{P}_i , velocity, \mathbf{V}_i , as well as the previous objective function values. The swarm also has some global information, i.e., the swarm size and time step. Using this information, the swarm has two options to act on particles. It may remove particles from the swarm or generate new particles. The condition for the swarm to change the status of a particle is based on the following criteria:

- If one particle has had *enough improvement* a new particle is generated from that particle and the old one is kept.

- If one particle has not had *enough improvement* that particle is removed from the swarm.

Here, the status changes every 5 iterations which is equal to the neighborhood size of the particles. The *enough improvement* is defined by "improvement for 5 iterations". Reflecting walls are used as boundary conditions for the MPSO. When a particle hits the boundary in one of the dimensions, the sign of that velocity component is changed and the particle is reflected back towards the searching space. This boundary condition keeps the particles inside the searching space at all times.

5.4.4 Problem-Specific Modification

As our main goal is to apply PSO to EEG source localization, we add a problem-specific modification to the MPSO. This modification comes from the anatomical constraint in EEG source localization. Restricting the search space to limited areas of the brain volume, e.g., the gray matter, reduces the ambiguity of source localization [159]. In the inverse problem we consider only those dipole locations and orientations that are consistent with the anatomical data. As discussed in Chapter 2, the EEG signals are generated by currents flowing in the apical dendrites of cortical pyramidal cells [56, 160] so the search area could be restricted only to the cortex sheet of the brain. We use this information and add it to the MPSO. For this anatomical constraint MPSO solely evaluates the cost function, (4.12), for the particles that are placed in the gray matter and assigns a high penalty value to others. The MPSO starts from gray matter and in this way it ends up in the gray matter, this constraint also helps to avoid trapping the solution of the inverse problem in false local minima in other tissues.

5.5 Comparison of Different Algorithms

The objective of this section is to statistically compare the performance of the MPSO with some other improved versions of PSO as well as a genetic algorithm [161], for EEG source localization. The well known t-test (hypothesis testing) [162, 163] is used to assess and compare the *effectiveness* and *efficiency* of all the different algorithms. In hypothesis testing, a null hypothesis, H_o will be correctly accepted with a significance (or confidence) level $(1 - \alpha)$ and falsely rejected with a type *I* error (asserting something that is absent) probability α . If the null hypothesis is false, it will be correctly rejected with a power of the test $(1 - \beta)$ and will be falsely accepted with a type *II* error (failing to assert what is present) probability β [164]. The decision options are summarized in Table 5.1. H_a corresponds to an alternative hypothesis that is complimentary to H_o .

Table 5.1: Possible decision outcomes in hypothesis testing (adapted from [164]).

Action	The true situation may be	
	H_o is true	H_o is false
accept H_o , reject H_a	$(1 - \alpha)$ significance level	β [type <i>II</i> error]
reject H_o , accept H_a	α [type <i>I</i> error]	$(1 - \beta)$ power of test
Sum	1	1

The t-test deals with the estimation of a true value from a sample and the establishing of confidence ranges within which the true value can be said to lie with a certain probability $(1 - \alpha)$. In hypothesis testing, increasing the sample size, n , decreases type *I* and *II* error probabilities, α and β , based on the t-distribution. When n is very large, the t-distribution approaches the normal distribution [165].

In this section, two hypotheses are tested. The first test is related to the *effectiveness* (finding the true global optimum) of the algorithms and the second is related to the *efficiency* (computational cost) of the algorithms. Effectiveness is defined as the ability of the algorithm to repeatedly find the known global solution, or arrive at sufficiently close solutions, when the algorithm is started from many random points in the design space. In other words, effectiveness is defined as the probability of finding a high quality solution such that,

$$Q = \left(1 - \frac{\| \mathbf{u}_{\text{meas}} - \mathbf{u}_{\text{est}} \|}{\| \mathbf{u}_{\text{meas}} \|} \right) \%, \quad (5.8)$$

where \mathbf{u}_{meas} and \mathbf{u}_{est} are the measured and estimated EEG signals, respectively. The solution quality metric described in (5.8) could then be used to synthesize a meaningful hypothesis to test the effectiveness of the search algorithms shown in Table 5.2. In our test cases, \mathbf{u}_{meas} is calculated synthetically by solving the forward problem for a dipole located inside the gray matter.

The second hypothesis that is tested in this section is the computational efficiency test. This test directly compares the computational effort required by MPSO and some other methods for EEG source localization. This requires a t-test called *comparison of two means* [163, 166]. For the computational efficiency test, the metric that is implemented is the number of function evaluations, N_{eval} , the algorithm carried out until the convergence criterion was met. The efficiency test is summarized in Table 5.3

5.5.1 Results and Discussions

The two tests were carried out for MPSO, three improved versions of PSO [146, 167] as well as GA [161]. Table 5.4 summarizes the features of the improved

Table 5.2: The effectiveness test.

<p>Objective to test whether $H_a: \mu_Q > 99\%$ $H_0: \mu_Q \leq 99\%$ $t = \frac{\bar{Q} - 99\%}{s(\bar{Q})}$ taking $\alpha = 1\%$, $\beta = 1\%$, and $n = 1000$ where μ is the unknown population mean, \bar{Q} is the mean of the quality of a solution, and</p> $s(\bar{Q}) = \frac{\text{standard deviation of Q}}{\sqrt{n}}$ <p>This is a one sided test of significance of a mean $\rightarrow t_{critical} = 2.0$.</p>
--

Table 5.3: The efficiency test.

<p>Objective to test whether $H_a: \text{MPSO } \mu_{N_{eval}} < \text{OM } \mu_{N_{eval}}$ $H_0: \text{MPSO } \mu_{N_{eval}} \geq \text{OM } \mu_{N_{eval}}$ $t = \frac{\text{OM } \bar{\mu}_{N_{eval}} - \text{MPSO } \bar{\mu}_{N_{eval}}}{\bar{s}(x) \sqrt{(1/n_{\text{OM}} + 1/n_{\text{MPSO}})}}$ where $\bar{s}(x) = \sqrt{\frac{(n_{\text{OM}} - 1)s_{\text{OM}}^2 + (n_{\text{MPSO}} - 1)s_{\text{MPSO}}^2}{n_{\text{OM}} + n_{\text{MPSO}} - 2}}$ OM stands for "Other Method". Taking $\alpha = 1\%$, $\beta = 1\%$, and $n_{\text{OM}} = n_{\text{MPSO}} = 1000$. This is a one sided test of significance of a mean $\rightarrow t_{critical} = 2.5$.</p>
--

versions of PSO selected for benchmarking. We set up four different cases with physiological meaning. The spike dipoles are placed inside the gray matter with the following positions and orientations, see Fig. 5.1:

1. Right motor cortex, radial direction.
2. Right temporal lobe, radial direction.
3. Right temporal lobe, tangential direction.
4. Deep inside the brain, oblique direction.

The background dipole is fixed at the occipital lobe for all cases. Both tests were conducted using acceptable Type I and Type II errors of 1% each. Table 5.5 shows the calculated t-values obtained for the effectiveness test for all methods.

The effectiveness tests for MPSO and the other improved versions of PSO show that $t > t_{critical}$ in all cases. This leads to the rejection of the null hypothesis

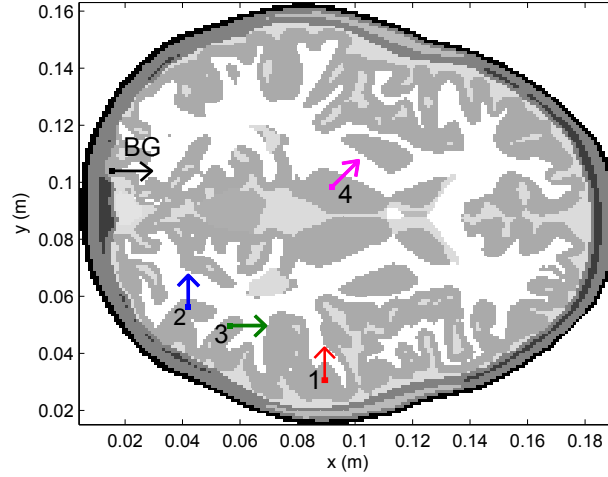


Figure 5.1: Position and orientation of the spike and background sources in 2D. Spike dipole is placed at right motor cortex with radial direction (case 1), right temporal lobe with radial direction (case 2), right temporal lobe with tangential direction (case 3) and deep inside brain with oblique direction (case 4). For all cases the background dipole is placed at the occipital lobe.

Table 5.4: Parameters of different versions of PSO selected here as benchmark methods.

	Formula	w	K	c_1	c_2	c_3
MPSO	Eqs. (5.6) and (5.7)	linear from 0.9 to 0.4	–	0.8	0.4	0.8
PSO1	Inertia (5.2)	linear from 0.9 to 0.4	–	2.0	2.0	–
PSO2	Inertia (5.2)	0.600	–	1.70	1.70	–
PSO3	Inertia (5.2)	0.729	–	1.494	1.494	–
PSO4	Constrict (5.3)	–	0.642	2.10	2.10	–
EPSO	Evolutionary(5.5)	linear from 0.9 to 0.4	–	0.8	0.4	0.8

and the acceptance of the alternative hypothesis, that is the quality of the solutions of these approaches is equal to or greater than 99% in all four cases. This alternative hypothesis is accepted with a confidence level of 99%. The infinity t-values in the Table 5.5 are obtained because in each of the runs the corresponding method consistently found the known solution. Therefore, the quality of the 1000 solutions in each case is 100%.

In all cases the null hypothesis is accepted for the GA runs, therefore it shows that the GA does not converge. By further investigating the data, it is found that the mean quality of the GA solutions for test case 1 is 98.98% with a standard deviation 0.20% and for the other cases it is 94.68% with a standard deviation 0.6%.

Table 5.5: Calculated t-values for the effectiveness hypothesis test.

Effectiveness test, $t_{critical} = 2.0$							
Calculated t-value							
	MPSO	PSO1	PSO2	PSO3	PSO4	EPSO	GA
Case 1	∞	9.07	11.81	7.36	∞	∞	-0.07
Case 2	∞	4.38	6.35	3.68	∞	∞	-7.32
Case 3	∞	6.35	2.43	4.38	∞	∞	-7.29
Case 4	∞	∞	∞	∞	∞	∞	-7.28

Table 5.6: Calculated t-values for the efficiency hypothesis test.

Efficiency test, $t_{critical} = 2.5$						
Calculated t-value						
	EPSO	PSO1	PSO2	PSO3	PSO4	GA
Case 1	15.13	27.16	32.84	33.92	27.18	303.19
Case 2	15.36	24.83	31.23	32.84	23.84	304.28
Case 3	16.72	24.36	28.12	31.24	24.81	305.49
Case 4	15.15	28.96	33.65	34.73	27.45	306.87

In Table 5.6 the results of the efficiency test are given and they show that $t > t_{critical}$ for all cases. These results lead to rejection of the null hypothesis and the acceptance of the alternative hypothesis with a confidence level of 99%. The interpretation of these results is that for all cases the computational effort required by MPSO to converge to a solution, is less than that of the other improved version of PSO as well as GA. Since DIRECT does not have any random parameters the same result is obtained for all runs and the t-test could not be applied. Table 5.7 shows the mean and standard deviation of the number of function evaluations for all methods. From Table 5.7 we can see that the MPSO, in average, finds the optimal solution five times faster than DIRECT. Paper I presents more details on the comparison of MPSO with other methods. In summary, by several examples, we have shown that the MPSO could find the optimal solution significantly faster than the other improved version of PSO as well as a genetic algorithm and the deterministic global optimization, DIRECT. Moreover that the MPSO is less prone to be trapped in local minima.

Table 5.7: Mean and standard deviation for the number of function evaluations for 1000 runs. Since DIRECT does not have any random parameters the same result was obtained for all runs.

	Case 1	Case 2	Case 3	Case 4
MPSO (mean±std)	97±40	93±42	92±39	104±35
EPSO(mean±std)	146±62	158±86	160±81	178±102
SPSO(mean±std)	187±58	201±93	196±86	195±61
CPSO(mean±std)	190±67	209±95	205±94	191±64
GA (mean±std)	1560±450	1680±400	1660±420	1710±550
DIRECT	500	680	430	350

5.6 Multiple Source Localization

Theoretically, it would be possible to calculate the objective function for all combinations of p sources in N_{gray} possible locations in the gray matter, i.e.,

$$\binom{N_{\text{gray}}}{p} = \frac{N_{\text{gray}}!}{(N_{\text{gray}} - p)!p!}, \quad (5.9)$$

evaluations. In practice, this is generally not feasible as the number of gray matter points in the configuration space is too large and cannot be explored exhaustively. The PSO is flexible and straightforward to extend to multiple source localizations. For p source locations, $6p$ unknown parameters should be estimated in 3D, i.e., $3p$ dipole position parameters in Cartesian space (x, y, z) and $3p$ dipole moments (M_x, M_y, M_z) . Thus the i -th particle of the swarm can be represented by the vector $\mathbf{X}_i \in \mathbb{R}^{np}$ and $\mathbf{V}_i \in \mathbb{R}^{np}$, where $n = 1, 2, 3$ is the problem dimension. For $n = 3$ we get,

$$\begin{cases} \mathbf{X}_i = ((x_1, y_1, z_1), \dots, (x_p, y_p, z_p), (M_{x_1}, M_{y_1}, M_{z_1}), \dots, (M_{x_p}, M_{y_p}, M_{z_p}))_i, \\ \mathbf{V}_i = ((V_{x_1}, V_{y_1}, V_{z_1}), \dots, (V_{x_p}, V_{y_p}, V_{z_p}), (V_{M_{x_1}}, V_{M_{y_1}}, V_{M_{z_1}}), \dots, (V_{M_{x_p}}, V_{M_{y_p}}, V_{M_{z_p}}))_i. \end{cases} \quad (5.10)$$

With this configuration for the particles we can now again use (5.6) and (5.7) to minimize the cost function. The minimization problem (4.10) then becomes,

$$J = \min_{\substack{\mathbf{x} \in \Omega_{\text{brain}} \\ \mathbf{M} \in \mathbb{R}^d}} \left\| \mathbf{u}_{\text{meas}} - \sum_{i=1}^p \mathbf{L}(\mathbf{x}_i) \mathbf{M}_i \right\|^2, \quad (5.11)$$

To test the ability of the MPSO to localize multiple dipole sources, we generate sets of simulated potentials for 30 channel electrodes for two active spike sources

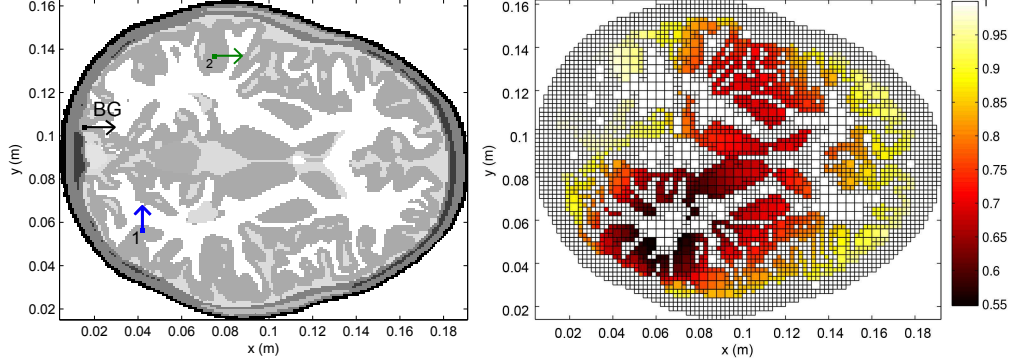


Figure 5.2: Left) Position and orientation of the two active spikes, with the same amplitude equal to $10 \mu\text{Am}$ and background sources, $1 \mu\text{Am}$, in 2D setup, Right) The cost function when a single dipole source is used.

placed in both brain hemispheres in a 2D case, see Fig. 5.2. As in the previous test cases, the background dipole is fixed at the occipital lobe for all cases. The two spike sources have the same amplitude equal to $10 \mu\text{Am}$, one with radial direction and the other with tangential direction. Fig. 5.2 shows the cost function when only a single dipole is used to estimate the potential for this test case. As we can see in Fig. 5.2 the global minimum is located 10.3 mm from the source in the left hemisphere and 88.4 mm from the source in the right hemisphere. The relative error is equal to 0.52 and clearly a single dipole is not enough in this case.

Therefore, we run the case with the multiple MSPO source localization formulated in (5.10) and (5.11) with eight unknown parameters, two position parameters and two orientation parameters for each dipole. To reduce the unknown parameters we can use the method explained in Section 4.4 and reduce the unknown parameters to six. For given dipole positions $\mathbf{x}_1 \in \Omega_{\text{brain}}$, $\mathbf{x}_2 \in \Omega_{\text{brain}}$ and orientation $\mathbf{M}_1 \in \mathbb{R}^3$ the optimal components $\mathbf{M}_{2,\text{opt}}$ are found in least squares sense as the solution of the linear equations $\mathbf{u}_{\text{meas}} - \mathbf{L}(\mathbf{x}_1)\mathbf{M}_1 = \mathbf{L}(\mathbf{x}_2)\mathbf{M}_2$, i.e.,

$$\mathbf{M}_{2,\text{opt}}(\mathbf{x}) = (\mathbf{L}^T(\mathbf{x}_2)\mathbf{L}(\mathbf{x}_2))^{-1}\mathbf{L}^T(\mathbf{x}_2)\tilde{\mathbf{u}}_{\text{meas}}. \quad (5.12)$$

where $\tilde{\mathbf{u}}_{\text{meas}} = \mathbf{u}_{\text{meas}} - \mathbf{L}(\mathbf{x}_1)\mathbf{M}_1$.

We ran the multiple MPSO 100 times. The MPSO had 30 initial particles and the optimization was stopped if the relative error ≤ 0.08 (this value was obtained when the exact dipole positions and orientations were selected as input for the optimization problem). Table 5.8 summarizes the results for multiple MPSO source localization. The standard deviation is zero since the MPSO found the optimal point in all runs. The errors presented in Table 5.8 is due to the background

source activity.

Table 5.8: Mean of the localization, orientation and relative errors after 100 runs.

	Source 1	Source 2
Localization error (mm)	1.8	4.0
Orientation Error (deg)	0.0	1.73
Relative Error	0.08	

The results in Table 5.8 show a significant source localization improvement compared to the one dipole localization approach. In our case the head model had 2 879 gray matter points. Thus all possible unique combinations of the two sources are 4 142 881. The multiple MPSO found the optimal only after 750 evaluations, which is 0.018% of the total number of possible choices. Using multiple MPSO source localization is a reliable choice when we deal with a strong multi-active sources scenario, since a one dipole source localization may fail in that case.

Head Model

EEG source localization results are influenced by different errors and approximations, such as head-model complexity [10, 47], EEG signal noise [48], tissue conductivity noise [11] and electrode misplacement [48, 49]. In this chapter we investigate some of these errors and approximations.

Segmentation of head tissues using structural imaging techniques such as computed tomography (CT) and MRI is the first step towards generating a patient-specific head model. MRI is known as a safe and non-invasive method for imaging the human head. Because of its high contrast, T1-weighted MRI (T1-MRI) is well suited for the segmentation of soft tissues, i.e., white and gray matter and tissue boundaries like outer skull and skin. In contrast, the classification of hard tissues, such as the skull, is problematic. Several estimation approaches for classification of the inner skull layer have been presented [85, 168–170]. Accurate EEG source localization of, in particular, basal frontal and mesial temporal current sources in the human brain, are of high importance in epilepsy surgery. In [171] it was shown that inaccurate modelling of the skull compartment can cause 1 cm localization error and this may be detrimental in clinical applications. CT is well suited for imaging bone tissues such as the human skull, and registration of a CT with a T1-MRI [172] enables exact modeling of the skull, but also a radiation exposure risk which is avoided when possible. Another well suited modality for extracting the bone from soft tissue is Proton Density MRI (PD-MRI) since the difference between the quantity of water protons of bone tissues and intracranial tissues is large.

Furthermore, the head model complexity studies in [10, 11] have shown that CSF has significant influence on the EEG source localization error. As normal CSF has long T1 and T2 times, which manifest as dark signals on T1-weighted images and bright signals on T2-weighted images, it is difficult to segment the CSF accurately. Moreover, the brain extraction step during segmentation can affect the CSF misclassification significantly since a large amount of the CSF is located between the brain and skull compartments [47]. In the following section, the MRI acquisition and segmentation methods used in our real EEG test case are

presented.

6.1 MR Acquisition

Structural MR images were acquired using a PHILIPS ACHIEVA 3T scanner (Sahlgrenska University Hospital, Gothenburg, Sweden) equipped with a 32 channel head coil. T1-weighted images were acquired for a healthy subject, (195 sagittal slices, matrix size = 256×256 , voxel size = 0.9375 mm^3 , flip angle 8 deg, TR/TE= 8.095/3.704 ms).

To allow for an estimation of the conductivity anisotropy in white matter (WM) based on diffusion tensor imaging (DTI) data [17], diffusion weighted images were acquired using a twice refocused SE-EPI sequence (60 axial slices, matrix size = 128×128 , voxel size $1.75 \times 1.75 \times 2.0 \text{ mm}^3$, TR/TE = 9793.685/77.183 ms, two averages) with 32 diffusion directions and a b-value of 800 s/mm^2 .

6.2 MRI Segmentation Methods

In the last two decades, many research groups have developed methods for brain MRI data sequence analysis, for reconstruction of the brain's cortical surface from anatomical MR data and registration of functional MR data on the reconstructed cortical surface [173–182]. Among them, the most widely used are the FMRIB Software Library (FSL) [173] and FreeSurfer [175]. In Paper III, we have investigated the influence of image segmentation done by FSL and FreeSurfer on the source localization. Comparing the results from the two methods with the “ground truth”, the set of voxels that were labeled by an expert, showed that the segmentations obtained from FSL gave better accuracy than those from FreeSurfer. In the following section we present the segmentation methods used to investigate the influence of head model on the EEG source localization. In our real EEG test case, presented in the next chapter, a manual segmentation done by an expert is used for generating the head model. More details are given in Papers II and III.

6.2.1 FSL

The segmentation of the five tissues, GM, WM, CSF, scalp and skull, is done by FSL in two steps. In the first step, masks of skin, skull and brain are generated by using a preset intensity threshold value (ITV) in the BET module. In the second step, an automated segmentation of three tissues, GM, WM and CSF, is carried out by applying the FAST module [174]. For the BET step, ITV is selected equal to 0.3 since in [47] it is shown that this value generated a model with minimum

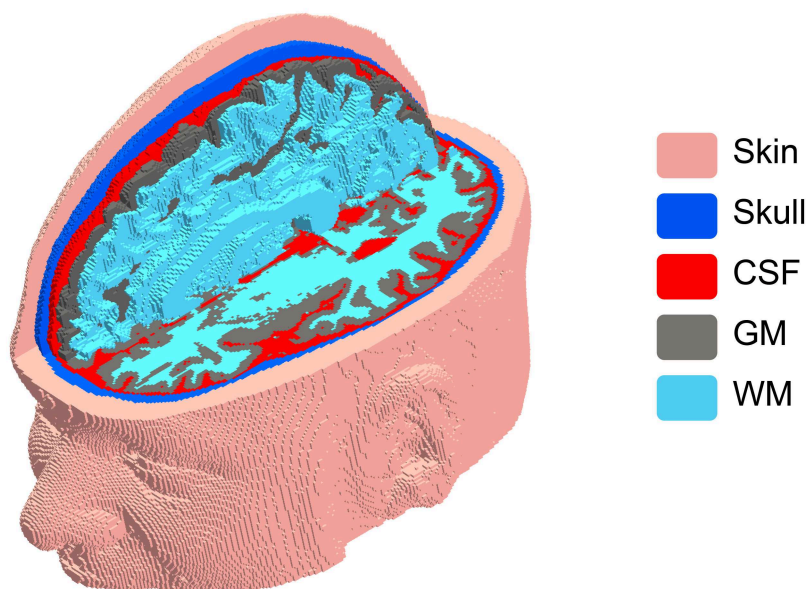


Figure 6.1: The subject's head model generated from the FSL segmented results.

source localization error. To generate an accurate head model the segmented tissues obtained from FSL need to be checked and corrected manually by a clinical expert. Fig. 6.1 illustrates the subject's FEM head model obtained from the corrected FSL segmentation.

6.2.2 Mean Shift Method

Our group (Department of Signals and Systems, Chalmers University of Technology, Gothenburg, Sweden) recently proposed a fully automatic multi-tissue segmentation method for multi-modal MRI images of the head [183]. The method is based on a hierarchical segmentation approach (HSA) incorporating Bayesian-based adaptive mean-shift segmentation (BAMS).

In Paper VIII, this method has been tested for synthetic and real EEG source localization and compared with other existing methods such as, HSA-HMRF-EM [184] and BET-FAST [174]. Table 6.1 summarizes these results for the median nerve stimulation (see Paper VIII for more results).

6.2.3 Manual Segmentation

Here the segmentation of the five tissues, i.e., GM, WM, CSF, scalp and skull, was done manually by a clinical expert based on neurophysiological knowledge. Our expert spent 170 hours to fully segment the head model (120 slices). We call this segmented model the “ground truth” since it was the most accurate segmentation model that we could generate for EEG source localization. We made a comparison between the different segmentation methods mentioned in the previous sections for source localization of somatosensory evoked potentials, see Table 6.1.

Table 6.1: The relative error defined as relative difference between measured SEPs and estimated potentials for the median nerve SEPs source localization for head models generated by different segmentation methods.

Segmentation methods	Relative error
FSL	0.42
Mean Shift Method	0.35
FSL Manually Corrected	0.32
Manual Segmentation	0.23

As we can see from Table 6.1 the manually segmented head model gave, as expected, best results compared to the other segmentation methods. We use this model in the next chapter for real EEG source localization.

6.3 Modeling Tissue Conductivity Anisotropy

This section describes the modeling of realistic WM conductivity anisotropy, for the generation of realistic anisotropic high-resolution volume conductor models of the head. Conductivity anisotropy, directionally dependent, with a ratio of about 1 to 9 (normal to parallel to fibers) has been measured for brain WM by Nicholson [15], however, a robust and non-invasive direct measurement seems to be challenging. Nevertheless, a formalism has been described recently for relating the effective electrical conductivity tensor to the effective water diffusion tensor in brain WM [17, 18, 185]. Water diffusion can be measured non-invasively by DT-MRI. The mutual restriction of both the ionic and the water mobility by the geometry of the porous medium (the WM fibers) builds the basis for the described relationship. Basser et al. [16] introduced the assumption that the conductivity tensor shares the eigenvectors with the water diffusion tensor. The assumption is not that a fundamental relation exists between the free mobility of ionic and water particles, rather that the restricted mobilities are related through the geometry.

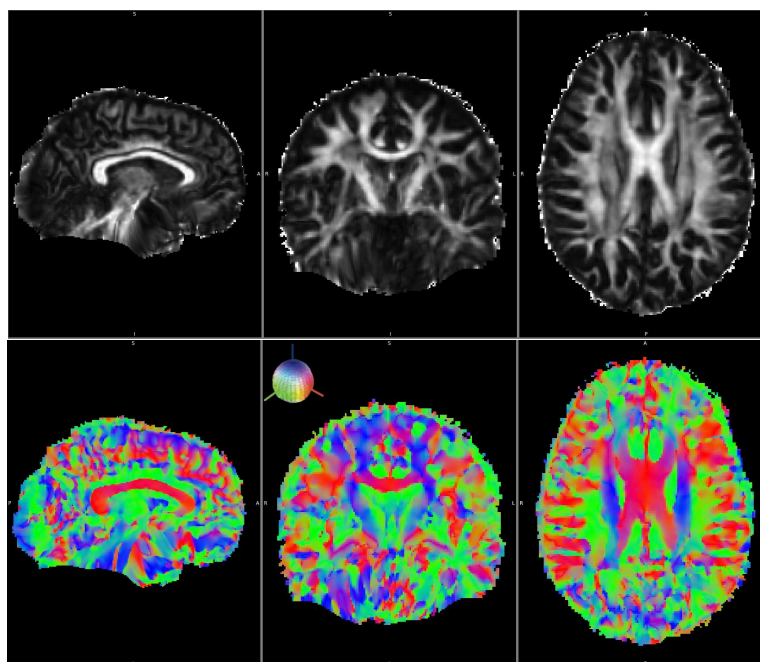


Figure 6.2: The fractional anisotropy image after registration of the T1 anatomy (top row), the color coded first eigenvector of the DTI tensor co-registered with the T1-weighted MRI (bottom row).

Two approaches are proposed in the literature for extracting the tissue anisotropy from DT-MRI, namely a “direct mapping” [186, 187] and a “volume normalized mapping” [188]. The direct mapping simply scales the DTI tensors to get the conductivity distribution. The volume normalized mapping uses the anisotropy information of the DTI data, while maintaining the mean conductivity of the tensors at a predefined value, e.g., the WM or GM isotropic conductivity. This approach prevents the problem of very high peak conductivity values that can occur when the direct mapping is used.

The procedure to prepare the diffusion weighted images for the subsequent estimation of the conductivity tensors, is based on the processing steps implemented in FDT [173]. A brain mask is extracted from the first b-value equal to zero image and the remaining images are corrected for head movements and distortions caused by eddy-currents using a linear affine co-registration to this first $b = 0$ image. After fitting the diffusion tensors and determining the fractional anisotropy (FA), the FA image is co-registered to the structural T1-weighted image. A two-step procedure is used to account for local distortions in the diffusion weighted images, starting with an affine registration and then applying a nonlinear registration. The resulting warp field is applied to the DTI data, thereby ensuring

that the correct diffusion directions are preserved. Fig. 6.2 shows the FA and color coded first eigenvector of the DTI tensor co-registered with the T1-weighted MRI, which illustrates the fiber orientation map from a DT-MRI. Finally, the conversion schemes from the diffusion to conductivity tensors are applied. In the next section we present two variations of these conversion schemes. Moreover, in Paper IX we add the WM anisotropy to the head model in a real EEG test case.

6.3.1 Direct Mapping

Tuch et al. in [187] showed a linear relationship between the eigenvalues of the diffusion and conductivity tensors

$$\sigma_v = s d_v, \quad (6.1)$$

where σ_v and d_v represent the v th conductivity and diffusion eigenvalue, respectively, and s is a scaling factor. With this assumption, the anisotropy ratio between the different diffusion eigenvalues are preserved. Tuch et al. [187] in the original scaling factor reported that results often have unrealistically high conductivity values, and an adjusted scaling factor was applied to make sure that the conductivity stays in a reasonable range [186]. The factor s was selected such that the geometric mean of the conductivity eigenvalues, averaged across voxels, fitted that of the isotropic conductivities reported in the literature. Thereby, a single factor s was chosen for GM and WM such that the mean conductivities derived from DTI for both tissue types matched the isotropic reference values as good as possible in a least-squares sense,

$$s = \frac{\bar{d}_{WM} \sigma_{WM}^{iso} + \bar{d}_{GM} \sigma_{GM}^{iso}}{\bar{d}_{WM}^2 + \bar{d}_{GM}^2}, \quad (6.2)$$

where σ_{WM}^{iso} and σ_{GM}^{iso} denote the isotropic conductivities of WM and GM, respectively. Typical conductivities $\sigma_{WM}^{iso} = 0.142$ S/m and $\sigma_{GM}^{iso} = 0.33$ S/m were used as isotropic reference values for EEG source localization [10, 186, 189]. The average value of the diffusion eigenvalues d_1 , d_2 and d_3 , in all voxels, is given by

$$\bar{d}_{WM/GM} = \sqrt[3]{\frac{\sum_{k=1}^{N_{WM/GM}} (d_1 d_2 d_3)_k}{N_{WM/GM}}}, \quad (6.3)$$

where $N_{WM/GM}$ indicates the number of voxels corresponding to WM and GM, respectively.

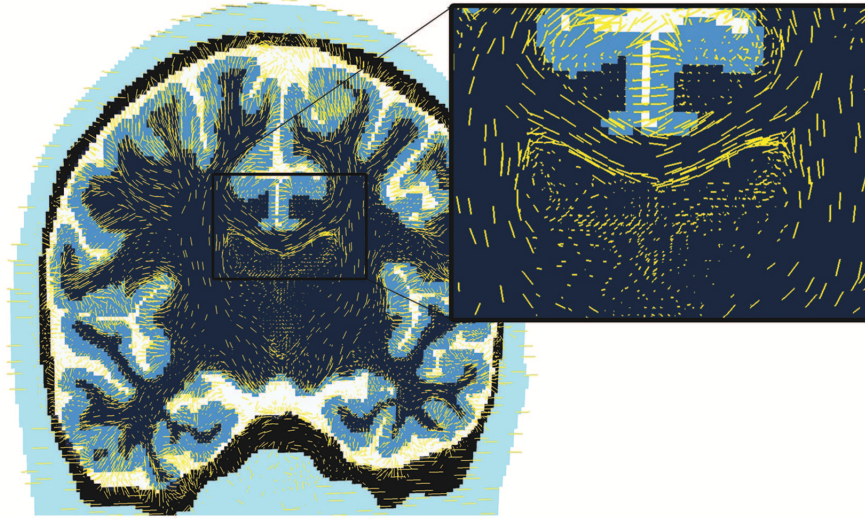


Figure 6.3: The maximum eigenvector co-registered to the segmented T1-weighted image. The zoom-in window shows the corpus callosum area which has highly anisotropic structures.

6.3.2 Volume Normalized Mapping

An alternative for conductivity mapping from DTI is to locally match the geometric mean of the conductivity eigenvalues of each single voxel to that of an isotropic reference value [188]. This approach is referred to as a “volume normalized” approach, with the adjusted conductivity eigenvalues being determined by

$$\sigma_i = \frac{d_i}{\sqrt[3]{d_1 d_2 d_3}} \sigma_{\text{WM/GM}}^{\text{iso}}. \quad (6.4)$$

6.4 Numerical Results

Both the direct and the volume normalized mapping were tested for synthetic EEG source localization with a realistic head model to investigate the influences of anisotropic WM on EEG source localization. Fig. 6.3 illustrates the maximum eigenvector co-registered to the segmented T1-weighted image. The zoom-in window in Fig. 6.3 shows the corpus callosum area. The corpus callosum is the major white-matter tract that crosses the interhemispheric fissure in the human brain and it consists of approximately 200 million interhemispheric fibers, most of which

Table 6.2: Mean and standard deviation of the localization and relative error for 725 source positions with three polarities. The direct and the volume normalized (VN) mapping were used to calculate the WM anisotropic conductivities from diffusion tensor images.

	Direct Mapping			VN Mapping		
	x-polarity	y-polarity	z-polarity	x-polarity	y-polarity	z-polarity
LE (mm)	5.2±3.1	6.1±3.5	6.5±4.2	4.1±2.2	5.2±2.8	5.7±3.4
RE	0.22±0.03	0.26±0.04	0.20±0.03	0.19±0.04	0.22±0.04	0.17±0.05

connect homologous regions of the cerebral cortex [190]. The corpus callosum with highly anisotropic cellular structures is a good reference to check the co-registration results visually.

To investigate the influence of WM anisotropy on source localization, a patch of gray matter with 725 voxels was selected. First, the EEG signals for a model with anisotropic tissues were calculated synthetically by applying the reciprocity method. Then the exhaustive search algorithm was used to locate the sources for a model with isotropic tissues. At each point, dipoles with three polarities, i.e., x-, y- and z-polarity were tested. The relative errors (RE) are calculated by comparing the isotropic and anisotropic solutions at each electrode node as follows

$$RE = \frac{\|\mathbf{u}_{\text{elec}}^{\text{aniso}} - \mathbf{u}_{\text{elec}}^{\text{iso}}\|}{\|\mathbf{u}_{\text{elec}}^{\text{aniso}}\|}, \quad (6.5)$$

where $\mathbf{u}_{\text{elec}}^{\text{iso}}$ and $\mathbf{u}_{\text{elec}}^{\text{aniso}}$ are potential values at electrodes for isotropic and anisotropic models, respectively, and $\|\cdot\|$ denotes the Euclidean norm. Moreover, for a single point source, the localization error (LE) is the distance between the estimated and the actual source position, defined as

$$LE = \|\mathbf{x}_0^{\text{aniso}} - \mathbf{x}_0^{\text{iso}}\|, \quad (6.6)$$

where $\mathbf{x}_0^{\text{aniso}}$ is the actual source position in the anisotropic head model and $\mathbf{x}_0^{\text{iso}}$ is the estimated source position in the isotropic head model.

Table 6.2 presents the mean and standard deviation (STD) of the LE and RE for both direct and volume normalized mapping. As we can see the WM anisotropy affects the localization approximately 5 mm with a 20% relative error. From this observation, we can conclude that using a head model with WM anisotropic tissue might affect the source localization in the range of millimeters. These results are consistent with the previous study [188]. In [188], it is concluded that the single-source localization errors resulting from neglecting anisotropy were found to be smaller compared to other modeling errors, like mis-

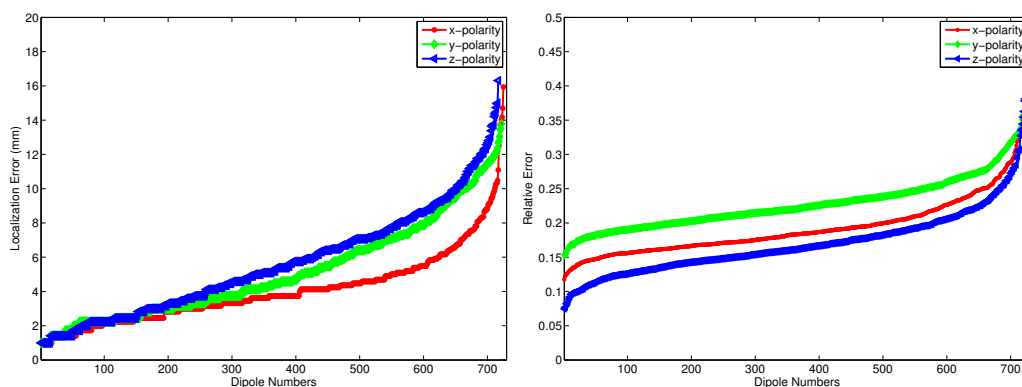


Figure 6.4: The localization error (left) and the relative error (right) for the different dipole sources using the volume normalized mapping.

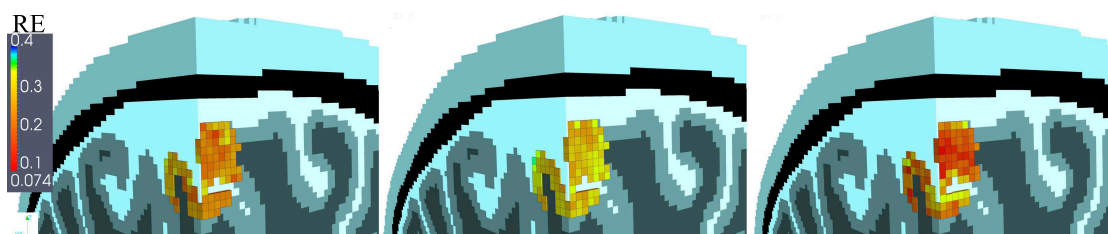


Figure 6.5: The color coded relative error projected on the gray matter for dipoles with x-polarity (left), y-polarity (middle) and z-polarity (right) obtained using the volume normalized mapping.

classified tissue or the use of non-realistic head models.

Fig. 6.4 shows the localization and relative error results for all three polarities. As we can see in Fig. 6.4 the x-polarity dipoles have smaller localization error compared to other polarities. Fig. 6.5 shows the relative error projected on the gray matter voxels. This figure indicates that the source positions surrounded by gray matter voxels, have smaller relative compared to those which are closer to or on the boundary.

Real EEG Test Case

The real EEG data that we use in this thesis was recorded from stimulation of somatosensory evoked potentials (SEPs) on a healthy subject. The 61 EEG electrodes were placed on the subject's head according to the 10/10 EEG electrode system [191]. The 3D (-x,-y,-z) coordinates of these electrodes were measured before and after the SEP stimulation experiment with a digitizer, and for the electrode registration three reference points, i.e., nasion (the delve at the top of the nose, level with the eyes), left and right tragus (the point situated in front of the respective concha) were measured on the subjects head. In this study two sets of stimulations were measured: *a*) median nerve at the left hand and *b*) the left posterior tibial nerves at the subject's ankle. In the following sections the SEP details, validation methods and results are presented.

7.1 Somatosensory Evoked Potential

Evoked potentials are the electrical signals generated by the nervous system in response to sensory stimulus. Auditory, visual, and somatosensory stimuli are commonly used for clinically evoked potential studies. Somatosensory evoked potentials (SEP) consist of a series of waves that reflect sequential activation of neural structures along the somatosensory pathways. Sensory nerves (cell bodies in the dorsal root ganglia) transmit the signal rostrally and ipsilaterally (first order fibers), in the posterior column to a synapse in the dorsal column nuclei at the cervicomedullary junction [192]. Then the signal is passed via the second order fibers that cross to the contralateral thalamus via the medial lemniscus. Finally, the signal travels via the third order fibers from the thalamus to the frontoparietal sensory cortex. Fig. 7.1 shows the SEP pathway (adopted from Saladin [192]). While SEP can be elicited by mechanical stimulation, clinical studies use electrical stimulation of peripheral nerves, which gives larger and more robust responses. The stimulation sites typically used for clinical diagnostic SEP studies are the median nerve at the wrist, the common peroneal nerve at the knee, and/or the posterior

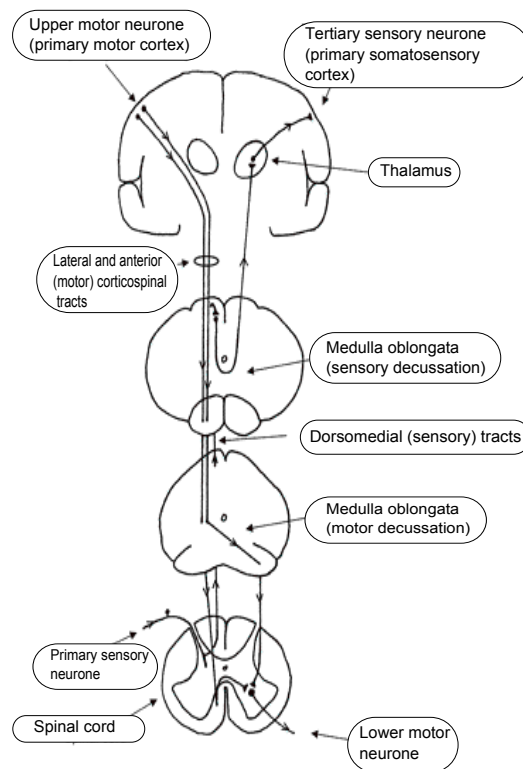


Figure 7.1: The motor and somatosensory pathways: sensory nerves transmit the signal to the sensory cortex via first, second and third order fibers (adopted from Saladin [192]).

tibial nerve at the ankle. In this study two sets of stimulations were measured: *a*) median nerve at the left hand. The anode was placed just proximal to the palmar crease, and the cathode was placed between the tendons of the palmaris longus muscle, 3 cm proximal to the anode. The selected nerves were stimulated with monophasic square pulses, 300 microseconds in duration, and the stimuli were delivered by using a constant current stimulator with 4.8 mA. *b*) the left posterior tibial nerves at the subject's ankle. The selected nerves were stimulated with monophasic square pulses, 300 microseconds in duration and the stimuli was delivered by using a constant current stimulator with 5.2 mA.

Too rapid stimulus delivery rates should be avoided, as they degrade the SEP waveforms. Hence, we used one stimuli per second in our measurements. One should note that the rates, which are subharmonics of the line frequency, such as 5 or 6 Hz, should be avoided, since that contaminates the averaged SEPs by artifacts of the line frequency [193]. Several characteristics of SEP can be measured, including peak latencies, component amplitudes, and waveform morphology. Peak latencies are consistent across subjects, whereas amplitudes show large intersub-

ject variability. Therefore, interpretation of extraoperative diagnostic SEP studies is predominantly based on peak latencies and measures derived from them, such as interpeak intervals and right-left differences [193]. Component amplitudes are more consistent during repeated SEP recordings in the same subject. Therefore, both peak latencies and component amplitudes should be measured and followed during intraoperative monitoring. Ageing is associated with some prolongation of SEP latencies. SEP components are commonly named by their polarity and typical peak latency in the normal population [194]. For example, N20 is a negativity that typically peaks 20 milliseconds after the stimulus. The N20 predominantly reflects activity of neurons in the hand area of the primary somatosensory cortex and the P40 predominantly reflects activity of neurons in the posterior tibial nerve at the primary somatosensory cortex [194, 195].

7.1.1 EEG Signal Preprocessing

The EEG of a healthy subject were recorded at the Department of Clinical Neurophysiology of the Sahlgrenska University Hospital, Gothenburg, Sweden. The participant (30 yrs-old) was without substance abuse or dependence and had no known neurological or psychiatric illnesses or trauma. A 61-channel EEG system was used at a sampling frequency of 2 kHz. The EEG time series were filtered (FIR, band-pass of 1–45 Hz and notch of 50 Hz), re-referenced against the common average reference, and segmented into non-overlapping 300 ms epochs using the EEGLab software [196]. Artifacts in all channels were edited off-line: first automatically, based on an absolute voltage threshold (100 mV) and on a transition threshold (50 mV), and then on the basis of a thorough visual inspection. Two electrodes with very high artifacts were removed from the recorded signals; F7 and CP1 according to the 10/10 system [191]. Using short segments for analysis allowed us to record 160 artifact-free epochs that were averaged to obtain an SNR equal to 28 dB. Then the peak of the averaged signals was used as input for the inverse problem. Fig. 7.2 shows the average of 160 stimulations for N20 at the EEG electrode positions and its topography on the subject’s head model.

7.2 Validation

Validation of the source localization is difficult, because no “ground truth” exists to make a comparison. We have taken three approaches to validate our method: first we use the physiological knowledge on localization of motor and sensory functions based on clinical expertise, second we use a standard functional imaging technique, i.e., fMRI, and third we follow an exhaustive search pattern, i.e., a brute force search for all possible locations inside the gray matter.

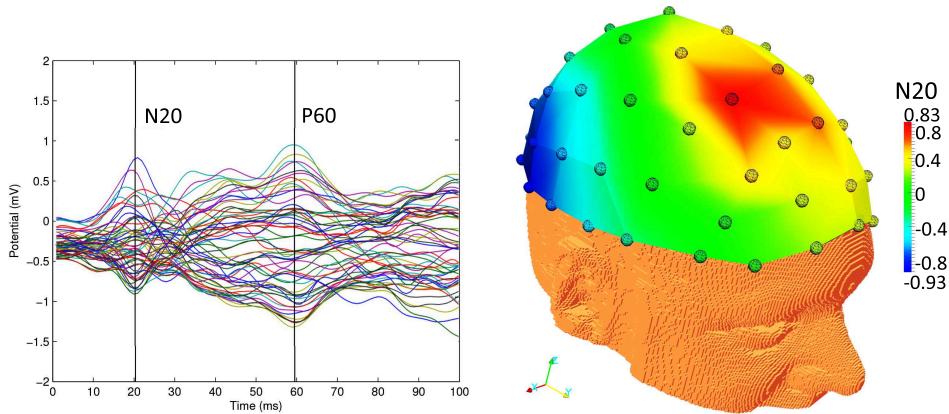


Figure 7.2: Somatosensory evoked potentials (SEPs): Butterfly plot of the averaged median nerve stimulation N20 and its late cortical activity P60 at the EEG electrode positions (left), the EEG's topography for the N20 peak (right).

7.2.1 Anatomical Validation

From direct cortical SEP studies in humans it was concluded that the postrolandic N1 (N20) reflects a horizontally oriented dipole in the posterior wall of the central sulcus [195, 197–205], see Fig. 7.3. This conclusion was supported by studies using magnetic field analysis which are particularly sensitive to horizontally oriented dipoles [206–208]. The primary cortical positivity following N20 (P60) is probably generated by radially oriented sources located immediately behind [201, 205] and in front of the central sulcus [198, 208–210], see primary motor cortex (area 4) shown in Fig. 7.3. This assumption has been supported by recent primate studies analyzing epicortical or intracortical SEPs, concomitant multi unit activity, and current source density calculations [211].

EEG source localization associated with SEP data has been well documented in the literature [213–218]. The most widely researched and clinically applied SEPs are elicited by stimulation of the median nerve at the wrist [214, 217, 218]. More recently, SEP data resulting from the stimulation of fingers or other sites have also been reported [219–223].

Thus, for the first class validation we use the physiological knowledge of localization of motor and sensory functions [224]. We consulted a clinical neurophysiology expert (from Sahlgrenska University Hospital, Gothenburg, Sweden) to localize the recorded SEPs in an independent session, and then we used those results to compare with results generated from our method. This is a valid comparison since in a daily clinical routine the pre-diagnostic localization for epilepsy

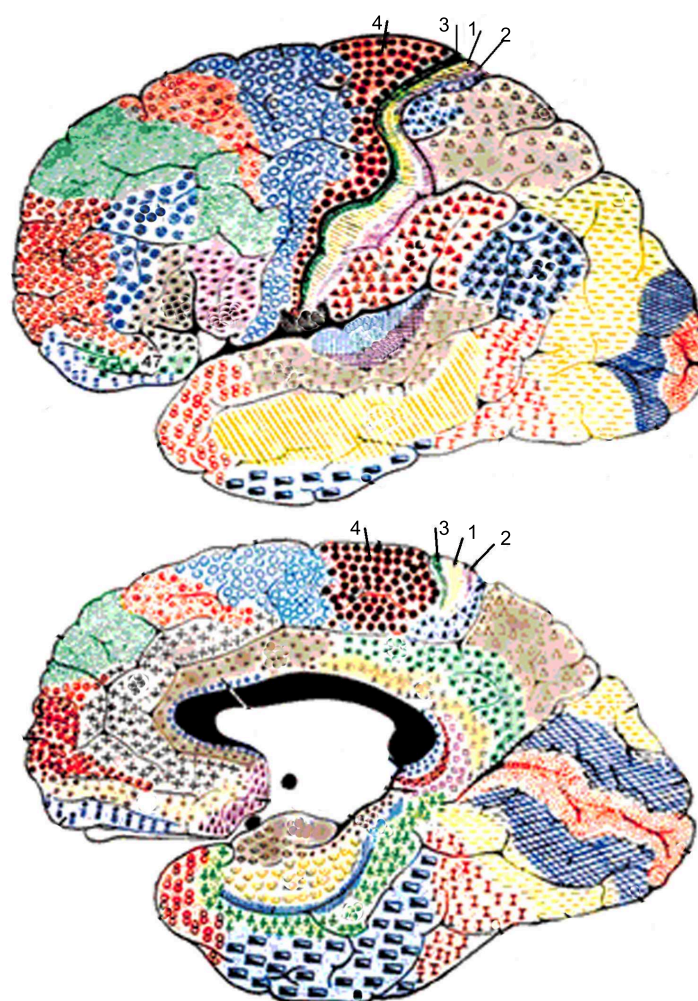


Figure 7.3: The primary somatosensory cortex (area 1, 2, and 3) and primary motor cortex (area 4). (Adopted from Brain Atlas: Brodmann Areas for fMRI [212]).

surgery is done by the same clinical expert. Fig. 7.4 shows visual images of locations and sizes of the subject's somatosensory cortical areas for the left hand marked by the clinical expert.

7.2.2 Functional Validation

Different imaging modalities including functional MRI (fMRI) and MEG have shown that the Primary Somatosensory Cortex (SI), located in the postcentral gyrus, is activated in response to cutaneous mechanical and electrical stimulation [220, 225–227] in a somatotopic manner [228]. In fact, somatosensory infor-

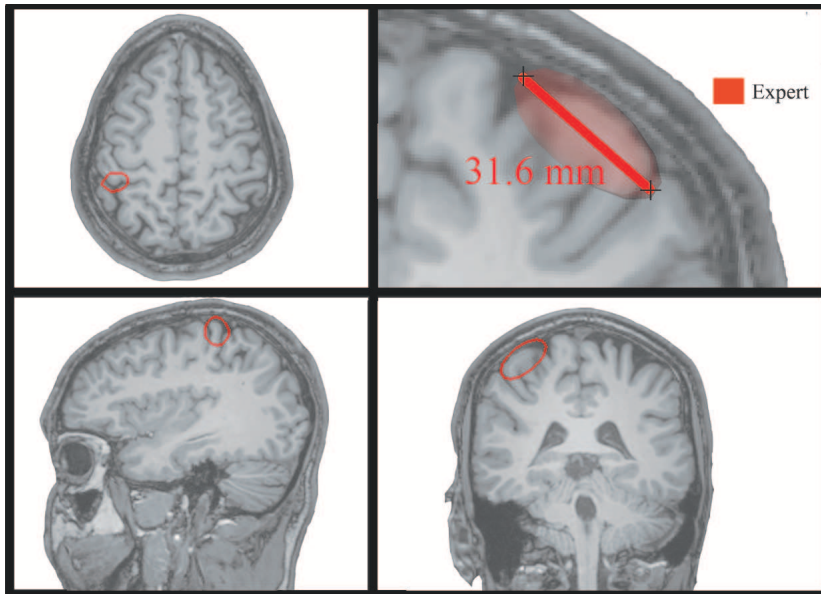


Figure 7.4: The location and size of the subject’s somatosensory cortical area which corresponds to the left hand marked by a clinical expert. (Note: MRI software shows the pictures flipped.)

mation of different body parts (such as the hand area) are represented in specific regions of SI [228, 229]. Ackerley et al. in [230] showed that touch on the left palm elicited a large positive Blood-Oxygenation Level Dependence (BOLD) signal in the right sensorimotor areas with a typical somatotopical representation in the right SI.

To get a robust activation in SI we used a similar fMRI design. A single run block design, consisting of 20 stimulation intervals interspersed by 20 rest intervals was used. The stimulation consisted of continuous brush strokes, manually delivered on the palm of the left hand. Stimulation and rest intervals lasted for 8700 ms (3TRs). The run began with a rest interval. The subject, who previously participated in the SEPs study, was instructed to lie still.

A 3T Philips Achieva MRI scanner with a 32 channels SENSE head coil was used. For functional imaging, a single-shot echo-planar imaging sequence was used (T2*-weighted, gradient echo sequence, repetition time (TR)= 2900 ms, echo time (TE) = 35 ms, flip angle = 90 deg, field-of-view (FOV) = $200 \times 244 \times 129$ mm). The functional scan consisted of 46 slices, 2.8 mm thick, with the acquisition plane oriented to the anterior-posterior commissure line and covering the whole cerebral cortex. For structural imaging a high-resolution T1-weighted anatomical protocol was used (195 sagittal slices, matrix size = 256×256 , voxel size = 0.9375 mm^3). Preprocessing and statistical analysis of MRI data was per-

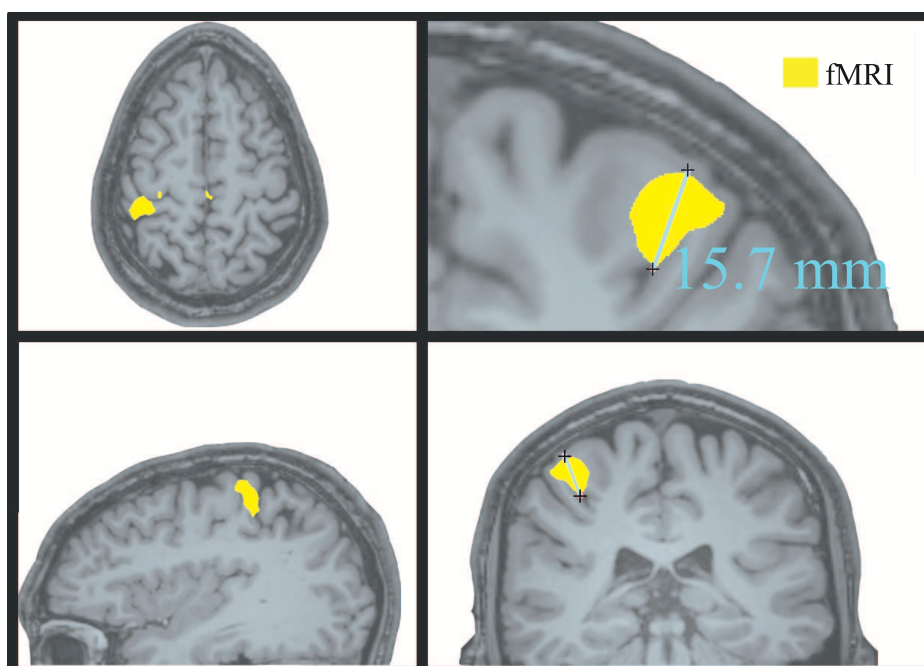


Figure 7.5: Activation in the right primary somatosensory cortex evoked by brush stimulation on the palm of the left hand. Activation displayed in radiological convention (left is right) in subject's space.

formed using BrainVoyager QX (version 2.1 Brain Innovation, Maastricht, The Netherlands). Functional data was motion corrected and low-frequency drifts were removed with a temporal high-pass filter (0.006 Hz). Spatial smoothing was applied with a Gaussian kernel (4 mm FWHM, full width at half-maximum). Functional data was manually co-registered with 3-dimensional (3D) anatomical T1 scans on the basis of anatomical landmarks. A whole brain general linear model was created for the single run. One predictor (convolved with a standard model of the hemodynamic response function) modeled the stimulation condition. The t -statistics image reflects the difference in activation between the stimulation to the rest condition, thresholded at t -value ($P < 0.0001$) of 4.

Fig. 7.5 shows the activation evoked by brush stimulation on the palm of the left hand, with the largest activation cluster in the postcentral gyrus, corresponding to the primary somatosensory cortex (SI). The 3D anatomical scan was transformed into Talairach space [231] and the parameters for this transformation were subsequently applied to the co-registered functional data. Talairach coordinates of peak activation were in: 44; -29; 51, corresponding to the postcentral gyrus according to the Talairach atlas [232].

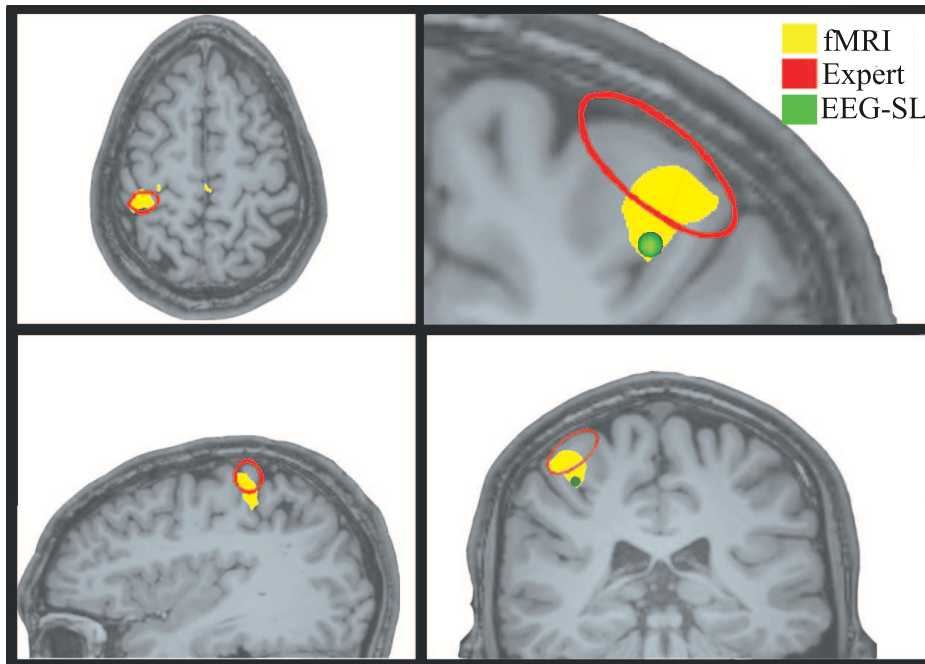


Figure 7.6: The estimated source position for median nerve stimulation on the subject's MR images.

7.2.3 Exhaustive Search

An exhaustive search was used to validate the MPSO results. We searched with brute force all gray matter voxels and the site with minimum relative error is determined, then we compare this point with results generated by MPSO. The head model has 1 mm resolution with 951 874 voxels in gray matter. All computations were performed on an Intel 2.93 GHz workstation with 8GB RAM memory and the post processing and visualizations were done using Matlab (R2012a) and the 3DSlicer (3.6.3) software [233].

7.3 Result and Discussion

We ran the source localization method for N20 signals, see Fig. 7.2, recorded from the median nerve, and compared the result with the anatomical, functional and exhaustive search methods. The manually segmented head model was used, see Section 6.2. The following conductivities were then assigned to the FE compartments based on their segmentation labels and the isotropic reference model [24, 234]: skin = 0.43 S/m, skull = 0.0042 S/m (skull to skin conductivity ratio of approximately 1:100), CSF = 1.538 S/m, gray matter = 0.33 S/m, and white matter =

0.142 S/m. First, we brutally searched all the gray matter voxels and the site with minimum relative error was determined, then we compared with results generated by MPSO. Compared to the exhaustive search MPSO was 6000 times faster and needed only around 10 milliseconds to converge.

Fig. 7.6 shows the estimated source position from all methods for median nerve stimulation on the subject's MR images. The optimization method was terminated when the minimum relative error from the exhaustive search was obtained. As we can see from Fig. 7.6, the EEG source localization result agrees well with both anatomical and functional validation methods. Although the source position is a bit deeper compared to the area marked by the clinical expert, it agrees very well with the fMRI results.

See Papers V and IX for more detailed information on the results, where the results for both median and tibial nerve stimulations for an isotropic and an anisotropic model, respectively, are presented.

Summary of the Papers

In this chapter, a brief summary of the papers included in the thesis is given. We divide the contribution into four categories; forward problem, inverse problem, real data source localization and sensitivity analysis.

8.1 Forward Problem: Papers I, VI and VII

In Papers I, VI and VII we proposed two methods for the forward problem, a modified subtraction method and a method based on the reciprocity theorem. The forward problem is a procedure to find the scalp potentials for a given current dipole(s) inside the brain.

In Papers I and VII, we introduced a modified subtraction FEM method that solves the singularity problem for the dipole sources, and improves the computational time compared to the original subtraction method. To obtain a more compact support of the right-hand side we introduced a smooth cut-off function which is identically one in a neighborhood of the dipole source. The cut-off function is radially symmetric around the dipole source, and its support is a ball with adjustable radius centered at the dipole source. We showed that a proper choice of radius led to a substantial speed up in the assembly process of the right-hand side, whilst the results had the same accuracy as the original subtraction method.

For using EEG source localization in real-time applications, such as TMS-EEG, there is a great need to speed up the solution of the forward problem to the range of seconds or less. We presented a method in Paper VI that combines the reciprocity theorem with FEM for EEG source localization. The reciprocity theorem for the electric case states that the field of the so-called lead vectors is the same as the field raised by feeding a reciprocal current to the lead. The reciprocity EEG source localization speeds up the solution of the inverse problem with more than three orders of magnitude compared to the state-of-the-art methods, which is a major advantage of this method for EEG source localization. The proposed method was tested for a four-layer spherical head model. The validation of the

method was performed by comparing the reciprocity method with analytical potentials for dipoles with eccentricity from 0 to 94%. To benchmark the proposed method, we compared it with the direct and subtraction methods. The results showed that the reciprocity method is as accurate as the subtraction method, and more accurate than the direct method. Furthermore, the reciprocity method was shown to be robust to both EEG signal noise and electrode misplacement.

8.2 Inverse Problem: Papers I, II and IX

The inverse problem is (usually) highly nonlinear and requires efficient algorithms for its solution. In Paper I, we introduced a novel particle swarm optimization (PSO) method with problem-specific modifications for the EEG source localization. The algorithm uses the velocity update properties from the original PSO, ideas from evolutionary programming and a new property, the so-called concept of authority. In Paper I, by several examples, we showed that the new algorithm finds the optimal solution significantly faster than other PSO methods from the literature, a genetic algorithm and the deterministic global optimization method, DIRECT. In addition, the MPSO is less prone to be trapped in local minima. The proposed modified PSO can also be implemented in a parallel computing environment making the inverse problem solution very cheap. Moreover, the modified PSO can easily be extended to multiple dipole source localization.

8.3 Real EEG Data: Papers II, V and IX

On the basis of our simulation results (Papers I and IV), we designed a real EEG test case with somatosensory evoked potentials (SEPs) in order to verify the proposed methods in realistic scenarios. In this study two sets of stimulations were measured: *a)* median nerve at the left wrist. *b)* the left posterior tibial nerves at the subject's ankle.

In Paper II, we applied MPSO to both median and tibial nerve stimulation as well as their late cortical activities. For the forward problem we used the modified subtraction method and an isotropic head model generated manually by a clinical expert. Comparison between the recorded EEG and estimated scalp potential topographies showed good agreement in all cases. Moreover, based on clinical expertise, the estimated sources were confirmed to be located in the correct region. The EEG source localization results obtained from MPSO gave the same results as exhaustive search, but with significantly lower computational complexity.

In Paper V, we applied MPSO to the tibial nerve stimulation. For the forward problem we used the modified subtraction method and an isotropic head model

generated automatically by the FSL software. The segmented results from FSL were corrected manually by a clinical expert. The results have a larger relative error compared to the ones obtained in Paper II due to the segmentation errors in the head model, and the fact that the source position was deeper.

In Paper IX we applied the reciprocity theorem and MPSO to the median nerve stimulations with a head model generated manually by a clinical expert and including anisotropic white matter conductivity. We used the fMRI method to validate our result. In a comparison between the EEG source localization and fMRI activities, the estimated source agrees extremely well with the fMRI activities area. The result shows that the proposed method is a step towards a clinically useful EEG source localization methodology that provides accurate, fast and robust solutions.

8.4 Sensitivity Analysis: Papers III, IV and VIII

The EEG source localization is influenced by different errors and approximations, for example source model approximations, head-modeling errors, EEG signal noise, tissue conductivity noise and electrode misplacements, as well as the numerical computational errors. For an accurate source localization, it is crucial to understand the influences of these errors on the results. To investigate this, we set up several test cases with synthetic EEG data. Generating an accurate patient-specific head model is one of the most important steps in EEG source localization and includes the segmentation, mesh generation and assigning conductivities to the respective tissues.

In Paper III, the performance of two of the most widely used software packages for brain segmentation, namely FSL [173] and FreeSurfer [175] were analyzed. Comparing with the “ground truth”, consisting of the set of voxels that were labeled by an expert, the results showed that the segmentation outputs obtained from FSL are more accurate than those from FreeSurfer, especially for the CSF compartment. Then a segmented head model from FSL was used to investigate the effects of brain tissue segmentation on EEG source localization. The results for FSL showed a 12 mm localization error in the z-direction of the estimated source.

In Paper VIII, we investigated a new fully automated segmentation method, the so-called HSA-BAMS [183], for EEG source localization. The results showed that this method can improve the source localization results by approximately 10% compared to other methods implemented in FSL such as HSA-HMRF-EM [184] and BET-FAST [174].

The complexity of the head model is another source of uncertainty. In Paper IV, six head models with different number of tissues from 4 to 9 were compared

with a reference model, i.e., a model with 10 tissues, in order to find the optimal number of tissues for the head model as well as the most important tissue for the source localization. Results showed that a model with five tissues, i.e. skin, skull, WM, GM and CSF, gave the best results. Moreover, by analyzing the results with respect to the tissues, we showed that CSF affects the results significantly.

In Paper IV the influence of EEG noise, electrode misplacements, conductivity noise and white matter anisotropy, on EEG source localization, were investigated. The results, in our test cases, showed that the source localizations are very sensitive to conductivity noise and only 4% noise can cause a 13 mm localization error. The WM anisotropy can affect the potential relative error significantly, approximately 20% in a 3D test case, but it only caused a 5 mm source localization error. In a realistic head model the electrode misplacement results showed that a 1 cm electrode misplacement caused approximately 17% potential relative error and an 8 mm localization error for the subtraction method. In Paper VI, the influences of electrode misplacement for the reciprocity forward method were investigated in the spherical head model. The results showed that the reciprocity method is more robust with respect to electrode misplacement. One centimeter electrode misplacement only caused a 2 mm source localization error. Our investigation of EEG signals noise in Papers I, IV and VI showed that both the subtraction and reciprocity methods are robust with respect to EEG signal noise.

Conclusions and Outlook

This thesis deals with different aspects of EEG source localization and pays particular attention to reducing the computational complexity. Reflecting on the shortcomings of pre-existing methods, we have developed a method based on the reciprocity theorem and particle swarm optimization. Encouraging results, expressed in different performance indicators as well as in comparison with other existing methods, have been demonstrated for localization of different spike sources inside the brain. The results show accurate localization with a very fast computation time (in the range of milliseconds). We designed real EEG test cases with somatosensory evoked potentials (SEPs) in order to verify the proposed method in realistic scenarios. The feasibility of the proposed source localization method was tested for median and tibial nerves evoked potentials. The results agreed very well with both the fMRI palm-brushing measurement and the clinical expert results. The computational time for localizing the SEP signals was 5 milliseconds.

The sensitivity analyses in this thesis contribute the understanding of the nature of the problem and its limitations. The numerical results show that the head model segmentation is the most important step in the EEG source localization and that inaccurate segmentations produce erroneous localization results

The numerical and experimental results presented in this thesis have shown that our proposed method based on the reciprocity theorem and the MPSO method is a good choice for EEG source localization. These results need to be confirmed clinically on real epileptic spikes by using subdural EEG recordings and brain surgery outcomes for validation. [235–237]. From a technical point of view there are still several issues that need to be improved. The existing segmentation methods should be improved to generate a more accurate head model automatically. Moreover, in the future, a further effort is needed for the measurement of human head tissue conductivities, especially concerning the skull anisotropy. Animal models can be a good alternative to provide the necessary validation on a more controlled level, i.e., the implantation of deep electrodes and their EEG reconstruction with and without tissue anisotropy modeling (see [238, 239]).

Knowing the position of the EEG electrodes is also very important in EEG

source localization. Although most of the EEG electrode digitizers used in a clinical measurement routine have measurement accuracy of around 1 mm, patient movements during the recording can change their positions. To avoid electrode misplacement error there is a strong need to develop an electrode positioning system which can localize the electrode positions over time [240].

Using the fast EEG source localization method proposed here, a future exciting application is a non-invasive treatment method for epilepsy using EEG simultaneous-localization guided repetitive transcranial magnetic stimulation (rTMS-EEG) [241]. This method can be an alternative to the conventional epilepsy surgery treatment. Moreover, since skull inhomogeneities have a large effect on EEG, another interesting application field for the proposed method would be newborns with open sutures (see [242]).

Bibliography

- [1] D. L. Kraeme, M. E. Brandling-Bennett, and D. G. Vossler. Epilepsy surgery. *Medscape reference, Drug, Diseases and Procedures*, 2011.
- [2] P. Kwan, A. Arzimanoglou, A. T. Berg, M. J. Brodie, H. W. Allen, G. Mathern, S. L. Moshe, E. Perucca, S. Wiebe, and J. French. Definition of drug resistant epilepsy: Consensus proposal by the ad hoc task force of the ILAE commission on therapeutic strategies. *Epilepsia*, 51(6):1069–1077, 2010.
- [3] J. Engel, S. Wiebe, J. French, M. Sperling, P. Williamson, D. Spencer, R. Gumnit, C. Zahn, E. Westbrook, and B. Enos. Practice parameter: Temporal lobe and localized neocortical resections for epilepsy. *Epilepsia*, 44(6):741–751, 2003.
- [4] S. Spencer, A. T. Berg, B. G. Vickrey, M. R. Sperling, C. W. Bazil, S. Shinnar, J. T. Langfitt, T. S. Walczak, S. V. Pacia, N. Ebrahimi, and D. Frobish. Initial outcomes in the multicenter study of epilepsy surgery. *Neurology*, 61(12):1680–1685, 2003.
- [5] J. S. Ebersole. Defining epileptogenic foci: Past, present, future. *Clin. Neurophysiol.*, 14:470–483, 1997.
- [6] Q. Chen and S. Lui. MRI-negative refractory partial epilepsy: Role for diffusion tensor imaging in high field MRI. *Epilepsy Research*, 80:83–89, 2008.
- [7] H. Berger. Über das Elektrenkephalogramm des Menschen. *Arch. Psychiat. Nervenkr.*, 87:527–570, 1929.
- [8] J. C. de Munck. The potential distribution in a layered anisotropic spheroidal volume conductor. *Journal of Applied Physics*, 64(2):464–470, 1988.
- [9] M. Sun. An efficient algorithm for computing multishell spherical volume conductor models in EEG dipole source localization. *IEEE Trans. Biomedical Engineering*, 44(12):1243–1252, 1997.

-
- [10] C. Ramon, P. H. Schimpf, and J. Haueisen. Influence of head models on EEG simulations and inverse source localizations. *Biomed Eng. Online*, 5(10), 2006.
- [11] Y. Shirvany, X. Chen, P. Sharad Dhanpalwar, M. MirHashemi, F. Edelvik, and M. Persson. Influence of different sources of noise on epileptic spike EEG source localization. In *SPIE Medical Imaging: Biomedical Applications in Molecular, Structural, and Functional Imaging*, volume 8672, 2013.
- [12] L. A. Geddes and L. E. Baker. The specific resistance of biological materials: A compendium of data for the biomedical engineer and physiologist. *Med. Biol. Eng. Comput.*, 5:271–293, 1967.
- [13] M. Akhtari, H. C. Bryant, A. N. Mamelak, L. Heller, J.J. Shih, M. Mandelkern, A. Matlachov, D. M. Ranken, E. D. Best, and W. W. Sutherling. Conductivities of three-layer human skull. *Brain Topography*, 13(1):29–42, 2000.
- [14] S. Rush and D. A. Driscoll. Current distribution in the brain from surface electrodes. *Anesthesia and Analgesia*, 47(6):717–723, 1968.
- [15] P. W. Nicholson. Specific impedance of cerebral white matter. *Experimental Neurology*, 13(4):386 – 401, 1965.
- [16] P. J. Basser, J. Mattiello, and D. LeBihan. MR diffusion tensor spectroscopy and imaging. *Biophysical Journal*, 66(1):259–267, 1994.
- [17] D. A. S. Tuch, V. J. Wedeen, A. M. Dale, J. S. George, and J. W. Belliveau. Conductivity mapping of biological tissue using diffusion MRI. *Annals of the New York Academy of Sciences*, 888(1):314–316, 1999.
- [18] M. Sekino, Y. Inoue, and S. Ueno. Magnetic resonance imaging of electrical conductivity in the human brain. *Magnetics, IEEE Transactions on*, 41(10):4203–4205, 2005.
- [19] M. Sekino, K. Yamaguchi, N. Iriguchi, and S. Ueno. Conductivity tensor imaging of the brain using diffusion-weighted magnetic resonance imaging. *Journal of Applied Physics*, 93(10):6730–6732, 2003.
- [20] B. N. Cuffin, D. Cohen, K. Yunokuchi, R. Maniewski, C. Purcell, G. R. Cosgrove, J. Ives, J. Kennedy, and D. Schomer. Tests of EEG localization accuracy using implanted sources in the human brain. *Annals of Neurology*, 29(2):132–138, 1991.

- [21] J. R. Bradley, B. Marshall, G. Alexander, and S. Susumu. How well does a three-sphere model predict positions of dipoles in a realistically shaped head? *Electroencephalography and Clinical Neurophysiology*, 87(4):175 – 184, 1993.
- [22] S. P. van den Broek, F. Reinders, M. Donderwinkel, and M. J. Peters. Volume conduction effects in EEG and MEG. *Electroencephalography and Clinical Neurophysiology*, 106(6):522 – 534, 1998.
- [23] G. Marin, C. Guerin, S. Baillet, L. Garnero, and G. Meunier. Influence of skull anisotropy for the forward and inverse problem in EEG: Simulation studies using FEM on realistic head models. *Human Brain Mapping*, 6(4):250–269, 1998.
- [24] J. Haueisen, D. S. Tuch, C. Ramon, P. H. Schimpf, V. J. Wedeen, J. S. George, and J. W. Belliveau. The influence of brain tissue anisotropy on human EEG and MEG. *NeuroImage*, 15(1):159–166, 2002.
- [25] J. Haueisen, C. Ramon, P. Czapski, and M. Eiselt. On the influence of volume currents and extended sources on neuromagnetic fields: A simulation study. *Annals of Biomedical Engineering*, 23(6):728–739, 1995.
- [26] J. Haueisen, C. Ramon, H. Brauer, and H. Nowak. The influence of local conductivity changes on MEG and EEG. *Biomedizinische Technik*, 45(7):211–214, 2000.
- [27] H. Buchner, G. Knoll, M. Fuchs, A. Rienäcker, R. Beckmann, M. Wagner, J. Silny, and J. Pesch. Inverse localization of electric dipole current sources in finite element models of the human head electroencephalogr. *Clin. Neurophysiol.*, 102:267–268, 1997.
- [28] K. A. Awada, D. R. Jackson, J. T. Williams, D. R. Wilton, S. B. Baumann, and A. C. Papanicolaou. Computational aspects of finite element modeling in EEG source localization. *Biomedical Engineering, IEEE Transactions on*, 44(8):736–752, 1997.
- [29] C. H. Wolters, M. Kuhn, A. Anwander, and S. Reitzinger. A parallel algebraic multigrid solver for finite element method based source localization in the human brain. *Computing and Visualization in Science*, 5(3):165–177, 2002.
- [30] C. H. Wolters, H. Köstler, C. Härdtlein, J. Möller, L. Grasedyck, and W. Hackbusch. Numerical mathematics of the subtraction method for the

- construction of a current dipole in EEG source reconstruction using finite element head models. *SIAM J. Scientific Computing*, 30(1):24–45, 2007.
- [31] G. Lantz, R. Grave de Peralta, L. Spinelli, M. Seeck, and C. M. Michel. Epileptic source localization with high density eeg: how many electrodes are needed? *Clinical Neurophysiology*, 114(1):63 – 69, 2003.
- [32] C. C. Wood. Application of dipole localization methods to source identification of human evoked potentials. *Annals of the New York Academy of Sciences*, 388(1):139–155, 1982.
- [33] C. Plummer, L. Litewka, S. Farish, A. S. Harvey, and M. J. Cook. Clinical utility of current-generation dipole modelling of scalp EEG. *Clinical Neurophysiology*, 118(11):2344–2361, 2007.
- [34] C. Plummer, M. Wagner, M. Fuchs, S. Vogri, L. Litewka, S. Farish, Bailey C., A. S. Harvey, and Cook M. J. Clinical utility of distributed source modelling of interictal scalp EEG in focal epilepsy. *Clinical Neurophysiology*, 121(10):1726–1739, 2010.
- [35] C. Plummer, M. Wagner, M. Fuchs, A. S. Harvey, and M. J. Cook. Dipole versus distributed EEG source localization for single versus averaged spikes in focal epilepsy. *J. Clin Neurophysiol.*, 27:141–162, 2010.
- [36] R. D. Pascual-Marqui. Standardized low-resolution brain electromagnetic tomography (sloreta): technical details. *Methods Find Exp Clin Pharmacol.*, 24:5–12, 2002.
- [37] M. Scherg and D. von Cramon. Two bilateral sources of the late AEP as identified by a spatio-temporal dipole model electroencephalogr. *Clin. Neurophysio.*, 6(1):32–44, 1985.
- [38] J. C. Mosher, P. S. Lewis, and R. M. Leahy. Multiple dipole modeling and localization from spatio-temporal MEG data. *IEEE Trans. Biomed. Eng.*, 39(6):541–557, 1992.
- [39] C. H. Wolters, R. F. Beckmann, A. Rienäcker, and H. Buchner. Comparing regularized and non-regularized nonlinear dipole fit methods: A study in a simulated sulcus structure. *Brain Topography*, 12(1):3–18, 1999.
- [40] M. S. Hämäläinen and R. J. Ilmoniemi. Interpreting magnetic fields of the brain: minimum norm estimates. *Medical & Biological Engineering & Computing*, 32(1):35–42, 1994.

- [41] M. Fuchs, M. Wagner, T. Köhler, and H. A. Wischmann. Linear and nonlinear current density reconstructions. *Jour. Clin. Neurophysiol.*, 16(3):267–295, 1999.
- [42] S. Baillet and L. Garnero. A bayesian approach to introducing anatomofunctional priors in the EEG/MEG inverse problem. *IEEE Trans. Biomed. Eng.*, 44(5):374–385, 1997.
- [43] G. Lantz, M. Spinelli, L. Seeck, R. G. de Peralta Menendez, C. C. Sotatas, and C. M. Michel. Propagation of interictal epileptiform activity can lead to erroneous source localizations: A 128-channel EEG mapping study. *Journal of Clinical Neurophysiology*, 20(5):311–319, 2003.
- [44] I. C. Mircea and S. J. Mandar. Spike source localization with tetrodes. *Journal of Neuroscience Methods*, 142(2):305–315, 2005.
- [45] S. van den Broeh, H. Zhou, and M. Peters. Computation of neuromagnetic fields using Finite-Element method and Biot-Savart law. *Medical and Biological Engineering and Computing*, 34(1):21–26, 1996.
- [46] F. Edelvik, B. Andersson, S. Jakobsson, S. Larsson, M. Persson, and Y. Shirvany. An improved method for dipole modeling in EEG-based source localization. In *World Congress on Medical Physics and Biomedical Engineering*, volume 25 of *IFMBE Proceedings*, pages 146–149. 2009.
- [47] Y. Shirvany, A. R. Porras, K. Kowkabzadeh, Q. Mahmood, Hoi-Shun Lui, and M. Persson. Investigation of brain tissue segmentation error and its effect on eeg source localization. In *Engineering in Medicine and Biology Society (EMBC), 2012 Annual International Conference of the IEEE*, pages 1522–1525, 28 2012-sept. 1 2012.
- [48] Y. Wang and J. Gotman. The influence of electrode location errors on EEG dipole source localization with a realistic head model. *Clinical Neurophysiology*, 112(9):1777 – 1780, 2001.
- [49] D. Khosla, M. Don, and B. Kwong. Spatial mislocalization of EEG electrodes effects on accuracy of dipole estimation. *Clinical Neurophysiology*, 110(2):261 – 271, 1999.
- [50] A. Anwander, C. H. Wolters, M. Dümpelmann, and T. R. Knösche. Influence of realistic skull and white matter anisotropy on the inverse problem in EEG/MEG-source localization. In *Proceedings of the 13th International Conference on Biomagnetism (BIOMAG 2002)*, 2002.

-
- [51] H. Hallez, B. Vanrumste, R. Grech, J. Muscat, W. De Clercq, A. Vergult, Y. D'Asseler, K. P. Camilleri, S. G. Fabri, S. Van Huffel, and I. Lemahieu. Review on solving the forward problem in EEG source analysis. *Neuro-engineering and Rehabilitation*, 46(4), 2007.
- [52] C. M. Michel, M. M. Murray, G. Lantz, S. Gonzalez, L. Spinelli, and R. Grave de Peralta. EEG source imaging. *Clinical Neurophysiology*, 115(10):2195–2222, 2004.
- [53] T. D. Waberski, H. Buchner, K. Lehnertz, A. Hufnagel, M. Fuchs, R. Beckmann, and A. Rienäcker. The properties of source localization of epileptiform activity using advanced headmodelling and source reconstruction. *Brain Top.*, 10(4):283–290, 1998.
- [54] H. L. Attwood and W. A. MacKay. *Essentials of Neurophysiology*. B. C. Decker, Hamilton, Canada, 1989.
- [55] D. A. Drachman. Do we have brain to spare? *Neurology*, 64(12):2004–2005, 2005.
- [56] L. G. Kiloh, A. J. McComas, J. W. Osselton, and A. R. M. Upton. *Clinical Electroencephalography*. Butterworth-Heinemann, 3rd edition, 1981.
- [57] H. Gray. *Gray's Anatomy*. Longman Group Ltd, 1973.
- [58] S. Sanei and J. A. Chambers. *EEG Signal Processing*. John Wiley and Sons Ltd, 2007.
- [59] E. R. Kandel and J. H. Schwartz. *Principles of Neural Science*. Elsevier Noth Holland, Inc., New York, 1982.
- [60] E. Niedermeyer and S. F. Lopes. *Electroencephalography: Basic Principles, Clinical Applications, and Related Fields*. Lippincott Williams & Wilkins, 2005.
- [61] R. M. Gulrajani. *Bioelectricity and Biomagnetism*. John Wiley and Sons, Inc, 1998.
- [62] K. X. Charand. <http://hyperphysics.phy-astr.gsu.edu/hbase/biology/actpot.html>.
- [63] S. Baillet, J. C. Mosher, and R. M. Leahy. Electromagnetic brain mapping. pages 14–30, 2001.

- [64] R. Plonsey and D. Heppner. Considerations on quasi-stationarity in electrophysiological systems. *Bull. math. Biophys*, 29(4):657–664, 1967.
- [65] D. K. Cheng. *Field and wave electromagnetics*. Addison-Wesley series in electrical engineering. Addison-Wesley, 1989.
- [66] Y. Okada. Neurogenesis of evoked magnetic fields biomagnetism. *ed S. N. Erne, H. D. Hahlbohm and H. Lübbig*, pages 399–408, 1981.
- [67] J. C. de Munck, B. W. van Dijk, and H. Spekreijse. Mathematical dipoles are adequate to describe realistic generators of human brain activity. *IEEE Trans. Biomed. Eng.*, 35(11):960–966, 1988.
- [68] P. Nunez. Localization of brain activity with electroencephalography advances in neurology. *Magnetoencephalography*, 54:39–65, 1990.
- [69] E. Frank. Electric potential produced by two point current sources in a homogeneous conduction sphere. *Journal of Applied Physics*, 23(11):1225–1228, 1952.
- [70] J. P. Ary, S. A. Klein, and D. H. Fender. Location of sources of evoked scalp potentials: Corrections for skull and scalp thicknesses. *Biomedical Engineering, IEEE Transactions on*, 28(6):447–452, 1981.
- [71] Y. Salu, L.G. Cohen, D. Rose, S. Sxato, C. Kufta, and M. Hallett. An improved method for localizing electric brain dipoles. *Biomedical Engineering, IEEE Transactions on*, 37(7):699–705, 1990.
- [72] M. A. Huerta and G. Gonzalez. The surface potentials produced by electric sources in stratified spherical and prolate spheroidal volume conductors. *International Journal of Electronics*, 54(5):657–671, 1983.
- [73] J. de Munck and M. Peters. A fast method to compute the potential in the multiphere model. *IEEE Transactions on Biomedical Engineering*, 40(11):1166–1174, 1993.
- [74] J. M. Jin. *The Finite Element Method in Electromagnetics*. New York: John Wiley & Sons, 1993.
- [75] J. M. Jin. *The Finite Element Method in Electromagnetics (2nd Edition)*. New York: John Wiley & Sons, 2002.
- [76] A. F. Peterson, S. L. Ray, and R. Mittra. *Computational Methods for Electromagnetics*. The IEEE/OUP Series on Electromagnetic Wave Theory and Oxford University Press, 1997.

-
- [77] T. Rylander, P. Ingelström, and A. Bondeson. *Computational Electromagnetics*. Addison-Wesley series in electrical engineering. Springer; 2nd ed., 2012.
- [78] M. Benzi, G. Benzi, H. Gene, and J. Liesen. Numerical solution of saddle point problems. *Acta Numerica*, 14:1–137, 2005.
- [79] Y. Yan, P. L. Nunez, and R. T. Hart. Finite-element model of the human head: Scalp potentials due to dipole sources. *Med. Biol. Engrg. Comput.*, 29(5):475–481, 1991.
- [80] P. H. Schimpf, C. Ramon, and J. Haueisen. Dipole models for the EEG and MEG. *IEEE Trans. Biomedical Engineering*, 49(5):409–418, 2002.
- [81] F. Drechsler, C. H. Wolters, T. Dierkes, H. Si, and L. Grasedyck. A full subtraction approach for finite element method based source analysis using constrained delaunay tetrahedralisation. *NeuroImage*, 46(4):1055–1065, 2009.
- [82] H. Helmholtz. Ueber einige Gesetz der Vertheilung elektrischer Ströme in körperlichen Leitern, mit Anwendung auf die thierisch-elektrischen Versuche. *Annalen der Physik*, 165(6):211–233, 1853.
- [83] S. Rush and D. A. Driscoll. EEG Electrode Sensitivity-An Application of Reciprocity. *Biomedical Engineering, IEEE Transactions on*, 16(1):15–22, 1969.
- [84] A. K. Liu, J. W. Belliveau, and A. M. Dale. Spatiotemporal imaging of human brain activity using functional MRI constrained magnetoencephalography data: Monte carlo simulations. *Proceedings of the National Academy of Sciences*, 95(15):8945–8950, 1998.
- [85] M. Wagner, M. Fuchs, and J. Kastner. fMRI-constrained dipole fits and current density reconstructions, 2000.
- [86] V. Menon, J. M. Ford, K. O. Lim, G. H. Glover, and A. Pfefferbaum. Combined event-related fMRI and EEG evidence for temporal-parietal cortex activation during target detection. *Neuro Report*, 8(14):3029–3037, 1997.
- [87] B. Opitz, A. Mecklinger, D. Y. von Cramon, and F. Kruggel. Combining electrophysiological and hemodynamic measures of the auditory oddball. *Psychophysiology*, 36(1):142–147, 1999.

- [88] Jr. H.G. Vaughan. The analysis of scalp-recorded brain potentials. In *R.F. Thompson and M.M. Patterson, editors, Bioelectric Recording Techniques*, pages 158–207, Part B. Academic Press, New York, 1974.
- [89] M. Hämäläinen and R.J. Ilmoniemi. Interpreting measured magnetic fields of the brain: Estimates of current distributions. *Techn. Report TKKF-A559, Helsinki University of Technology*, 1984.
- [90] M. Wagner, M. Fuchs, H. A. Wischmann, R. Drenckhahn, and T. Köhler. Current density reconstructions using the L1-norm. In *In Proc. of the 10th Int. Conf. of Biomagnetism Santa Fe*, pages 158–207, 1996.
- [91] T. R. Knösche. *Solutions of the neuroelectromagnetic inverse problem: an Evaluation Study*. PhD thesis, University of Twente, The Netherlands, 1997.
- [92] U. Schmitt and A. K. Louis. Efficient algorithms for the regularization of dynamic inverse problems: I. Theory. *Inverse Problems*, 18(3):645–658, 2002.
- [93] U. Schmitt, A. K. Louis, C. H. Wolters, and M. Vauhkonen. Efficient algorithms for the regularization of dynamic inverse problems: II. Applications. *Inverse Problems*, 18(3):659–676, 2002.
- [94] J. C. De Munck. The estimation of time varying dipoles on the basis of evoked potentials. *Electroencephalography and Clinical Neurophysiology*, 77:156–160, 1990.
- [95] R. Grech, T. Cassar, J. Muscat, K. P. Camilleri, S. G. Fabri, M. Zervakis, P. Xanthopoulos, V. Sakkalis, and B. Vanrumste. Review on solving the inverse problem in EEG source analysis. *Journal of NeuroEngineering and Rehabilitation*, 5(25), 2008.
- [96] D. M. Schmidt, J. S. George, and C. C. Wood. Bayesian inference applied to the electromagnetic inverse problem. *Physics Division*, pages 1997–1998, 2002.
- [97] C. Silva, J. C. Maltez, E. Trindade, A. Arriaga, and E. Ducla-Soares. Evaluation of L1 and L2 minimum-norm performances on EEG localizations. *Clinical Neurophysiology*, 115(7):1657–1668, 2004.
- [98] K. A. Moores, C. R. Clark, Jo L. M. Hadfield, G. C. Brown, D. J. Taylor, S. P. Fitzgibbon, A. C. Lewis, D. L. Weber, and R. Greenblatt. Investigating the generators of the scalp recorded visuo-verbal P300 using cortically constrained source localization. *Human Brain Mapping*, 18(1):53–77, 2003.

- [99] C. M. Michel, R. G. De Peralta, G. Lantz, S. G. Andino, L. Spinelli, O. Blanke, and M. Landis, T. Seeck. Spatiotemporal EEG analysis and distributed source estimation in presurgical epilepsy evaluation. *Journal of Clinical Neurophysiology*, 16(3):239–266, 1999.
- [100] W. E. Kincses, C. Braun, S. Kaiser, and T. Elbert. Modeling extended sources of event-related potentials using anatomical and physiological constraints. *Human Brain Mapping*, 8(4):182–193, 1999.
- [101] R. G. D. Menendez and S. L. G. Andino. Discussing the capabilities of Laplacian minimization. *Brain Topography*, 13(2):97–104, 2000.
- [102] R. G. D. Menendez and S. L. G. Andino. A critical analysis of linear inverse solutions to the neuroelectromagnetic inverse problem. *Biomedical Engineering, IEEE Transactions on*, 45(4):440–448, 1998.
- [103] D. W. Marquardt. An algorithm for least-squares estimation of nonlinear parameters. *J. Soc. Indust. Appl. Math.*, 11(2):431–441, 1963.
- [104] J. Nelder and R. Mead. A simplex method for function minimization. *Comput. J.*, 7(4):308–313, 1965.
- [105] D. Z. Yao. Electric theory and techniques of brain functional prospecting. (*In Chinese*), Beijing: Science Press, 2003.
- [106] D. C. Fernandez, R. G. Menendez, , and S. L. Gonzalez. Some limitations of spatio temporal source models. *Brain Topogr.*, 7(3):233–243, 1995.
- [107] Z. J. Koles. Trends in EEG source localization. *Electroencephalography and Clinical Neurophysiology*, 106(2):127–137, 1998.
- [108] M. Huang, C. J. Aine, S. Supek, E. Best, D. Ranken, and E. R. Flynn. Multi-start downhill simplex method for spatio-temporal source localization in magnetoencephalography. *Electroencephalography and Clinical Neurophysiology/Evoked Potentials Section*, 108(1):32–44, 1998.
- [109] J. C. Mosher and R. M. Leahy. Recursive MUSIC: A framework for EEG and MEG source localization. *Biomedical Engineering, IEEE Transactions on*, 45(11):1342–1354, 1998.
- [110] C. M. Michel, M. M. Murray, G. Lantz, S. Gonzalez, L. Spinelli, and R. Grave de Peralta. EEG source imaging. *Clinical Neurophysiology*, 115(10):2195–2222, 2004.

- [111] A. Polonsky and M. Zibulevsky. MEG/EEG source localization using spatio-temporal sparse representations. In *Independent Component Analysis and Blind Signal Separation*, volume 3195, pages 1001–1008. 2004.
- [112] C. W. Hesse and C. J. James. On semi-blind source separation using spatial constraints with applications in EEG analysis. *Biomedical Engineering, IEEE Transactions on*, 53(12):2525–2534, 2006.
- [113] A. Gramfort, D. Strohmeier, J. Haueisen, M. Hämäläinen, and M. Kowalski. Functional brain imaging with M/EEG using structured sparsity in time-frequency dictionaries. In *Information Processing in Medical Imaging*, volume 6801, pages 600–611. 2011.
- [114] R. G. Menendez and S. L. Gonzalez. Single dipole localization: Some numerical aspects and a practical rejection criterion for the fitted parameters. *Brain Topogr.*, 6(4):277–282, 1994.
- [115] D. McNay, E. Michielssen, R. L. Rogers, S. A. Taylor, M. Akhtari, and W. W. Sutherling. Multiple source localization using genetic algorithms. *Journal of Neuroscience Methods*, 64(2):163–172, 1996.
- [116] K. Uutela, M. Hämäläinen, and R. Salmelin. Global optimization in the localization of neuromagnetic sources. *Biomedical Engineering, IEEE Transactions on*, 45(6):716–723, 1998.
- [117] D. Khosla, M. Singh, and M. Don. Spatio-temporal EEG source localization using simulated annealing. *IEEE Transactions on Biomedical Engineering*, 44(11):1075–1090, 1997.
- [118] C. Sequeira, F. Sanchez-Quesada, M. Sancho, I. Hidalgo, and T. Ortiz. A genetic algorithm approach for localization of deep sources in MEG. *Physica Scripta*, 118:140–142, 2005.
- [119] C. Jiang, J. Ma, B. Wang, and L. Zhang. Multiple signal classification based on genetic algorithm for meg sources localization. *Lecture Notes in Computer Science, NUMB*, 4492:1133–1139, 2007.
- [120] L. Qiu, Y. Li, and D. Yao. A feasibility study of EEG dipole source localization using particle swarm optimization. In *Evolutionary Computation, 2005. The 2005 IEEE Congress on*, volume 1, pages 720–726, 2005.
- [121] R. Eberhart and J. Kennedy. A new optimizer using particle swarm theory. In *Micro Machine and Human Science, 1995. MHS '95., Proceedings of the Sixth International Symposium on*, pages 39–43, 1995.

- [122] J. Kennedy and R. Eberhart. Particle swarm optimization. In *Neural Networks, 1995. Proceedings., IEEE International Conference on*, volume 4, pages 1942–1948, 1995.
- [123] M. A. Abido. Optimal design of power system stabilizers using particle swarm optimization. *IEEE Trans. Energy Conversion*, 17(3):406–413, 2002.
- [124] D. K. Agrafiotis and W. Cedeno. Feature selection for structure-activity correlation using binary particle swarms. *Journal of Medicinal Chemistry*, 45(5):1098–1107, 2002.
- [125] K. E. Parsopoulos and M. N. Vrahatis. Initializing the particle swarm optimizer using the nonlinear simplex method. In *Advances in Intelligent Systems, Fuzzy Systems, Evolutionary Computation*, pages 216–221, 2002a.
- [126] K. E. Parsopoulos and M. N. Vrahatis. Recent approaches to global optimization problems through particle swarm optimization. *Natural Computing*, 1(2):235–306, 2002b.
- [127] N. G. Pavlidis, K. E. Parsopoulos, and M.N. Vrahatis. Computing nash equilibria through computational intelligence methods. *Journal of Computational and Applied Mathematics*, 175:113–136, 2005.
- [128] Y. G. Petalas, K. E. Parsopoulos, and M. N. Vrahatis. Stochastic optimization for detecting periodic orbits of nonlinear mappings. *Nonlinear Phenomena in Complex Systems*, 11(2):285–291, 2008.
- [129] C. Skokos, K. E. Parsopoulos, P. A. Patsis, and M. N. Vrahatis. Particle swarm optimization: an efficient method for tracing periodic orbits in 3D galactic potentials. *Monthly Notices of the Royal Astronomical Society*, 359(1):251–260, 2005.
- [130] T. Ray and K. M. Liew. A swarm metaphor for multiobjective design optimization. *Engineering Optimization*, 34(2):141–153, 2002.
- [131] A. Saldam, I. Ahmad, and S. Al-Madani. Particle swarm optimization for task assignment problem. *Microprocessors and Microsystems*, 26(8):363–371, 2002.
- [132] W. Cedeno and D. Agrafiotis. A comparison of particle swarms techniques for the development of quantitative structure-activity relationship models for drug design. In *IEEE 2005 Computational Systems Bioinformatics Conference*, pages 322–331, 2005.

- [133] N. Forghani, M. Forouzanfar, and E. Forouzanfar. MRI fuzzy segmentation of brain tissue using IFCM algorithm with particle swarm optimization. In *Proc. 22nd Int. Symp. Computer and Information Sciences (ISCIS)*, pages 1–4, 2007.
- [134] V. L. Georgiou, N. G. Pavlidis, K. E. Parsopoulos, P. D. Alevizos, and M. N. Vrahatis. New self adaptive probabilistic neural networks in bioinformatics and medical tasks. *International Journal on Artificial Intelligence Tools*, 15(3):371–396, 2006.
- [135] Y. Liu, J. Zhou, and Y. Chen. Ensemble classification for cancer data. In *Proc. 2008 Int. Conf. Biomedical Engineering and Informatics (BMEI)*, pages 269–273, 2008.
- [136] O. Mohamed and A. Adel. Particle swarm optimization based stroke volume influence on mean arterial pressure. In *Proc. Int. Conf. Biomedical and Pharmaceutical Engineering (ICBPE)*, pages 508–512, 2006.
- [137] A. Nakib, S. Roman, H. Oulhadj, and P. Siarry. Fast brain mri segmentation based on two-dimensional survival exponential entropy and particle swarm optimization. In *Proc. 29th Ann. Int. Conf. IEEE Engineering in Medicine and Biology Society (EMBS)*, pages 5563–5566, 2007.
- [138] M. P. Wachowiak, R. Smolikova, Y. Zheng, J. M. Zurada, and A. S. Elmaghraby. An approach to multimodal biomedical image registration utilising particle swarm optimization. *IEEE Transactions on Evolutionary Computation*, 8(3):289–301, 2004.
- [139] L. Xie and L. Jiang. Global optimal ICA and its application in brain MEG data analysis. In *Proceedings of the 2005 Int. Conf. Neural Networks and Brain*, pages 353–357, 2005.
- [140] C. Xu, Q. Zhang, B. Wang, and R. Zhang. Research on the DNA sequence design based on GA/PSO algorithms. In *Proc. 2nd Int. Conf. Bioinformatics and Biomedical Engineering (ICBBE)*, pages 816–819, 2008.
- [141] C. S. Yang, L. Y. Chuang, J. C. Li, and C. H. Yang. A novel BPSO approach for gene selection and classification of microarray data. In *Proc. IEEE 2008 Int. Joint Conf. Neural Networks (IJCNN)*, 2008.
- [142] X. Zhang and T. Li. Improved particle swarm optimization algorithm for 2D protein folding prediction. In *Proc. 1st Int. Conf. Bioinformatics and Biomedical Engineering (ICBBE 2007)*, pages 53–56, 2007.

-
- [143] J. Kennedy, R. C. Eberhart, and Y. Shi. *Swarm Intelligence*. Morgan Kaufmann, 1st edition, 2001.
- [144] Y. Shi and R. Eberhart. A modified particle swarm optimizer. In *Evolutionary Computation Proceedings, 1998. IEEE World Congress on Computational Intelligence., The 1998 IEEE International Conference on*, pages 69–73, 1998.
- [145] Y. Shi and R. C. Eberhart. Parameter Selection in Particle Swarm Optimization. In *EP '98: Proceedings of the 7th International Conference on Evolutionary Programming VII*, pages 591–600, London, UK, 1998. Springer-Verlag.
- [146] M. Clerc. The swarm and the queen: towards a deterministic and adaptive particle swarm optimization. In *Evolutionary Computation, 1999. CEC 99. Proceedings of the 1999 Congress on*, volume 3, 1999.
- [147] R. C. Eberhart and Y. Shi. Comparing inertia weights and constriction factors in particle swarm optimization. In *Evolutionary Computation, 2000. Proceedings of the 2000 Congress on*, volume 1, pages 84–88, 2000.
- [148] M. Clerc and J. Kennedy. The particle swarm: explosion, stability, and convergence in a multidimensional complex space. *Trans. Evol. Comp.*, 6(1):58–73, 2002.
- [149] P. J. Angeline. Using selection to improve particle swarm optimization. *Evolutionary Computation Proceedings.*, pages 84–89, 1998.
- [150] S. C. Esquivel and C. A. C. Coello. On the use of particle swarm optimization with multimodal functions. In *in Proceedings of the 2003 Congress on Evolutionary Computation. IEEE Press*, pages 1130–1136, 2003.
- [151] P. S. Andrews. An investigation into mutation operators for particle swarm optimization evolutionary computation. In *Evolutionary Computation, IEEE Congress on*, 2006.
- [152] T. Bäck. *Evolutionary Algorithms in Theory and Practice*. New York Oxford University Press, 1996.
- [153] D. Fogel. *Evolutionary Computation: Towards a New Philosophy of Machine Intelligence*. Piscataway, NJ: IEEE Press, 1996.
- [154] D. Fogel. *System Identification Through Simulated Evolution: A Machine Learning Approach to Modeling*. Needham Height MA: Ginn, 1991.

-
- [155] A. Sokolov and D. Whitley. Unbiased tournament selection. In *Proceedings of the Conference on Genetic and Evolutionary Computation*, pages 1131–1138. ACM Press, 2005.
- [156] D. E. Goldberg and K. Deb. A comparative analysis of selection schemes used in genetic algorithms. In *Foundations of Genetic Algorithms*, pages 69–93. Morgan Kaufmann, 1991.
- [157] K. B Lee and J. H. Kim. Particle swarm optimization driven by evolving elite group. In *Evolutionary Computation, 2009. CEC '09. IEEE Congress on*, pages 2114–2119, 2009.
- [158] M. Clerc. Think Locally, Act Locally: The Way of Life of Cheap-PSO, an Adaptive PSO. 2001.
- [159] A. M. Dale and M. I. Sereno. Improved localization of cortical activity by combining EEG and MEG with MRI cortical surface reconstruction: A linear approach. *J. Cogn. Neurosci*, 5(2):162–176, 1993.
- [160] S. Murakami and Y. Okada. Contributions of principal neocortical neurons to magnetoencephalography and electroencephalography signals. *The Journal of Physiology*, 575(3):925–936, 2006.
- [161] D. Goldberg. Genetic algorithms in search optimization and machine learning. *Addison-Wesley*, pages 1–25, 1989.
- [162] J. Fisher Box. Guinness, gosset, fisher, and small samples. *Statistical Science*, 2(1):45–52, 1987.
- [163] R. G. D. Steel and J. H. Torrie. *Principles and procedures of statistics a biometrical approach*. McGraw-Hill Book Comapany, New York, 2nd edition, 1980.
- [164] D. Harnett. *Statistical Methods*. Addison-Wesley, third edition, 1982.
- [165] W. Volk. *Applied Statistics for Engineers*. McGraw-Hill, 2nd edition, 1969.
- [166] R. O. Kuel. *Design of Experiments: Statistical Principles of Research Design and Analysis*. Duxbury Press, Pacific Grove, 2nd edition, 2000.
- [167] I. C. Trelea. The particle swarm optimization algorithm: convergence analysis and parameter selection. *Information Processing Letters*, 85(6):317–325, 2003.

- [168] M. Wagner, M. Fuchs, H. A. Wischmann, K. Ottenberg, and O. Dössel. Cortex segmentation from 3D MR images for MEG reconstructions. *In Biomagnetism: Fundamental Research and Clinical Applications*, pages 433–438, 1995.
- [169] T. Heinonen, H. Eskola, P. Dastidar, P. Laarne, and J. Malmivuo. Segmentation of T1 MR scans for reconstruction of resistive head models. *Computer Methods and Programs in Biomedicine*, 54(3):173–181, 1997.
- [170] H. Rifai, I. Bloch, S. Hutchinson, J. Wiart, and L. Garnero. Segmentation of the skull in MRI volumes using deformable model and taking the partial volume effect into account. *Med. Imag. Anal.*, 4:219–233, 2000.
- [171] G. Huiskamp, M. Vroeijenstijn, R. van Dijk, G. Wieneke, and A. C. van Huffelen. The need for correct realistic geometry in the inverse EEG problem. *IEEE Trans. Biomed. Eng.*, 46(11):1281–1287, 1999.
- [172] C. Studholme, D. L. G. Hill, and D. J. Hawkes. Automated 3D registration of MR and CT images of the head. *Med. Imag. Anal.*, 1(2):163–175, 1997.
- [173] S. M. Smith, M. Jenkinson, M. W. Woolrich, C. F. Beckmann, T. E.J. Behrens, H. Johansen-Berg, P. R. Bannister, M. De Luca, I. Drobnjak, D. E. Flitney, R. K. Niazy, J. Saunders, J. Vickers, Y. Zhang, N. De Stefano, J. M. Brady, and P. M. Matthews. Advances in functional and structural MR image analysis and implementation as FSL. *NeuroImage*, 23:208–219, 2004.
- [174] S. M. Smith. Fast robust automated brain extraction. *Human Brain Mapping*, 17(3):143–155, 2002.
- [175] FreeSurfer. [Online], <http://surfer.nmr.mgh.harvard.edu/>.
- [176] A. Mayer and H. Greenspan. An adaptive mean-shift framework for MRI brain segmentation. *Medical Imaging, IEEE Transactions on*, 28(8):1238–1250, 2009.
- [177] J. Ashburner and K. J. Friston. Voxel based morphometry: The Methods. *NeuroImage*, 11(6):805–821, 2000.
- [178] B. D. Ward. *Intracranial Segmentation*. Biophysics Research Institute, Medical College of Wisconsin, Milwaukee, WI, 1999.
- [179] H. Hahn and H. O. Peitgen. The skull stripping problem in mri solved by a single 3D watershed transform. *In Paper Presented at the Proceedings of MICCAI, LNCS*, volume 1935, pages 134–143, 2000.

-
- [180] A. H. Zhuang, D. J. Valentino, and A. W. Toga. Skull-stripping magnetic resonance brain images using a model-based level set. *NeuroImage*, 32(1):79–92, 2006.
- [181] L. Lemieux. Fast, accurate, and reproducible automatic segmentation of the brain in T1-weighted MR volumes. *Magnetic Resonance in Medicine*, 42(1):127–135, 1999.
- [182] S. M. Atkins and B. T. Mackiewich. Fully automatic segmentation of the brain in MRI. *IEEE Transactions on Medical Imaging*, 17(1):98–107, 1998.
- [183] Q. Mahmood, A. Chodorowski, A. Mehnert, J. Gellermann, and M. Persson. Automatic multi-tissue segmentation of MR images of the head using a hierarchical segmentation approach incorporating bayesian-based adaptive mean-shift. *Submitted to Journal of Computer Assisted Tomography*, 2012.
- [184] Y. Zhang, M. Brady, and S. Smith. Segmentation of brain MR images through a hidden markov random field model and the expectation-maximization algorithm. *Medical Imaging, IEEE Transactions on*, 20(1):45–57, 2001.
- [185] D. S. Tuch, V. J. Wedeen, A. M. Dale, and J. W. Belliveau. Electrical conductivity tensor map of the human brain using NMR diffusion imaging: An effective medium approach. *ISMRM, 6th Scientific Meeting, Sydney*, 1998.
- [186] M. Rullmann, A. Anwander, M. Dannhauer, S. K. Warfield, F. H. Duffy, and C. H. Wolters. EEG source analysis of epileptiform activity using a 1 mm anisotropic hexahedra finite element head model. *Neuroimage*, 44:399–410, 2009.
- [187] D. S. Tuch, V. J. Wedeen, A. M. Dale, J. S. George, and J. W. Belliveau. Conductivity tensor mapping of the human brain using diffusion tensor MRI. *Proc Natl Acad Sci USA*, 98(20):11697–11701, 2001.
- [188] D. Güllmar, J. Haueisen, and J.R. Reichenbach. Influence of anisotropic electrical conductivity in white matter tissue on the EEG/MEG forward and inverse solution. A high-resolution whole head simulation study. *Neuroimage*, 51(1):145–163, 2010.

- [189] S. Gabriel, R.W. Lau, and C. Gabriel. The dielectric properties of biological tissues: III parametric models for the dielectric spectrum of tissues. *Phys Med Biol*, 41(11):2271–2293, 1996.
- [190] A. Biegon, J. L. Eberling, B. C. Richardson, M. S. Roos, S. T. Wong, B. R. Reed, and W. J. Jagust. Human corpus callosum in aging and alzheimer’s disease: a magnetic resonance imaging study. *Neurobiol Aging*, 15(4):393–397, 1994.
- [191] V. Jurcak, D. Tsuzuki, and I. Dan. 10/20, 10/10, and 10/5 systems revisited: Their validity as relative head-surface-based positioning systems. *NeuroImage*, 34(4):1600–1611, 2007.
- [192] K. S. Saladin. *Anatomy and Physiology*. McGraw-Hill, New York, 2004.
- [193] A. D. Legatt. General principles of somatosensory evoked potentials. Online: <http://emedicine.medscape.com/article/1139906-overview#aw2aab6b3>, Last Update: Feb. 2012.
- [194] M. J. Aminoff. *Electrodiagnosis in clinical neurology*. Churchill Livingstone, 1986.
- [195] G. Cruccu, M. J. Aminoff, G. Curio, J. M. Guerit, R. Kakigi, F. Mauguiere, P. M. Rossini, R. D. Treede, and L. Garcia-Larrea. Recommendations for the clinical use of somatosensory-evoked potentials. *Clinical Neurophysiology*, 119(8):1705–1719, 2008.
- [196] A. Delorme and S. Makeig. EEGLAB: an open source toolbox for analysis of single-trial EEG dynamics. *Journal of Neuroscience Methods*, 134:9–21, 2004.
- [197] R. Broughton, T. Rasmussen, and C Branch. Scalp and direct recordings of somatosensory evoked potentials in man (circa 1967). *J. Psychol.*, 35(2):136–158, 1981.
- [198] H. Lueders, R. P. Lesser, J. Hahn, D. S. Dinner, and G. Klem. Cortical somatosensory evoked potentials in response to hand stimulation. *J. Neurosurg.*, 58(6):885–894, 1983.
- [199] M. P. Deiber, M. H. Giard, and F. Mauguiere. Separate generators with distinct orientations for N20 and P22 somatosensory evoked potentials to finger stimulation? *Electroenceph. clin. Neurophysiol.*, 65(5):321–334, 1986.

- [200] J. E. Desmedt, T. H. Nguyen, and M. Bourguet. Bit-mapped color imaging of human evoked potentials with reference to the N20, P22, P27 and N30 somatosensory responses. *Electroenceph. clin. Neurophysiol.*, 68(1):1–19, 1987.
- [201] T. Allison, G. McCarthy, C. C. Wood, P. D. Williamson, and D. D. Spencer. Human cortical evoked potentials by stimulation of the median nerve. I. cytoarchitectonic areas generating short-latency activity. *J. Neurophysiol.*, 62(3):694–710, 1989.
- [202] J. Spiegel, J. Tintera, J. Gawehn, P. Stoeter, and R. D. Treede. Functional MRI of human primary somatosensory and motor cortex during median nerve stimulation. *Clinical Neurophysiology*, 110(1):47–52, 1999.
- [203] W. H. Backes, W. H. Mess, V. van Kranen-Mastenbroek, and J. P. H. Reulen. Somatosensory cortex responses to median nerve stimulation: fMRI effects of current amplitude and selective attention. *Clinical Neurophysiology*, 111(10):1738–1744, 2000.
- [204] V. L. Towle, L. Khorasani, S. Uftring, C. Pelizzari, R. K. Erickson, J. P. Spire, K. Hoffmann, D. Chu, and M. Scherg. Noninvasive identification of human central sulcus: a comparison of gyral morphology, functional MRI, dipole localization, and direct cortical mapping. *NeuroImage*, 19(3):684–697, 2003.
- [205] T. Allison, G. McCarthy, C. C. Wood, and S. J. Jones. Potentials evoked in human and monkey cerebral cortex by stimulation of the median nerve. *Brain*, 114(6):2465–2503, 1991.
- [206] D. Brenner, J. Lipton, L. Kaufman, and S. J. Williamson. Somatically evoked magnetic fields of the human brain. *Science*, 199(4324):81–83, 1978.
- [207] Y. C. Okada, R. Tanenbaum, S. J. Williamson, and L. Kaufman. Somatotopic organization of the human somatosensory cortex revealed by neuro-magnetic measurements. *Exp. Brain Res.*, 56(2):197–205, 1984.
- [208] C. Baumgartner. *Clinical Neurophysiology of the Somatosensory Cortex*. Springer-Verlag, Wien, 1993.
- [209] D. L. J. Kelly, S. Goldring, and J. L. O’Leary. Averaged somatosensory evoked responses from exposed cortex in man. *Arch. Neurol.*, 13(1):1–19, 1965.

- [210] D. S. Dinner, H. Lüders, R. P. Lesser, and H. H. Morris. Cortical generators of somatosensory evoked potentials to median nerve stimulation. *Neurology*, 37(7):1141–1145, 1987.
- [211] N. N. Peterson, C.E. Schroeder, and J.C. Arezzo. Neural generators of early cortical somatosensory evoked potentials in the awake monkey. *Electroenceph. clin. Neurophysiol.*, 96(3):248–260, 1995.
- [212] <http://vincijesusbrain.blogspot.se/2007/12/brain-atlas-brodmann-areas-for-fmri.html>.
- [213] F. Babiloni, C. Babiloni, L. Locche, F. Cincotti, P.M. Rossini, and F. Carducci. High-resolution electro-encephalogram: source estimates of Laplacian-transformed somatosensory-evoked potentials using a realistic subject head model constructed from magnetic resonance images. *Medical and Biological Engineering and Computing*, 38(5):512–519, 2000.
- [214] R. Emerson and T. Pedley. Generator sources of median somatosensory evoked potentials. *J. Clin. Neurophysiol.*, 1(2):203–218, 1984.
- [215] I. Hashimoto. High-frequency oscillations of somatosensory evoked potentials and fields. *J. Clin. Neurophysiol.*, 17(3):309–320, 2000.
- [216] E. Recuero. The use of somatosensory evoked potentials for cortical localization during surgical operations. *Rev. Neurol.*, 28(6):588–590, 1999.
- [217] M. Sonoo. Anatomic origin and clinical application of the widespread N18 potential in median nerve somatosensory evoked potentials. *J. Clin. Neurophysiol.*, 17(3):258–268, 2000.
- [218] M. Valeriani, D. Le Pera, D. Niddam, L. Arendt-Nielsen, and A. Chen. Dipolar source modeling of somatosensory evoked potentials to painful and nonpainful median nerve stimulation. *Muscle Nerve*, 23(8):1194–1203, 2000.
- [219] R. Dowman and S. Schell. Innocuous-related sural nerve-evoked and finger-evoked potentials generated in the primary somatosensory and supplementary motor cortices. *Clin. Neurophysiol.*, 110(12):2104–2116, 1999.
- [220] K. Druschky, M. Kaltenhäuser, C. Hummel, A. Druschky, W. J. Huk, B. Neundörfer, and H. Stefan. Somatosensory evoked magnetic fields following passive movement compared with tactile stimulation of the index finger. *Experimental Brain Research*, 148(2):186–195, 2003.

- [221] D. Restuccia, M. Valeriani, A. Insola, M. Lo Monaco, E. Grassi, C. Barba, D. Le Pera, and F. Mauguiere. Modality-related scalp responses after electrical stimulation of cutaneous and muscular upper limb afferents in humans. *Muscle Nerve*, 26(1):44–54, 2002.
- [222] M. Schaefer, W. Muhl nickel, S. Grüsser, and H. Flor. Reproducibility and stability of neuroelectric source imaging in primary somatosensory cortex. *Brain Topogr.*, 14(3):179–189, 2002.
- [223] T. D. Waberski, H. Buchner, M. Perkuhn, R. Gobbele, M. Wagner, W. Kucker, and J. Silny. N30 and the effect of explorative finger movements: a model of contribution of the motor cortex to early somatosensory potentials. *Clin. Neurophysiol.*, 110(9):1589–1600, 1999.
- [224] W. Penfield and E. Boldrey. Somatic motor and sensory representation in the cerebral cortex of man as studied by electrical stimulation. *Brain*, 60(4):389–443, 1937.
- [225] R. Hari and N. Forss. Magnetoencephalography in the study of human somatosensory cortical processing. *Philos. Trans. R. Soc. London, B: Biol. Sci.*, 354(1387):1145–1154, 1999.
- [226] W. H. Backes, W. H. Mess, V. van Kranen-Mastenbroek, and Reulen J. P. H. Somatosensory cortex responses to median nerve stimulation: fMRI effects of current amplitude and selective attention. *Clinical Neurophysiology*, 111(10):1738–1744, 2000.
- [227] V. Ibanez, M. P. Deiber, N. Sadato, C. Toro, J. Grissom, R. P. Woods, J. C. Mazziotta, and Hallett M. Effects of stimulus rate on regional cerebral blood flow after median nerve stimulation. *Brain*, 118(5):1339–1351, 1995.
- [228] W. Penfield and T. Rasmussen. *The Cerebral Cortex in Man*. Macmillan, New York, 1957.
- [229] R. Kurth, K. Villringer, G. Curio, K. J. Wolf, T. Krause, J. Repenthin, J. Schwiemann, M. Deuchert, and A. Villringer. fMRI shows multiple somatotopic digit representations in human primary somatosensory cortex. *Neuroreport*, 11(17):1487–1491, 2000.
- [230] R. Ackerley, E. Hassan, A. Curran, J. Wessberg, H. Olausson, and F. McGlone. An fMRI study on cortical responses during active self-touch and passive touch from others. *Frontiers in Behavioral Neuroscience*, 6(51), 2012.

- [231] J. Talairach and P. Tournoux. *Co-planar Stereotaxic Atlas of the Human Brain*. Georg Thieme Verlag, Stuttgart, 1988.
- [232] J. L. Lancaster, M. G. Woldorff, L. M. Parsons, M. Liotti, C. S. Freitas, L. Rainey, P. V. Kochunov, D. Nickerson, S. A. Mikiten, and P. T. Fox. Automated talairach atlas labels for functional brain mapping. *Human Brain Mapping*, 10(3):120–131, 2000.
- [233] <http://www.slicer.org>.
- [234] K. R. Foster and H. P. Schwan. Dielectric properties of tissues and biological materials: a critical review. *Crit Rev Biomed Eng*, 17(1):25–104, 1989.
- [235] E. Behrens, J. Zentner, D. Roost, A. Hufnagel, C. E. Elger, and J. Schramm. Subdural and depth electrodes in the presurgical evaluation of epilepsy. *Acta Neurochirurgica*, 128(1-4):84–87, 1994.
- [236] C. W. van Veelen, R. M. Debets, A. C. van Huffelen, W. van Emde Boas, C. D. Binnie, W. Storm van Leeuwen, D. N. Velis, and A. van Dieren. Combined use of subdural and intracerebral electrodes in preoperative evaluation of epilepsy. *Neurosurgery*, 26(1):93–101, 1990.
- [237] J. Engel, T. R. Henry, M. W. Risinger, J. C. Mazziotta, W. W. Sutherling, M. F. Levesque, and M. E. Phelps. Presurgical evaluation for partial epilepsy: Relative contributions of chronic depth electrode recordings versus fdgpet and scalp-sphenoidal ictal eeg. *Neurology*, 40(11):1670, 1990.
- [238] L. Flemming, J. Haueisen, U. Tenner, F. Giessler, and M. Eiselt. Source localization accuracy in an animal model. *Biomedizinische Technik*, 46(2):138–140, 2000.
- [239] D. Güllmar, J. Haueisen, M. Eiselt, F. Giessler, L. Flemming, A. Anwander, T. R. Knosche, C. H. Wolters, M. Dumpelmann, D. S. Tuch, and J. R. Reichenbach. Influence of anisotropic conductivity on EEG source reconstruction: investigations in a rabbit model. *Biomedical Engineering, IEEE Transactions on*, 53(9):1841–1850, 2006.
- [240] Q. Shuo and S. Yang. A single camera photogrammetry system for multi-angle fast localization of EEG electrodes. *Annals of Biomedical Engineering*, 39(22):2844–2856, 2011.
- [241] M. Thordstein and R. Constantinescu. Possibly lifesaving, noninvasive, EEG-guided neuromodulation in anesthesia-refractory partial status epilepticus. *Epilepsy & Behavior*, 25(3):468–472, 2012.

-
- [242] R. Grebe, H. Zeaiter, V. Bach, F. Telliez, and R. Vandenhouten. Non-stationary time series analysis applied for evaluation of newborn sleeping stages under change of environment temperature. *Med. Biol. Eng. Comp.*, 37:438–439, 1999.

